Rheological Characterization of Polymers via Dissipative Particle Dynamics

MASSACHUSETTS INSTITUTE OF TECHNOLOGY
SEP 10 2008
LIBRARIES

by

Theis Forman Clarke

B.S., Purdue University (2002)
M.S.C.E.P., Massachusetts Institute of Technology (2004)

Submitted to the Department of Chemical Engineering
in partial fulfillment of the requirements for the degree of

Doctor of Philosophy

at the

MASSACHUSETTS INSTITUTE OF TECHNOLOGY

July 2008

© Massachusetts Institute of Technology 2008

The author hereby grants to Massachusetts Institute of Technology
permission to reproduce and
to distribute copies of this thesis document in whole or in part.

Signature of Author .....
Department of Chemical Engineering
July 29, 2008

Certified by.....
Robert C. Armstrong
Chevron Professor of Chemical Engineering
Thesis Supervisor

Accepted by.....
William M. Deen
Chairperson, Department Committee on Graduate Students

ARCHIVES

Rheological Characterization of Polymers via Dissipative Particle Dynamics

by

Theis Forman Clarke

Submitted to the Department of Chemical Engineering
on July 29, 2008, in partial fulfillment of the
requirements for the degree of
Doctor of Philosophy

Abstract

Dissipative particle dynamics (DPD) is a mesoscale simulation technique which uses soft potentials between large particles to reproduce liquid behavior. In form, DPD is similar to molecular dynamics, as all matter is represented by point particles which interact with each other via pairwise forces. The method was first introduced in the early 1990's, and has since undergone a number of refinements which have put it on a firm thermodynamic footing. DPD is notable for the flexibility it presents the modeler for building complex fluid systems. DPD has been used to study simple molecular liquids, polymer and colloid solutions, and phase behavior of block copolymer melts. Recently, a number of workers have used DPD to study the flow of polymer solutions in various geometries such as microchannels, pores, and sudden contractions. While these types of flows are well-suited to DPD's relative strengths, an important step has been skipped. Before the results of these complex flows can be accepted, it is necessary to demonstrate that the rheological predictions made by DPD are generally reliable. The principle aim of this thesis is to demonstrate that the rheology of polymer solutions can be simulated successfully with DPD.

The rheology of a solution of DPD dumbbells using a FENE spring force law is studied in the first part of this thesis via simulation of steady shear flow and steady planar elongational flow. The rheological results are compared to dilute Brownian dynamics simulations of the same FENE dumbbell model. The level of coarse-graining of the DPD fluid is varied by changing the length of the DPD dumbbell relative to the particle size, while maintaining a constant extensibility parameter. Broadly speaking, the viscosity, first normal stress coefficient, and dumbbell extension in shear flow calculated with DPD are in agreement with the BD results. The two methods are not perfectly alike however, and two systematic differences between the DPD and BD results are observed. An excluded volume effect which occurs naturally in DPD and is not present in the BD simulations results in elevated viscosity and dumbbell extension in the zero-shear-rate

regime. The effect is more powerful in DPD dumbbells which are more coarse-grained. At high shear rates in the power-law regime, DPD systematically overpredicts the rate of shear-thinning, with the greatest deviation occurring in the most coarse-grained dumbbells. This is hypothesized to be a result of hydrodynamic interaction which comes naturally out of DPD's explicit treatment of the solvent. The HI effect is analyzed using the Giesekus anisotropic drag tensor.

Shortly after its introduction, the complaint was made that DPD's dynamic results are suspect because it has a very low, gas-like Schmidt number, meaning that momentum and mass are transported through the DPD medium at similar rates. This is in contrast with physical liquids, which have large Schmidt numbers. The use of the Lowe-Anderson formulation of DPD allows the Schmidt number of a solution to be varied for the same polymer model. Shear flow simulations of identical dumbbells under different Schmidt number conditions give results in excellent agreement with each other, indicating that the Schmidt number is not an important factor in determining polymer rheology with DPD.

Steady planar elongational flow is simulated for the first time in DPD using the Kraynik and Reinelt boundary conditions, which are periodic in both space and time, allowing for simulations of planar elongational flow for an unlimited period of time. The planar elongational flow results of FENE dumbbells are also in agreement with BD, butshow the same systematic deviations observed in shear flow.

The second portion of this thesis examines a more complex polymer solution using DPD, with simulations of semidilute solutions of longer $N = 20$ bead-spring chain polymers undergoing shear and planar elongational flow. In addition to concentration effects, the importance of the solvent quality is also examined with simulations of polymer solutions in both good and theta solvents. In order to capture concentration dependency, a spring-spring repulsion force is added to the DPD model to prevent polymer springs from passing though each other. A strong concentration dependence on the longest relaxation time is observed. In planar elongational flow, each solution goes through a coil-stretch transition at the theoretically predicted strain rate $\mathrm{De} = 0.5$. In shear flow, the rheological results are in qualitative agreement with theory, showing a plateau at low De, and a transition into a shear-thinning regime beginning at $\mathrm{De} = 1$. While the planar elongational flow results show clear dependence on the solution relaxation time, the shear results show a mixed dependence on the overall solution relaxation time, which reflects the concentration dependence, and the relaxation rate of an isolated chain, suggesting that only some aspects of the shear rheology are affected by the concentration.

The conclusion of this thesis is that DPD is able to faithfully reproduce reliable rheological behavior with bead-spring polymer models. We find however, that the computational costs associated with the explicit simulation of the solvent put DPD at a disadvantage for systematic rheology studies when compared to Brownian dynamics. The high costs of the spring-spring repulsion force implementation are particularly limiting. In complex systems where DPD's natural flexibility in molecular architecture and chemistry make it the best choice, rheological results can now be accepted with more

confidence.

Thesis Supervisor: Robert C. Armstrong
Title: Chevron Professor of Chemical Engineering

Acknowledgements

I owe a debt of gratitude to Professor Robert C. Armstrong for his patience and steady hand. Thank you Bob, for all the good advice and encouragement you've given me throughout the last six years. There are some fragile moments for every graduate student, and you helped me to get through mine with my sanity intact.

Thanks go as well to the National Science Foundation for funding my first three years through a graduate research fellowship, and to the Center for Advanced Engineering of Fibers and Films at Clemson University for funding the balance of my time here.

Special thanks are due to Melanie, Katie, Alina, Patty, Gwen, and Suzanne for all your help in scheduling, travel support, giving me candy, and generally bailing me out of paperwork trouble. You keep this department afloat.

To the Armstrong group, who've been one of my surrogate families these last few years, Micah, Zubair, David, Kate, Scott, Irina, Arvind, Markus, and Pankaj, thank you for all the camaraderie, sneaky trips to the driving range, illuminating research discussions, and emotional support.

My fellow grad students in the department have made all the difference these past years. I love you all. Jake, thank you for putting up with me for four years as a roommate. Kristin, thank you for dragging me to furniture making class.

I would not have ever made it this far without the love and support of my parents, Stephen and Nancy, and my four siblings Kyliah, Byron, Myles and Wyatt. Thank you for all the encouragement.

Most of all, thank you Catherine. We're the right sort of crazy for each other. You have been wonderful to me these last couple of years. You're a walking reminder to me that there is an intellectual world out there larger than chemical engineering.

I couldn't have done it without you.

Contents

List of Figures

Chapter 1

Introduction

1.1 Motivation

One of the defining challenges associated with the computational study of polymeric systems is that of length scale. Within a long chain polymer, a multiplicity of length and time scales are represented, from the atomistic length scale associated with atomic vibrations, to the Kuhn length, defined as the length over which the polymer backbone is stiff, to the full contour length of the macromolecule, which can reach to hundreds of microns. Polymer physicists have developed a number of different methods for studying polymer systems, which can be organized based on the length scale they address, and consequently the level of molecular detail they are able to resolve. The most coarse-grained methods are continuum based, in which the physics of the polymer solution is modeled as a field quantity. At this level, closed constitutive equations are required to calculate the fluid stresses and other system-level quantities of interest, which limits the molecular complexity that can be captured. As we zoom in closer, we arrive at kinetic theory, in which a mechanical model of the macromolecule is made to interact with a surrounding fluid. The stresses and other fluid properties are calculated as a function of the configuration of the individual molecular model molecules and the flow field of

the surrounding solvent. The models used in kinetic theory to represent polymers run the gamut from the very simple Hookean spring dumbbell, in which an entire polymer chain is represented by a spring connecting two beads, to the Kramers chain, a bead-rod representation which captures Kuhn length-level details, to even smaller-scale models. Finally, we arrive at the very small length scale domain of molecular dynamics and Monte Carlo methods, which seek to model polymer systems at the monomer, or even atomic scale. In these methods, both solvent and polymer are represented as particles rather than as a continuum fluid. As the methods become more fine-scale, molecular detail is traded for computational cost. The time and length scales which can be addressed by molecular dynamics are orders of magnitude smaller than those which can be addressed by kinetic theory, which in turn are much smaller than those amenable to study with continuum methods. It is thus natural to seek methods of polymer simulation with intermediate cost, and an intermediate level of detail in order to address problems for which traditional kinetic theory models are too coarse, but for which molecular dynamics and Monte Carlo are too costly. It is here that dissipative particle dynamics (DPD) finds its home.

1.1.1 History of DPD

DPD was first proposed in the early 1990's by Hoogerbrugge and Koelman[40] as a method useful for studying mesoscopic complex fluid systems using a framework taken from molecular dynamics (MD). Mesoscopic refers to length scales which are large in comparison to atomic or molecular lengths, but small relative to everyday experience. In form, DPD closely resembles MD, as it is a fluid made of entirely of particles which interact with other nearby particles through pairwise forces. As such, the implementation of the two methods have much in common. DPD departs from MD, however, when the nature of the particles themselves are considered. Each DPD particle represents a large number of solvent or monomer units, and might be better thought of as a fluid packet or element. DPD is distinguished from other mesoscale simulation techniques such as

lattice-gas cellular automata [69] and lattice-Boltzman equation [7] in that the particles move continuously in space, rather than along a predefined lattice. The pair-interaction laws lead to DPD to conserve momentum, which in turn leads to hydrodynamic behavior. DPD was quickly adopted by a number of other workers who recognized that the form of the model would allow for a great deal of flexibility in building complex molecules and systems. Using DPD to model polymers by connecting DPD particles with entropic springs was proposed very early[70], and was followed up with studies of the effects of solvent quality on relaxation and conformation of polymer molecules.[44].Espanol and Warren[20] made a major contribution to the development of DPD when they proposed a constraint on the coefficients and weighting functions of the dissipative and random forces, satisfying the fluctuation-dissipation theorem. With their modification, these two forces function as a thermostat, maintaining a constant systemwide temperature. Groot and Warren[37] made the next major contribution, establishing an integration algorithm for Newton's equations of motion, and making the first theory-based argument for the value of the conservative force coefficient. This paper also introduced a relationship between DPD parameters and Flory-Huggins χ-parameters, which led to a great deal of additional work using DPD to study polymer phase behavior[15, 14, 58]. Marsh *et al.*[55] made an effort to derive thermodynamic and transport properties of the simple DPD fluid via the solution of the Fokker-Planck-Boltzmann equation, leading to estimates of the viscosity and self-diffusion constants.

The use of DPD as a method of studying polymer systems continued to develop with additional work on the properties of polymers at equilibrium. Spenley[75] showed that DPD bead-spring chains followed Rouse scaling in the relaxation time, diffusivity, and radius of gyration. Pan and Manke[62] investigated the use of a linear spring-spring repulsion in order to simulate polymer melts. Willemsen *et al.*[82] explored the use of frozen DPD particles to build a wall which would exhibit no-slip boundary conditions, later using the method to simulate pressure-driven flow in a chromatography channel[83] in one of the first instances of DPD being used to simulate a flowing polymer solution.

Further work on DPD simulations with walls is also available[27, 54, 67, 66, 65, 85, 86, 87]. Fan *et al.*[26] used DPD to simulate flows of DNA solutions in channels. The work was further refined[17, 25] to include more realistic treatment of the wall boundaries and spring force law. DPD has been widely used to simulate phase behavior of block copolymers[12, 29, 30, 36, 48], aphiphilic polymers[42, 71, 72], lipid bylayers[32, 45, 84], polymer brushes[60, 41], and particle adsorption[34]. The DPD method has also been used to model a number of other physical systems and flow types which are not addressed in this thesis, including dense phase colloid systems[9, 10], flow around spheres[13, 43], capillary wetting[16], and flow in pores[49, 51].

In 2003, Lowe[52] made an important contribution to DPD with the introduction of an alternate thermostat, which replaces the dissipative and random forces with a modification of the Anderson thermostat from MD. The new method allows for greater control of the Schmidt number, greatly increasing the flexibility of the method for performing non-equilibrium simulations. This development led to several studies of the effect of the Schmidt number on solutions of DNA and other flexible polymer systems[79, 78].

In all the papers mentioned above, the extraordinary flexibility of the DPD system is used in a number of ways to attack problems which are difficult to access with other methods. The results, however, are presented based upon an assumption that the DPD method reproduces correct rheological behavior in polymer solutions generally. This assumption has never been tested in a systematic way. Quantities are reported which reflect on the rheology of the polymer system, such as velocity profiles in channel flow, and spring extension in shear flow, but in no cases are material functions reported explicitly, especially with respect to the strain rate. This deficiency in the DPD literature forms the basis for the motivation of this thesis. I am seeking to place non-equilibrium simulation of polymer solutions in DPD on a firmer footing by performing simulation experiments which can be replicated with other methods. Showing that DPD produces verifiably correct results for simple problems will make DPD's predictions of more complicated phenomena like those studied by previous DPD workers more believable. To this end, I

have developed DPD codes for simulating shear and planar elongational flow over a wide range of strain rates. I show that DPD produces realistic rheological results both at low strain rates in which the polymer molecules are not significantly deformed, as well as at high strain rates, in which the molecules change their shape drastically, resulting in very nonlinear rheological responses.

This analysis is carried out twice; once for dilute FENE dumbbells, which is a very simple model, and easy to compare to other methods, and once for concentration-dependent long chains in varying solvent quality, as a demonstration of DPD's performance studying the rheology of complex systems for which it is well-positioned.

1.2 Thesis Outline

This thesis is organized progressively, beginning with an introduction to the method in its various forms. Chapter 2 contains an in-depth description of the original DPD method, including a breakdown of the governing equations and pairwise forces which act between particle pairs. The significance of each of the coefficients is explored, as well as the role of the weighting functions in each of the pairwise forces. Special attention is paid to the conservative force coefficient, which controls the chemistry of the DPD fluid. The constraints on the dissipative and random forces which work together to form a thermostat in the MD sense are explained next. I then discuss the limitations on the use of DPD for non-equilibrium simulations, including the strains rates which are practically accessible, and the potential difficulty due to low Schmidt number. The alternative DPD thermostat proposed by Lowe[52] is then introduced. Finally, the concept of using DPD to model macromolecules with bead-spring chains is presented, along with a system for assigning physical scales to DPD length, time, and mass units.

Chapter 3 deals with the details required to implement non-equilibrium flow simulations of DPD systems. Two well-known flow types, simple steady shear flow, and steady planar elongational flow are studied in this thesis. For both flows, periodic boundary

conditions which are specific to the flow in question are used. For shear flow, Lees-Edwards boundary conditions involve periodic images which move relative to the simulation domain. Implementation using LE boundary conditions requires careful treatment of interactions that occur across the moving periodic boundary, including pairwise particle interactions, polymer spring force calculations, and the calculation of configurational quantities. Implementation of planar elongational flow is somewhat more involved, as it entails the use of Kraynik and Reinelt's boundary conditions. The KR boundary conditions describe a periodic domain that deforms with the flow until a certain total strain is reached, at which point a temporal periodicity is reached, allowing the shape of the domain to be reset to it's original configuration without interrupting the particle-level details of the fluid. KR boundary conditions have never been used with DPD before. In addition to a detailed explanation of how the KR boundary condition system works, the treatment of interactions which occur across the moving/deforming boundaries are presented in a step-by-step manner intended to function as a how-to manual for future investigators.

Chapter 4 contains the first set of simulation results presented in this thesis. The shear and planar elongational behavior of dilute solutions of FENE dumbbells are investigated via nonequilibrium DPD simulation, and the results are compared quantitatively with those of Brownian dynamics simulations of the same molecular models. The purpose of this chapter is to demonstrate that DPD is useful for studying the rheology of polymer systems, and that the results produced by the DPD method match those of another better-established method. The FENE dumbbell molecular model is purposefully chosen to be as simple as possible, in order to produce results which can be analyzed in as simple and uncluttered a manner as possible. Viscosity, first normal stress coefficient, and dumbbell configuration are studied in detail. The length scale of the DPD particle pair interaction (in short, the particle diameter) relative to the dumbbell length is varied, allowing us to study the relative importance of the effects of excluded volume and hydrodynamic interaction on the rheology of polymers in DPD.

Chapter 5 brings together a number of the attractive capabilities of DPD in a single set of simulations. A longer $N = 20$ bead-spring chain polymer molecule is simulated in steady shear and steady planar elongational flow throughout the semi-dilute regime. The solvent quality is varied as well. In order to include concentration effects, a spring-spring repulsion force is added to the DPD model to prevent polymer chain backbones from passing through each other. The implementation details and performance of this addition to the DPD method are presented in this chapter. The concentration-dependent rheology of the polymer solutions are presented for each flow, and the results are compared to a similar study of λ-DNA using Brownian dynamics.

Finally, in Chapter 6, the thesis is concluded with an examination of the utility of DPD as a simulation method for polymer rheology. While I have shown for the first time that DPD is able to reproduce believable rheological results for two important types of flow, the question remains as to whether the considerable computational costs and inherent modeling limitations that accompany the DPD method make it worthwhile to use for studying this type of phenomena.

Chapter 2

Dissipative Particle Dynamics

Dissipative Particle Dynamics (DPD) is a mesoscopic simulation technique which is modeled loosely on Molecular Dynamics. The term mesoscopic indicates that DPD occupies the space between Molecular Dynamics and Monte Carlo methods, which seek to model systems at the level of individual atoms or groups of atoms, and continuum descriptions, which make the assumption that the contributions of individual particles can be represented as field quantities. Roughly speaking, mesoscale is thought to refer to characteristic lengths of $10nm$ to $1\mu m$. A DPD fluid is made up of particles which have continuous spatial positions and velocities, but which are updated discretely in time. In this way, it is differentiated from other mesoscopic methods such as Lattice-Boltzman[7] and lattice Monte Carlo methods, wherein particles are restricted to a set of discrete positions. The motion of the particles is governed by pairwise forces. In this way, DPD is superficially similar to MD. DPD particles, however, are not intended to represent individual atoms. Rather, each particle should be viewed as a fluid packet, or element which may contain thousands or even millions of atoms. DPD particles do not have hard-sphere repulsions with each other, and as a result overlap with each other to a significant degree. DPD was first suggested in the early 1990s by Hoogerbrugge and Koelman[40] as an attempt to address the mesoscopic scale without having to resort to lattice methods.

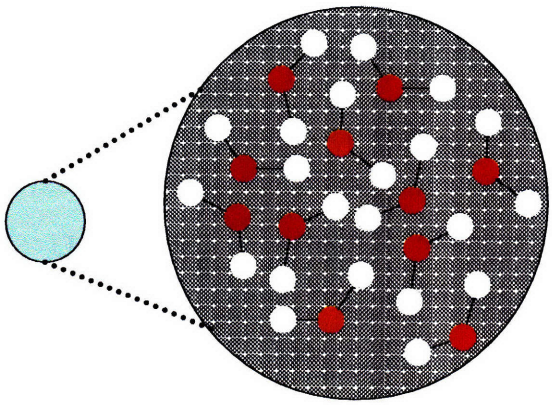

Figure 2-1: A DPD particle should be thought of as a fluid element, or collection of atoms, rather than a physical particle. DPD particles are point particles, so the only measure of size is the interaction length, r_c.

2.1 The Method

DPD consists of an ensemble of point particles $i = 1, ..., N$ whose positions and momenta at time t are denoted by $\mathbf{r}_i(t)$ and $\mathbf{p}_i(t)$ respectively. The time evolution of $\mathbf{r}_i(t)$ and $\mathbf{p}_i(t)$ are updated according to Newton's equations of motion

$$\frac{d\mathbf{r}_i}{dt} = \mathbf{v}_i \tag{2.1}$$

and

$$\frac{d\mathbf{p}_i}{dt} = \mathbf{F}_i \tag{2.2}$$

where $\mathbf{v}_i = \mathbf{p}_i/m_i$. For simplicity, the masses of all DPD particles are chosen to be equal. The DPD unit of mass is chosen such that $m = 1$, so we will dispense with the use of the momentum $\mathbf{p}_i$, and deal exclusively with $\mathbf{v}_i$ from now on. The total force on particle i is the sum of a conservative force, a dissipative force, and a random force, each of which is pairwise additive

$$\mathbf{F}_i = \sum_{i \neq j} \left[\mathbf{F}_{ij}^C (\mathbf{r}_{ij}) + \mathbf{F}_{ij}^D (\mathbf{r}_{ij}, \mathbf{v}_{ij}) + \mathbf{F}_{ij}^R (\mathbf{r}_{ij}) \right] \tag{2.3}$$

where the sum runs over all particles found within a cutoff radius designated by r_c. As DPD contains no other inherent length scales, we will choose a unit length to be $r_c = 1$. Here $\mathbf{r}_{ij}$ refers to the interparticle vector $\mathbf{r}_{ij} \equiv \mathbf{r}_j - \mathbf{r}_i$, and $\mathbf{v}_{ij}$ is the difference in the velocity of particles i and j, $\mathbf{v}_{ij} \equiv \mathbf{v}_j - \mathbf{v}_i$. Below are descriptions of each of the component forces:

The Conservative Force

The conservative force is a soft repulsion that acts on a line between the two particles and is defined as

$$\mathbf{F}_{ij}^C (\mathbf{r}_{ij}) = \begin{cases} a_{ij}(1 - r_{ij})\hat{\mathbf{r}}_{ij} & (r_{ij} < 1) \\ 0 & (r_{ij} \geq 1) \end{cases} \tag{2.4}$$

where a_{ij} is the maximum repulsion between particles i and j, r_{ij} is the length of $\mathbf{r}_{ij}$; $r_{ij} = |\mathbf{r}_{ij}|$, and $\hat{\mathbf{r}}_{ij}$ is the unit vector in the direction of $\mathbf{r}_{ij}$; $\hat{\mathbf{r}}_{ij} = \mathbf{r}_{ij}/r_{ij}$. The conservative force is similar to that used in molecular dynamics. The choice of the linear weighting function represents an averaging over the rapid fluctuations of many atoms obeying a Lennard-Jones potential. The key feature of the conservative force is that at very small separation distances, the repulsion force is finite. This is referred to as a soft potential.

The Dissipative Force

The dissipative force is dependent on both the separation distance and the relative velocity of the two particles

$$\mathbf{F}_{ij}^D (\mathbf{r}_{ij}, \mathbf{v}_{ij}) = -\gamma w^D(r_{ij})(\hat{\mathbf{r}}_{ij} \cdot \mathbf{v}_{ij})\hat{\mathbf{r}}_{ij} \tag{2.5}$$

where $w^D(r_{ij})$ is an arbitrary weighting function that is finite at $r_{ij} < 1$ and vanishes for $r_{ij} \geq 1$. γ is a coefficient controlling the amplitude of the dissipative force. This parameter is important in determining the viscosity of the simple DPD fluid. From a

physical standpoint, it is useful to view the dissipative force as a friction interaction between particles that pass close to each other having different velocities. A particle moving more slowly receives momentum from a faster particle, while the faster particle is slowed down. This momentum exchange contributes strongly to the viscosity of the fluid as a whole.

The Random Force

The final term in Eq. 2.3 is the random force acting on particle pairs:

$$\mathbf{F}_{ij}^{R}\left(\mathbf{r}_{ij}\right) = \sigma w^{R}(r_{ij})\theta_{ij}\widehat{\mathbf{r}}_{ij} \tag{2.6}$$

where $w^R(r_{ij})$ is the weighting function for the random force, and σ is the coefficient governing the strength of the interaction. θ_{ij} is a random Gaussian variable with mean 0 and unit variance. The random force models the averaged result of a multiplicity of atomic collisions that occur in a physical fluid. In this, it can be thought of as analogous to the Brownian force in Brownian Dynamics simulations. It should be noted that Groot and Warren report that a uniform distribution for θ_{ij} gives indistinguishable results. As uniformly distributed random numbers can be produced for $\frac{1}{6}$ the computational cost of Gaussian random numbers, this is a development worth implementing.

2.1.1 Fluctuation-Dissipation Theorem

When DPD was introduced by Hoogerbrugge and Koelman[40], they suggested that the weighting functions for the dissipative and random forces be set equal to each other, however Espanol and Warren [37] later showed that in order to satisfy the fluctuation-dissipation theorem, neither the weighting functions, nor the coefficients of the dissipative and random forces were independent of each other. Rather, the following relationships must be satisfied:

$$w^{D}(r_{ij}) = \left[w^{R}(r_{ij})\right]^{2} \tag{2.7}$$

and

$$\sigma^2 = 2k_B T\gamma. \tag{2.8}$$

While the choice of $w^D(r_{ij})$ is arbitrary, the majority of DPD workers have opted for the simple choice of

$$w^D(r_{ij}) = \left[w^R(r_{ij})\right]^2 = \begin{cases} [(1-r_{ij})\widehat{\mathbf{r}}_{ij}]^2 & (r_{ij} < 1) \\ 0 & (r_{ij} \geq 1) \end{cases} \tag{2.9}$$

so that $w^R(r_{ij})$ is identical to the linear weighting function used in the conservative force. The fluctuation-dissipation theorem ensures that the total energy added to the system due to the random force is equal to the total energy removed from the system due to the dissipative force. As such, the random and dissipative forces in DPD, constrained by Eqs. 2.7 and 2.8 form a thermostat, which ensures that the system temperature remains constant at the setpoint of $k_B T$. It should be pointed out that DPD is incapable of sustaining a non-homogeneous temperature field due to the presence of a thermostat.

2.1.2 Integration Scheme

The Newtonian equations of motion for DPD which we have described in detail in the preceding section are typically integrated using a modified velocity-Verlet algorithm, given here:

$$\begin{aligned} \mathbf{r}_i(t+\Delta t) &= \mathbf{r}_i(t) + \Delta t \mathbf{v}_i(t) + \tfrac{1}{2}(\Delta t)^2 \mathbf{f}_i(t), \\ \tilde{\mathbf{v}}_i(t+\Delta t) &= \mathbf{v}_i(t) + \lambda \Delta t \mathbf{f}_i(t), \\ \mathbf{f}_i(t+\Delta t) &= \mathbf{f}_i(\mathbf{r}_i(t+\Delta t), \tilde{\mathbf{v}}_i(t+\Delta t)), \\ \mathbf{v}_i(t+\Delta t) &= v_i(t) + \tfrac{1}{2}\Delta t(\mathbf{f}_i(t) + \mathbf{f}_i(t+\Delta t)) \end{aligned} \tag{2.10}$$

with $\lambda = \frac{1}{2}$ being typical. $\tilde{\mathbf{v}}_i$ is an intermediate velocity used in the calculation of the interparticle forces. Further work on integration schemes and timestep dependence

in DPD is available in[33, 38, 57, 59, 64, 73, 77, 80].

2.2 Parameter Choice in DPD

In addition to specifying the form of the equations, one must choose values for the parameters that appear in the governing equations. The most common choices of parameter values are presented in this section, along with the rationale for so choosing. Generally, the choice of DPD parameters is made based on a combination of physical rationalization and practical computational necessity.

2.2.1 Physical Units in DPD

The time scale in the DPD system is a result of choosing the temperature, $k_BT = 1$ along with the MD definition of the temperature, $k_BT = \langle v^2 \rangle / d$ where $\langle ... \rangle$ is the average over all particles in the simulation, and d is the number of spatial dimensions. Thus time is scaled such that a particle with velocity $v = 1$ will move a distance r_c in one time unit. In choosing a timestep Δt, the modeler must compromise between a desire to save computational resources by using as large a timestep as possible, and yet not compromising the stability of the simulation. The accuracy of the integration of the equations of motion is measured by monitoring the deviation from the set point temperature. Groot and Warren[37] found that, using the velocity-Verlet algorithm given above, $\Delta t = 0.04$ resulted in deviations from the setpoint temperature of less than 1% for a simulation using a random force noise amplitude of $\sigma = 3$. The same accuracy from a simpler Euler method algorithm required $\Delta t \approx 0.001$. Increasing the noise amplitude σ reduces the accuracy of the integration.

2.2.2 The Conservative Repulsion Parameter

Once Δt and σ have been chosen, only a_{ij}, the particle pair repulsion coefficient, is required to fully specify the method. The first two parameters relate to the simulation

itself, while a_{ij} describes the model fluid. In order for fluctuations in the DPD liquid to faithfully reproduce those of the physical model, the compressibility of the liquid must be correct. The compressibility is given by

$$\kappa^{-1} = \frac{1}{nk_BT\kappa_T} = \frac{1}{k_BT}\left(\frac{\partial p}{\partial n}\right)_T \tag{2.11}$$

where n is the particle number density, and κ_T is the isothermal compressibility. For reference, water at $300K$ has $\kappa^{-1} = 15.9835$. From the virial theorem, Groot and Warren[37] define the pressure as

$$p = \rho k_BT + \frac{1}{3V}\left\langle \sum_{j>i}\left(\mathbf{r}_{ij}\cdot\mathbf{F}_{ij}^C\right)\right\rangle \tag{2.12}$$

from which they were able to show that for densities $\rho > 2$, an approximation of the pressure is given by

$$p = \rho k_BT + \alpha a\rho^2 \tag{2.13}$$

where the coefficient for the quadratic term is $\alpha = 0.101 \pm 0.001$. Thus the dimensionless compressibility can be approximately expressed as

$$\kappa^{-1} = 1 + 0.2a\frac{\rho}{k_BT}\ . \tag{2.14}$$

Normally, DPD modelers choose the compressibility of their fluid to be similar to water, which leads to a guideline for choosing the repulsion coefficient to be

$$a_{ij} = \frac{75k_BT}{\rho}. \tag{2.15}$$

Most DPD studies in the literature have chosen ρ to be between 3 and 4, as the object is to reproduce hydrodynamic behavior for the cheapest computational cost. The CPU cost per timestep per unit volume increases as the square of the density, so modelers have good reason to use a density only as great as is necessary.

Chemical Species Differentiation

Chemical species are easily differentiated in DPD systems simply by specifying that the interspecies repulsion coefficient between unlike atoms, a_{AB} be different than the intraspecies coefficients a_{AA} and a_{BB}. Groot and Warren showed that the repulsion coefficients could be accurately mapped onto Flory-Huggins parameters, and that with sufficiently dissimilar repulsion coefficients, phase separation could be achieved, and a surface tension measured which agrees with theory. This ability to represent unlike species without any major modification to the model is one of the key strengths of DPD.

2.2.3 Dynamics

The governing parameters for DPD have all been established using arguments taken from DPD's equilibrium behavior. As rheologists, we are at least as concerned with the dynamics of the DPD fluid model. One important quantity which has been much discussed in the DPD literature is the Schmidt number $Sc = \nu/D$, where ν is the kinematic viscosity and D is the particle autodiffusion constant. This dimensionless number can be interpreted as the ratio between the rates of diffusion of momentum and mass, or instead as a comparison of the time it takes a particle to travel a certain distance against the time required for hydrodynamic interactions to travel the same distance. For reference, the Schmidt number of liquid water is of order 10^3. Marsh *et al.*[55] have proposed relations for the transport properties of the DPD fluid. The self diffusion coefficient is given by

$$D \approx \frac{45 k_B T}{2\pi\gamma\rho r_c^2} \tag{2.16}$$

and the kinematic viscosity by

$$\nu \approx \frac{D}{2} + \frac{2\pi\gamma\rho r_c^5}{1575} \tag{2.17}$$

where the first term is the kinetic contribution, and the second comes from the dissipative force contribution. The conservative force contributions are neglected. This

results in a prediction for the Schmidt number of

$$Sc \approx \frac{1}{2} + \frac{\left(2\pi\gamma\rho r_c^4\right)^2}{70875 k_B T}. \tag{2.18}$$

Measurements of the transport properties of DPD can alternately be calculated from direct simulation, either via Green-Kubo relations, or by direct measurement of the results of non-equilibrium flow experiments[6]. For typical operating conditions, the Schmidt number for the DPD fluid is of order 1.

Limitation on DPD Fluid Viscosity

From the perspective of one interested in polymer rheology, the formulation of DPD presented above has some key limitations. The first is with regard to the viscosity of the simple DPD fluid. In dilute polymer solutions, the viscosity of the Newtonian solvent has a significant effect on the relaxation time scale of the polymer molecule being studied. In the experimental world, the introduction of Boger fluids allowed researchers to study dilute solutions of polymers whose dynamics were too fast to access experimentally when they were in solution with solvents of lower viscosity. One wishing to simulate polymer solutions with DPD finds the same limitation here. The viscosity of the simple DPD fluid affects the relaxation time of polymers in solution with it, which in turn affects the strain rates at which interesting polymer dynamics occur. The viscosity of the DPD fluid, expressed in Eq. 2.17 depends on the density, the interaction radius, and γ, the strength of the dissipative force. Due to the dependence of γ on σ found in Eq. 2.8, γ cannot be increased without a commensurate decrease in the timestep size. Similarly, increasing either ρ or r_c results in very large increases in the computational cost of the model as many more particles pair distances and forces must be calculated at each time step. As such, the simple fluid viscosity that is available to a modeler is relatively static.

Limitation on Strain Rate

As with all stochastic methods, DPD results always include a noise term, which must be reduced to a small fraction of the quantity being measured. This can be accomplished either by simulating a large number of DPD particles, or else by running the simulation over a long time period, and averaging the results. The cost of increasing either time or system size scales approximately linearly. As a result of this, the accurate measurement of dynamic quantities such as polymer stress becomes more and more computationally demanding as the rate of strain is decreased. This principle puts a lower bound on the rates of strain which are practically accessible via DPD simulation. The upper bound is set by the fluid itself. As the strain rate is increased, individual beads have less time to sample each other's presence in the fluid as they pass. As the strain rate, defined in native DPD units approaches unity, the viscosity of the simple DPD fluid begins to decrease. We are wishing to treat the simple DPD fluid as a Newtonian solvent, so we must limit ourselves to strain rates in which the fluid behaves as such, having a constant viscosity. This results in an upper limit on the DPD shear rate of 0.3.

2.3 The Lowe-Anderson Thermostat

Given the limitations on the Schmidt number, there have been a number of efforts to modify the DPD model to address this problem. Fan *et al.* [25] have proposed the introduction of a new interaction range which is used exclusively for the dissipative force. This range would be larger than the conservative force range, and would result in more particle-pairs exchanging momentum. By varying the dissipative interaction range, they are able to gain a lever with which to manipulate the Schmidt number. The chief disadvantage of this approach is in the computational cost involved. As the secondary interaction distance is increased, the efficiency of the simulation suffers.

In another approach to addressing the issue of low Schmidt number, Lowe [52] has presented an interpretation of DPD in which the method is split between the conserv-

ative force, which serves to govern the thermodynamic behavior of the system, and the dissipative and random forces, which serve as the thermostat keeping the system at a consistent total kinetic energy, due to their connection through the fluctuation-dissipation law. He argues that there is no reason that the soft conservative potential must be used in conjunction with the DPD thermostat in order to convey the advantages native to it, namely that large time and length scales can be addressed in simulation relative to molecular dynamics. Several of the advantages associated with DPD are due to specific properties of the DPD thermostat, but are not necessarily unique to it. In particular, the DPD model conserves momentum because all particle interactions are pairwise, so that when momentum is exchanged between particles the pair's momentum is unchanged and thus there is no global change in the momentum of the system. This is the property that gives rise to hydrodynamic behavior.

Two other properties of the DPD thermostat are important. Because the random and dissipative forces contribute to the stress in the system, the DPD thermostat enhances viscosity. Finally, the DPD thermostat is local, which means that the strength of the thermostat's interaction is strictly a result of local, rather than global conditions. This is in contrast to the Nose-Hoover thermostat[1], for example, which resets particle velocities based on the entire system's temperature. As a result, a discontinuity in the temperature in one part of the domain effects the behavior of the thermostat everywhere. If these properties can be conserved in a thermostat of a different form, then the dynamic properties of DPD that make it attractive for fluid modeling will be preserved.

2.3.1 The Anderson Thermostat

The Anderson thermostat[2] was originally developed for molecular dynamics simulations. It controls the temperature of the system by periodically exchanging the momentum of a particle with that of an imaginary particle from a thermal reservoir. Specifically, the momentum of system particles are replaced at random intervals with a value taken from a Maxwellian velocity distribution. This thermostat acts locally, as each thermostat

interaction affects just a single particle and does not depend on the global state of the system. From the perspective of DPD, the chief disadvantage of the Anderson thermostat is that momentum is not conserved, as each momentum exchange changes the system total.

Lowe suggested a modification to the Anderson thermostat in which particle pairs, rather than individual particles are thermalized. The relative velocity of the particle pair is replaced by a relative velocity taken from a Maxwellian distribution. The velocity of each particle in the pair is changed by an amount equal in magnitude, but opposite in sign, so that the centroid velocity of the pair is unchanged. As a result, the total momentum of each pair of particles is the same before and after the thermalization step, and total momentum is conserved.

2.3.2 Lowe-Anderson DPD Formulation

Based on this modification of the Anderson thermostat a new formulation of DPD is possible. The Lowe-Anderson formulation of DPD then, is made by the marriage of the modified Anderson thermostat to the integration scheme and conservative force law of the original Groot and Warren formulation. The dissipative and random forces introduced earlier are abandoned altogether, while the conservative force law is kept without modification. In the place of the dissipative and random forces, the Lowe-Anderson thermostat is inserted.

Moving from the DPD thermostat to the Lowe-Anderson thermostat obviates the need to choose γ, the strength of the dissipative force, which controls the strength of the viscous interaction. Instead, the modeler chooses a new parameter, Γ, which controls the frequency of particle pair thermalization events. For each particle pair with a separation distance less than the interaction range, for which $r_{ij} < r_c$, there is a probability defined by the quantity $\Gamma\Delta t$ of undergoing the thermal bath exchange process. This means that Γ is an absolute measure of the thermostatting frequency, without regard to the timestep size. We note, however, that there is a practical limit of the range of Γ that may be

employed. Each particle pair can be thermalized but once per timestep, so $\Gamma\Delta t$ has an upper limit of 1.

For those particle pairs which are selected, a new relative velocity along the vector connecting the particles is generated from a distribution $\xi_{ij}\sqrt{2k_BT}$ where ξ_{ij} is a Gaussian random number.

$$[\mathbf{v}_{ij}]' \cdot \mathbf{r}_{ij} = \xi_{ij}\sqrt{2k_BT} \tag{2.19}$$

The factor of $\sqrt{2}$ is included to reflect that the distribution is for relative velocities rather than for individual particle velocities. This new relative velocity replaces completely the previous velocity of the particles via

$$[\mathbf{v}_i]' = \mathbf{v}_i + \boldsymbol{\Delta}_{ij} \quad \text{and} \quad [\mathbf{v}_j]' = \mathbf{v}_j - \boldsymbol{\Delta}_{ij} \tag{2.20}$$

where the velocity update quantity $\boldsymbol{\Delta}_{ij}$ is calculated according to

$$2\boldsymbol{\Delta}_{ij} = \hat{\mathbf{r}}_{ij}\left([\mathbf{v}_{ij}]' - \mathbf{v}_{ij}\right) \cdot \hat{\mathbf{r}}_{ij}. \tag{2.21}$$

Let us now examine the question of how the Lowe-Anderson thermostat contributes to the fluid viscosity. The velocity update term described in Eq. 2.21 is an impulsive force, but it can be viewed instead as a force on the particles over the timestep given by

$$\mathbf{f}_{ij}^{LA} = \frac{\boldsymbol{\Delta}_{ij}}{\Delta t}. \tag{2.22}$$

If we take the example of a simple shear flow, we note that a particle pair that sits across a shear plane will on average, experience an impulsive thermostat force that retards the motion of the faster particle, and speeds up the slower particle. The impulse force can thus be understood to be acting as a viscous force. Making an argument based on the form of the stress-stress autocorrelation function, which predicts the zero-shear rate viscosity, Lowe predicts that the simple DPD fluid will have the following viscosity law:

$$\eta_0 = \frac{\pi\rho^2\Gamma r_c^5}{75m}. \tag{2.23}$$

In a similar fashion, the self-diffusion constant is predicted to follow

$$D \propto k_B T/\Gamma. \tag{2.24}$$

Taken together, we see that we can expect the Schmidt number of the Lowe-Anderson DPD fluid to depend on the square of Γ. A timestep of $\Delta t = 0.01$ allows us to access $Sc\tilde{}1800$, which is a significant improvement in the range of accessible Schmidt numbers over the original DPD formulation. The actual Schmidt number behavior of a LA-DPD fluid was investigated via non-equilibrium simulations by Symeonidis *et al.* [79], who showed that viscosity increases linearly with Γ, while the self-diffusion constant varies as Γ^{-1}, giving the predicted relationship that $Sc\tilde{}\Gamma^2$.

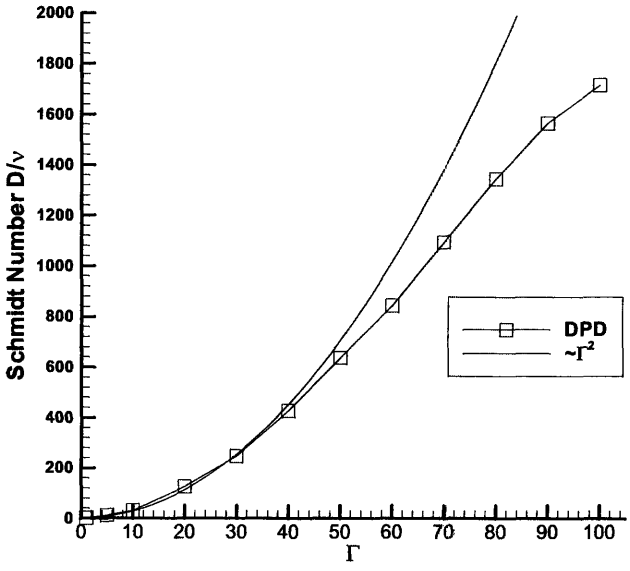

Figure 2-2: Behavior of the Schmidt number as a function of Γ with $\Delta t = 0.01$, data taken from [79]

A DPD particle with interaction radius $r_c = 1$ when $\rho = 4$ will, on average, have roughly 15 other DPD particles within its interaction sphere at each timestep. If we focus on the case illustrated in Figure 2-2, where $\Delta t = 0.01$. When $\Gamma = 50$, half of the particle pairs undergo a LA thermalization at each timestep. This means that the average particle undergoes more than 7 individual thermalization events at every timestep. This may seem like an excessively strong intervention, but it is worth keeping in mind that the centroid velocity of the particle pair is unchanged by the LA thermostat. This means that the likely effect of a single thermostat interaction is quite small. As Γ becomes quite large however, each particle is likely to be thermostatted many times at each timestep, and so it is not unreasonable to assume that there is a screening effect. The first thermostat interaction changes the final state of the particle more than the twelfth. This interpretation explains the fact that the measured Schmidt number does not follow exactly the Γ^2 heuristic as the value of $\Gamma\Delta t$ becomes large.

Table 2.1 gives explicitly the algorithm for implementing the Lowe-Anderson approach to DPD.

Lowe-Anderson DPD approach

1.) $\mathbf{v}_i(t + \frac{\Delta t}{2}) = \mathbf{v}_i(t) + \frac{1}{2}\mathbf{F}^C\Delta t$

2.) For all particle pairs for which $r_{ij} < r_c$
   i.) Generate a uniform random number ξ_{ij}
   ii.) If $\xi_{ij} < \Gamma\Delta t$, generate $[\mathbf{v}_{ij}]' \cdot \mathbf{r}_{ij}$ from a Maxwell Distribution $\xi_{ij}\sqrt{2k_BT}$
   iii.) $2\boldsymbol{\Delta}_{ij} = \mathbf{r}_{ij}\left([\mathbf{v}_{ij}]' - \mathbf{v}_{ij}\right) \cdot \mathbf{r}_{ij}$
   iv.) $[\mathbf{v}_i]' = \mathbf{v}_i + \boldsymbol{\Delta}_{ij}$
   v.) $[\mathbf{v}_j]' = \mathbf{v}_j - \boldsymbol{\Delta}_{ij}$

3.) $\mathbf{v}_i(t + \frac{\Delta t}{2}) = \mathbf{v}_i(t) + \frac{1}{2}\mathbf{F}^C\Delta t$

4.) $\mathbf{r}_i(t + \Delta t) = \mathbf{r}_i(t) + \mathbf{v}_i(t + \frac{\Delta t}{2})\Delta t$

5.) Calculate $\mathbf{F}^C$

Table 2.1: Implementation of Lowe-Anderson DPD Formulation

2.4 Polymers in DPD

From the earliest introduction of DPD, it has been observed that the model is ideal for incorporating macromolecules into DPD simulations. In particular, the DPD model strongly suggests by its structure a bead-spring or bead-rod model for constructing macromolecules, as the beads are already extant. Bead-spring models are more coarse-grained than macromolecules build with rigid connectors, so we will choose to focus on these, as DPD is a mesoscopic technique.

Bead-spring polymer models, as the name suggests, are constructed of a set of N beads connected by massless springs which impart a force on the beads between which they are connected. The mass of the polymer is concentrated in the beads, as is the interaction with the solvent. To create polymer molecules in a DPD simulation, we simply connect a series of DPD particles together with springs to form a linear chain, or any other polymer shape of our choosing.

A number of spring force models have been used for DPD polymers. The simplest is a Hookean spring constant, in which the force on the beads as a function of the spring vector $\mathbf{Q}$ is simply

$$\mathbf{F}^{Hookean} = H\mathbf{Q}. \tag{2.25}$$

Hookean springs are popular because analytical results can be calculated for many flows without resorting to stochastic simulations. While this model is quite successful at very low rates of strain, there is no limit on the extensibility of such springs, so the model gives unphysical results at large strain rates, as the bead-spring chains extend beyond the total length of the physical polymer molecule being studied. In order to address this shortcoming, we look instead to the finitely extensible non-linear elastic (FENE) spring[8], which incorporates a maximum spring extension Q_0. The FENE force law is given by

$$\mathbf{F}^{FENE} = \frac{H\mathbf{Q}}{1 - Q^2/Q_0^2}. \tag{2.26}$$

FENE springs are useful for modeling flexible polymers, and will be used throughout

this work.

In Brownian dynamics, the solvent is modeled as a continuum Newtonian fluid which imparts a hydrodynamic drag force and a random thermal force on the polymer beads. In a DPD system, the continuum solvent is replaced by an ensemble of DPD particles which are not themselves connected by springs, but are otherwise indistinguishable from the DPD beads used in constructing the polymer molecule itself. As in Brownian dynamics, the interaction between polymer and solvent is once again concentrated entirely in the polymer beads, as the springs do not "see" the solvent at all. That the DPD solvent is made of explicit particles rather than a field quantity results in a number of important differences in the way polymer simulations must be treated.

2.4.1 Length Scales

When the solvent is a continuum, as in BD, it carries with it no length scale. The length scale of the continuum is simply assumed to be "very small" in comparison to the polymer. As a result of this, the length scale of such a system is determined entirely by the characteristics of the polymer molecule, such as the spring law parameters. As we have seen with DPD, however, the particles themselves have an already-defined set of mass, length, time, and energy scales. While this set of scales is self-consistent, there is no systematic way of connecting DPD units with physical units. If a polymer molecule is built carefully, it can provide a translation between the DPD units described above and physical units. We will seek to do just that here, using as an example, polystyrene with molecular weight 500 kDa.

In physical units, our polymer molecule has a mass of $8.3 * 10^{-19}$ $g/molecule$. If our DPD polymer molecule model is composed of $N = 20$ beads, we know that the mass of a single DPD particle is $4.15 * 10^{-20}$ g. The density of the DPD system is 4 beads per unit volume, so the mass of a unit volume of DPD fluid is $1.66 * 10^{-19}$ g. If we assume a physical system density of 1 g/cm^3, we calculate that the length of one side of a DPD unit cube, $r_c = 5.5nm$. Having established a relationship between DPD and physical

length units, we must now determine the appropriate parameters in the DPD system to describe our polystyrene molecule with a bead-spring model.

2.4.2 Bead-spring Polymer Model

We will use a stepping-stone approach beginning with the physical polymer molecule, and specifying its representation as a freely-jointed bead-rod chain, or Kramers chain. From the Kramers chain, we can calculate the proper FENE bead-spring chain characteristics.

The Kramers Chain represents a linear flexible polymer molecule as a set of beads joined by rigid rods. The rods rotate freely at the bead points. The number of rods N necessary for the Kramers chain to describe a polymer can be determined from the molecular weight of the polymer, M_w, the molecular weight of the repeat unit, M_0, the bond angle of the carbon-carbon chain, θ, and the characteristic ratio, C_∞, which contains information about the chemical structure of the polymer backbone. McKinley[56] reports the following expression:

$$N = \frac{2M_w \sin^2(\theta/2)}{M_0 C_\infty} \tag{2.27}$$

With an estimate of $C_\infty = 9.6$, our 500 kDa polystyrene molecule requires 668 Kramers beads. The length of each rigid rod is given by

$$a = \frac{C_\infty l}{\sin(\theta/2)} \tag{2.28}$$

where l is the length of a carbon-carbon bond. For this polymer, $a = 0.415$ in DPD length units.

The Kramers chain can be related to a FENE bead spring chain as a function of a and N where, for a chain of M springs, the finite extensibility Q_0 is given by

$$Q_0 = \frac{(N-1)\,a}{M} \tag{2.29}$$

where we recognize that both $(N-1)\,a$ and MQ_0 are representations of the contour

length of the molecule. The spring constant for each spring is given by

$$H = \frac{3Mk_BT}{(N-1)\,a^2}. \tag{2.30}$$

If we choose to represent the molecule with a chain of 20 beads and 19 chains, these relations yield $Q_0 = 11.25$ and $H = 0.81$.

This development serves to establish a method for relating polymers described via DPD units to physical molecules, and to give an estimate as to the range of chain parameters which are appropriate to use when building model polymer molecules for simulation within DPD.

2.5 Extensions of DPD

There have been a number of important extensions of the DPD method which are not addressed in this thesis, but which are important for fully realizing the power of DPD's flexibility as a model. One can attach an additional energy variable to each DPD particle in order to create a form of DPD which conserves energy[4, 3, 18, 53, 68]. Alternately, the conservative force law can be altered to include both repulsive and attractive forces between particles[50, 81]. This allows liquid-gas interfaces to be simulated in theory.

Chapter 3

Non-Equilibrium Treatment of DPD Systems

Once the equations of motion have been chosen, and the thermostat is established, there remains the issue of actually running a simulation, and collecting the results. This chapter deals with the specific details of writing a DPD code to simulate solutions of polymer molecules.

3.1 Non-Equilibrium Molecular Dynamics

The tools for direct simulations of explicit particle models for fluids find their genesis in the field of non-equilibrium molecular dynamics. The original development of molecular dynamics included rules for the interactions of particles in an equilibrium setting, but did not provide for the imposition of a bulk flow. When a material is described by a continuum model, the entirety of the model is devoted to bulk motion. A continuum fluid at rest may have a temperature, a pressure, and a density, but it doesn't *do* anything. In contrast, a fluid at equilibrium in an explicit description is in constant motion, as the constituent particles move about ceaselessly. As such, the addition of bulk flow to an MD-type description of a fluid must be undertaken with special care, as we must now

describe two very different types of motion by the movements of but one ensemble of particles.

3.2 Periodic Boundary Conditions

Anytime one wishes to simulate a fluid with particles, one must establish a method of constraining the system, so that the constituent particles remain in a defined area. In a physical experiment, solid walls are frequently used to constrain a fluid, and a number of DPD workers have chosen this route, modeling solid walls with frozen DPD particles, simple reflection conditions, or more complicated schemes involving images of the particles in the domain. [82][28][25] Unfortunately, all of these methods lead to imperfect modeling of the very small-scale physical realities inherent in a solid-fluid boundary. Common problems include density and temperature fluctuations near the wall, as well as failure to reproduce a no-slip condition. As we are primarily interested in exploring the bulk rheological characteristics of DPD-modeled fluid systems, these artifacts present a significant challenge, as they reduce the volume of the simulated domain which is useful for confidently measuring material functions and configurational quantities.

In order to simulate only bulk flow we employ periodic boundary conditions in all three spatial dimensions to mimic an infinite bulk. Thus, a particle that leaves the domain will re-enter immediately on the other side. Surrounding the domain on all sides are infinite repeat images, each an exact replica of the primary domain. Sometimes, we will wish to describe features of the simulation which are more clearly expressed in the view that the domain is infinite. In those cases, a naming convention is important to keep track of which copy of the original domain we are referring to. Figure 3-1 illustrates this and gives the naming convention we will use to refer to specific periodic image domains. It is important to keep in mind that while many of the diagrams that follow will include pictures of the image domains that surround the primary, only the

velocities and positions of the particles in the primary domain are stored by the code. We will begin by describing the implementation of a DPD fluid at equilibrium, as this

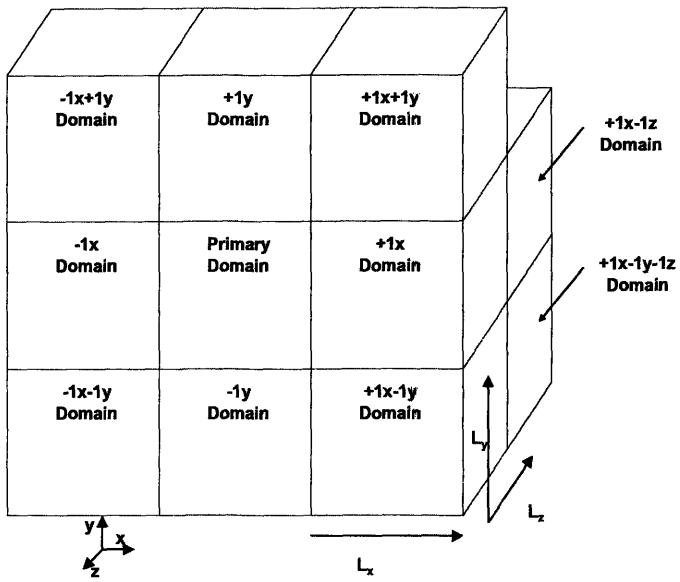

Figure 3-1: Schematic and naming conditions for periodic image domains. Each image domain is an exact replica of the primary domain, shifted by some multiple of the domain size vectors, L_x, L_y, and L_z.

is the simplest possible case, in terms of the steps required to deal with the periodic boundary conditions. There is no change in the relative positions of the periodic images with time. For the case of equilibrium simulations, a particle leaving the domain across the $-x$ boundary reappears instantaneously at the $+x$ boundary. Likewise, pairwise particle-particle interactions are communicated across periodic boundaries as well. This ensures that there is no discontinuity in the structure of the DPD fluid across a periodic boundary. When the DPD fluid is a polymer solution, so that DPD beads are connected by springs to create macromolecules, the orientation of individual springs, as well as molecular connectivity must be maintained across the periodic domain. While all of the techniques described here are commonly found in molecular dynamics programs, they

will be useful as a starting point when non-equilibrium treatment is considered.

3.2.1 Particle Position

After the position update step, the position of each particle is checked to see if it has left the domain. Any particle whose new position places it outside the bounds is returned to the domain by adding or subtracting L_i, the domain side length, from the particle's position. this process is illustrated in Figure 3-2. At equilibrium, the position of a particle in each dimension is independent of the other two, so there is no preferred order in which the dimensions must be checked for out-of-bounds particles. The explicit rules for the particle re-introduction are given formally in Eq. 3.1

$$\begin{aligned}
&if \quad r_{ix} > L_x \quad then \quad r_{ix} = r_{ix} - L_x \\
&if \quad r_{ix} < 0 \quad then \quad r_{ix} = r_{ix} + L_x \\
&if \quad r_{iy} > L_y \quad then \quad r_{iy} = r_{iy} - L_y \\
&if \quad r_{iy} < 0 \quad then \quad r_{iy} = r_{iy} + L_y \\
&if \quad r_{iz} > L_z \quad then \quad r_{iz} = r_{iz} - L_z \\
&if \quad r_{iz} < 0 \quad then \quad r_{iz} = r_{iz} + L_z
\end{aligned} \tag{3.1}$$

3.2.2 Particle Separation Distance

In all variations of molecular dynamics simulations, of which DPD is an example, one of the main computational costs is the calculation of interparticle distances. These are required to determine which pairs of particles will impart a force on each other. Without refinement, this is an $O(N^2)$ operation, as the separation distance for each pair of particles must be calculated. In order to reduce this cost, a linked cell list is used. The domain is divided into cubic cells with side length r_c, which is the interparticle interaction limit. The linked cell list contains a list of all the particles that inhabit each cell. For particle

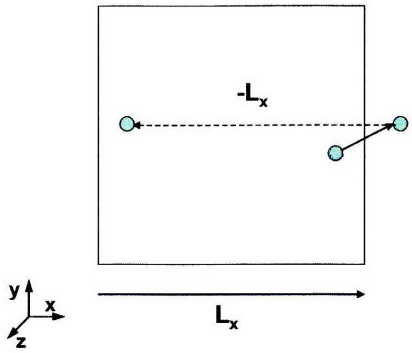

Figure 3-2: When a particle leaves the domain across the $+x$ boundary, it is returned by subtracting L_x from it's position vector r_i.

i found in cell A, only particles that are also found in cell A, or one of its immediate neighbors can be within its interaction sphere, so only those interparticle distances must be calculated, as pictured in Figure 3-3. In order to further improve the efficiency of the process, we note that particle pair distances need only be calculated once, so if particle i in cell A is found to have interparticle vector D_{ij} with particle j in cell B, there is no need to recalculate this value when the particles in cell B are considered. As such, an upwinding scheme is employed so that only half the neighboring cells need to be searched. Of the 26 cells that surround the test cell, all nine $(+1y)$ cells are searched, along with four cells in the $(+0y)$ plane. The upwinding scheme is illustrated in Figure 3-4. Cells that lie opposite each other across the periodic boundary are considered to be neighbors, so the effect of the boundary must also be taken into account. The interparticle distance vector is calculated as

$$\mathbf{D}_{ij} = \mathbf{r}_j - \mathbf{r}_i \tag{3.2}$$

where r_i and r_j are the position vectors of the two particles. The particle separation distance is $D = (\mathbf{D} \cdot \mathbf{D})^{\frac{1}{2}}$ A periodic boundary check must now be performed in each dimension to identify particle pairs that sit across a boundary. For these pairs, the

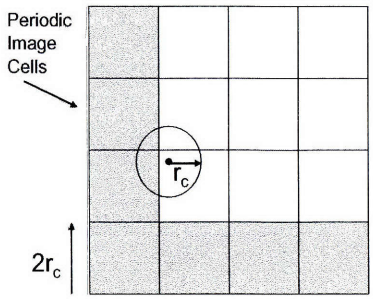

Figure 3-3: Linked celllist algorithm: by sorting the particles into cells of side length r_c, we reduce the number of particle pairs whose separation distance must be computed. The particles in any cell can only interact with particles found in neighboring cells.

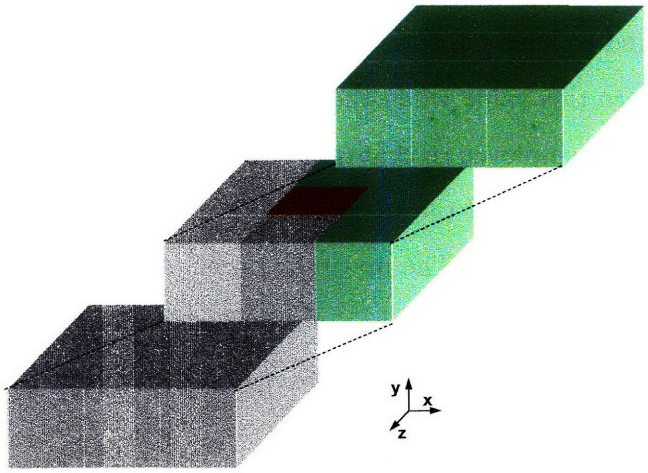

Figure 3-4: Illustration of the upwinding scheme used in the linked cell list algorithm; the test cell is shown in red, with cells which must be searched shown in green.

separation distance calculated via Eq. 3.2 will be large . Because we know that particles i and j came from adjacent cells, the maximum value for each component of $\mathbf{D}_{ij}$ is $2r_c$. We conclude that pairs for which a component of $\mathbf{D}_{ij} > 2r_c$ must lie across a periodic boundary. Thus the periodic boundary check is performed as:

$$\begin{aligned}
&if \quad D_{ijx} > 2r_c \quad then \quad D_{ijx} = D_{ijx} - L_x \\
&if \quad D_{ijx} < -2r_c \quad then \quad D_{ijx} = D_{ijx} + L_x \\
&if \quad D_{ijy} > 2r_c \quad then \quad D_{ijy} = D_{ijy} - L_y \\
&if \quad D_{ijy} < -2r_c \quad then \quad D_{ijy} = D_{ijy} + L_y \\
&if \quad D_{ijz} > 2r_c \quad then \quad D_{ijz} = D_{ijz} - L_z \\
&if \quad D_{ijz} < -2r_c \quad then \quad D_{ijz} = D_{ijz} + L_z
\end{aligned} \tag{3.3}$$

where L_i is the domain size in each dimension. When the fluid is at equilibrium in a cubic domain, the three spatial dimensions are independent of each other, so the periodic boundary check can be performed in any order.

3.2.3 Spring Length

The vector describing the length and direction of a polymer spring is given by $\mathbf{Q}_i = \mathbf{r}_{i+1} - \mathbf{r}_i$, leading to a spring length $Q = (\mathbf{Q} \cdot \mathbf{Q})^{\frac{1}{2}}$. In the presence of periodic boundary conditions, a check must be performed at each timestep to determine whether the spring in question crosses any periodic boundaries. We require that all springs have a maximum extension $Q_0 < 0.5L$ where L is the domain side length in the smallest dimension. With this limitation in place, any spring with $Q_i > 0.5L_i$ is assumed to lie across the periodic boundary in the i-direction. Thus we introduce a checking procedure which is similar to

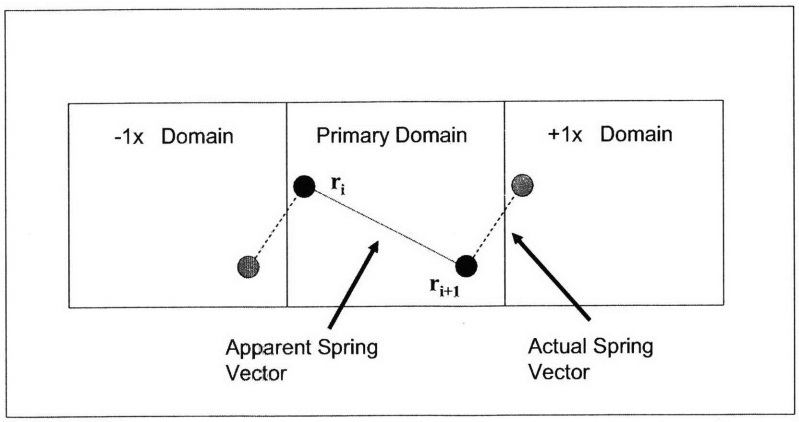

Figure 3-5: Springs which lie across the boundary can appear to be connected internally across the domain. We identify boundary crossing springs by their length.

Eq.3.3 for springs.

$$\begin{aligned}
&if \quad Q_{ix} > \tfrac{1}{2}L_x \quad then \quad Q_{ix} = Q_{ix} - L_x \\
&if \quad Q_{ix} < -\tfrac{1}{2}L_x \quad then \quad Q_{ix} = Q_{ix} + L_x \\
&if \quad Q_{iy} > \tfrac{1}{2}L_y \quad then \quad Q_{iy} = Q_{iy} - L_y \\
&if \quad Q_{iy} < -\tfrac{1}{2}L_y \quad then \quad Q_{iy} = Q_{iy} + L_y \\
&if \quad Q_{iz} > \tfrac{1}{2}L_z \quad then \quad Q_{iz} = Q_{iz} - L_z \\
&if \quad Q_{iz} < -\tfrac{1}{2}L_z \quad then \quad Q_{iz} = Q_{iz} + L_z
\end{aligned} \tag{3.4}$$

3.2.4 Molecular Configuration Calculation

Polymer molecules are represented in the model as bead-spring chains made up of DPD particles connected by springs. In the case of long chains containing a large number of beads, it is possible for a single molecule to stretch across several images of the periodic domain, as illustrated in Figure 3-6.

The radius of gyration of a molecule describes the volume occupied by the coil, and

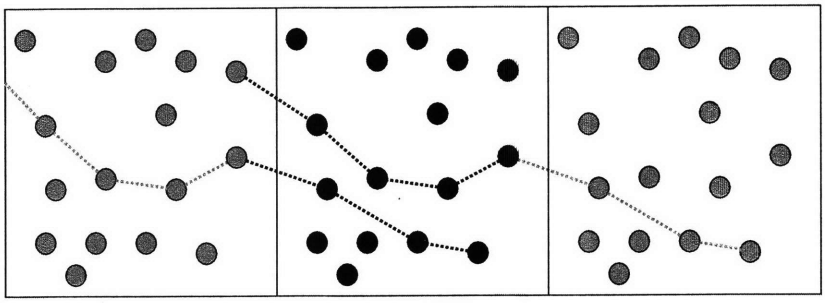

Figure 3-6: Macromolecule connectivity: a large polymer molecule may stretch across the domain several times. It is essential that the shape of the molecule as it would exist in an infinite bulk is understood and maintained. Here we picture one macromolecule, which belongs to the primary domain along with an image of it, which belongs to the image domain adjacent to the primary domain.

is defined as

$$R_G^2 = \sum_{i=1}^{N} (\mathbf{r}_i - \mathbf{r}_{CM})^2 \tag{3.5}$$

where N is the number of DPD particles, and $\mathbf{r}_{CM}$ is the center of mass of the polymer molecule. In order to correctly calculate this and other configurational quantities, it is essential to know the position of each bead relative to a fixed reference. We do this by assigning each particle a new virtual position $\widetilde{r}_i$

$$\widetilde{r}_i = r_i + \alpha_i L_x + \beta_i L_y + \gamma_i L_z \tag{3.6}$$

where α_i, β_i and γ_i are the number of times the molecule crosses the periodic boundary in each dimension between particle i and the reference particle. In this way, we can take into account instances when the polymer molecule has crossed a periodic boundary, and is thus larger than the domain. We customarily designate the first particle on the molecule to be the reference particle, so $\widetilde{r}_1 = r_1$. We then calculate the spring length vector $\mathbf{Q}_{r_2 r_1}$ between the first and second particles, and apply a boundary check process similar to that described in Eq. 3.4

If the spring crosses the $+x$ boundary, for example, α_2 is increased by 1. In this

manner each spring in the molecule is checked for boundary crossings, until every particle has been assigned a virtual position. Configurational quantities can then be calculated using the normal formulae. By treating the polymer molecules in this way, we allow ourselves the ability to simulate molecules with a contour length significantly longer than the domain size.

3.2.5 Center of Mass and Polymer Molecule Diffusion Constant

The polymer diffusion constant can be measured as a function of the mean squared displacement of the center of mass at long times. This quantity is calculated as

$$D = \frac{\langle (\mathbf{r}_{CM}(t) - \mathbf{r}_{CM}(0) \rangle}{6t} \tag{3.7}$$

for times longer than the longest relaxation time of the molecule. The virtual center of mass, which was used to calculate the radius of gyration, is given by

$$\widetilde{r}_{CM} = \frac{1}{N} \sum_{i=1}^{N} \widetilde{r}_i \tag{3.8}$$

This value is useful for calculating instantaneous configurational quantities such as the radius of gyration and end-to-end vector that are not related to the location of the center of mass of the polymer molecule, but it is important to keep in mind that $\widetilde{\mathbf{r}}_{CM}$ will not necessarily lie within the primary domain. Therefore, at each time step, one must also calculate the in-domain center of mass value. This is done by applying the particle boundary condition rules described in Section 3.2.1 to $\widetilde{\mathbf{r}}_{CM}$. We note that it can be necessary to add or subtract multiples of L if the virtual center of mass is more than one periodic image away from the primary domain. Finally, at each timestep we must compare the in-domain center of mass to its value at the previous timestep to determine whether r_{CM} has moved across a periodic boundary. So for each $r_{CM}(t)$, we associate $\alpha_{CM,t}$, $\beta_{CM,t}$, and $\gamma_{CM,t}$ to represent how many domain boundaries the polymer

molecule's center of mass has traversed since $t = 0$. Thus the polymer diffusion constant is calculated in our simulation as

$$D = \frac{\left\langle ((\mathbf{r}_{CM}(t) + \alpha_{CM,t}L_x + \beta_{CM,t}L_y + \gamma_{CM,t}L_z) - \mathbf{r}_{CM}(0) \right\rangle}{6t} \tag{3.9}$$

While none of the procedures described in this section are particularly complicated or unusual, it is worthwhile to become familiar with the standard rules for dealing with periodic domains, as they will have to be extensively modified when flows are introduced.

3.3 Shear Flow

We will begin by discussing the implementation of simple shear flow for DPD. A simple shear flow is defined by the velocity field

$$v_x = \dot{\gamma}_{xy} y; \qquad v_y = 0; \qquad v_z = 0 \tag{3.10}$$

pictured in Figure 3-7. The stress tensor for a simple shear flow is

$$\boldsymbol{\pi} = p\boldsymbol{\delta} + \boldsymbol{\tau} = \begin{pmatrix} p + \tau_{xx} & \tau_{yx} & 0 \\ \tau_{yx} & p + \tau_{yy} & 0 \\ 0 & 0 & p + \tau_{zz} \end{pmatrix} \tag{3.11}$$

From this, we measure three stress quantities of interest; the shear stress, τ_{yx}, the first normal stress difference, $\tau_{xx} - \tau_{yy}$, and the second normal stress difference, $\tau_{yy} - \tau_{zz}$. For the special case of steady shear flow, material functions can be defined for each of the aforementioned stresses. The viscosity η is dependent on the shear rate $\dot{\gamma}$ and is defined as

$$\tau_{yx} = -\eta(\dot{\gamma})\dot{\gamma}_{xy} \tag{3.12}$$

In a similar fashion, the first and second normal stress coefficients, Ψ_1 and Ψ_2 are

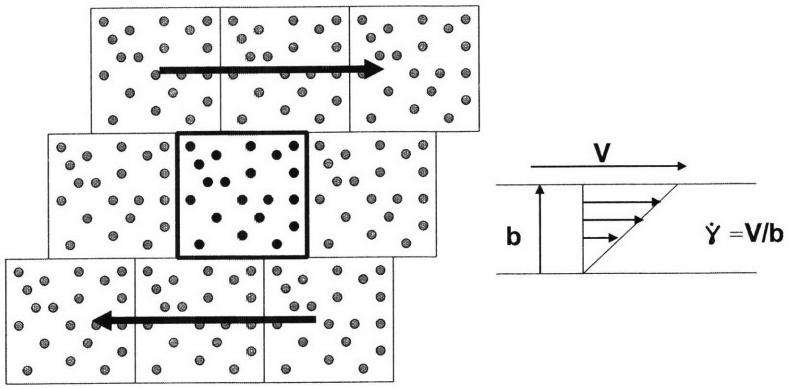

Figure 3-7: Lees-Edwards boundary conditions for shear flow: The periodic images of the domian in the shear directions move at the twice the fluid velocity at the boundary.

defined as

$$\tau_{xx} - \tau_{yy} = -\Psi_1(\dot{\gamma})\dot{\gamma}_{xy}^2 \tag{3.13}$$

and

$$\tau_{yy} - \tau_{zz} = -\Psi_2(\dot{\gamma})\dot{\gamma}_{xy}^2 \tag{3.14}$$

3.3.1 Lees-Edward Boundary Conditions

In this section we will describe the implementation challenges related to simulating shear flow with DPD. The most immediately apparent of these changes is the adoption of Lees-Edwards boundary conditions, which are an adaptation of the infinite periodic boundary conditions described in Section 3.2. At its most basic level, the concept behind Lees-Edwards boundary conditions is to have the $\pm y$ periodic images move relative to the primary domain, as illustrated in Figure 3-7. In order for the particles populating the region near the shearing boundary to experience a bulk flow, the mean velocity of the particles must be continuous across the boundary. We will refer to this quantity as the bulk solution velocity. As there are no absolute positions in a periodic simulation, we

will choose the midline of the primary domain to have bulk velocity $v_x = 0$. This results in a bulk velocity at the y-boundaries of $\pm v_{x \mid +y\ boundary} = \left(\dot{\gamma}_{xy} L_y\right)/2$. Matching the velocities across the periodic boundary gives the velocity of the $\pm y$ periodic images as $\pm \dot{\gamma}_{xy} L_x$. If we continue one domain further into the infinite bulk in the y-direction, the the velocity of the $+2y$-image domain will be $2\dot{\gamma}_{xy} L_x$. The movement of the periodic images also causes displacement of their positions relative to the primary domain. This introduces the first change that must be made to the original boundary rules. In the equilibrium case, a particle leaving the primary domain across the $+y$-boundary would be reintroduced with the only change being that $r_y = r_y - L_y$. Now, because there is a displacement of the image domains in the x-direction, the particle must be reintroduced with changes to both r_y and r_x. We define a new quantity δ_{LE}, the boundary offset, to describe this displacement. There are several ways to keep track of this value. First, we can simply define the quantity as the distance the periodic image has moved modulated by L_y.

$$\delta_{LE} = \dot{\gamma}_{xy} L_x t \mod (L_y) \tag{3.15}$$

This method works as long as the shear rate $\dot{\gamma}_{xy}$, is held constant. If one wishes to uses a variable shear rate $\dot{\gamma}_{xy}(t)$, one must update δ_{LE} at each timestep, performing a boundary check on it at each timestep as well.

$$\begin{aligned} \delta_{LE,t=0} &= 0 \\ \delta_{LE,t} &= \delta_{LE,t-\Delta t} + \dot{\gamma}_{xy} L_x \Delta t \\ if \quad \delta_{LE} > L_y\,, \quad \delta_{LE} &= \delta_{LE} - L_y \end{aligned} \tag{3.16}$$

Calculation of the Interparticle Distance

Having established the positions and velocities of the periodic image domains, we are ready to revise the linked cell list algorithm for calculating the distance between particle pairs described in Section 3.2.2. The cost savings from the cell list algorithm comes from being able to reduce the number of other particles that could potentially be within an

interaction radius of a given test particle, and whose separation distances with the test particle must be calculated. This in turn is dependent on knowing the identity of the neighboring cells that might house interacting particles. For the cells that lie adjacent to the moving boundary, the identity of "neighbor" cells will change with time. The assurance that one must search only one cell away in each direction is also lost, as the cells along the moving boundary will not reliably line up with each other. Fortunately, the entire confusing situation can be sidestepped for a relatively small additional computational cost. Rather than dealing directly with the shifting relationships between cells , we simply create an additional "phantom" row of cells that extend into the +y periodic image domains. This row of phantom cells is populated with phantom copies of the particles whose position $r_y < r_c$. That is, those particles that lie within one interaction distance of the shifting boundary. The new position of these phantom particles is given by

$$\begin{aligned} r_x &= r_x + \delta_{LE} \\ \text{if} \quad r_x > L_x \quad &\text{then} \quad r_x = r_x - L_x \\ r_y &= r_y + L_y \\ r_z &= r_z \end{aligned} \tag{3.17}$$

at this point, the normal linked celllist algorithm can be employed for the primary domain and the phantom row, with the exception that we disallow particle interactions across the y-boundary. Finally, all particle interactions that occur between two phantom particles are discarded. Interactions between a real particle and a phantom particle are kept, along with a notation that the interaction occurs across the moving boundary.

Thermostat Forces with Lees-Edwards Boundary Conditions

When calculating forces that depend on the relative velocity of the two particles, which include the dissipative force in traditional DPD, and the Lowe-Anderson velocity correction in that thermostat, one must take into account the differences in the absolute velocity across the moving boundary. When there exists a moving boundary, the relative

velocity between particles i and j is given by

$$v_{ij} = v_j - v_i + \beta(\dot{\gamma}_{xy} L_y) \tag{3.18}$$

where $\beta = 0$ for particle pairs that do not sit across the moving boundary, and $\beta = \pm 1$ if the particle pair does cross. The sign of β is determined by whether r_i or r_j was a phantom particle.

Spring Interactions

We now examine the process for resolving the length and direction vector of spring interactions. In most cases, this is accomplished as described in Section 3. The exception to this is for springs that lie across the moving y-boundary. First, a little nomenclature. Because we describe the motion of the periodic images using a positive quantity δ_{LE}, we will use the convention that the periodic image domain which is even with, or has already begun to move past the primary domain is considered the $(+1y)$-domain, while the trailing image domain is considered the $(-1x)\,(+1y)$-domain as in Figure 3-8 . When The position of the $(-1x)\,(+1y)$-domain draws even with the primary domain, $\delta_{LE} = 0$, and it is reassigned to be the $(+1y)$-domain. When a spring is found to lie across the moving boundary, we automatically assume that the spring extends into the $(+1y)$-domain. This will give the true result in cases such as the one illustrated in part a. of Figure 3-8. If the spring in fact extends into the $(-1x)\,(+1y)$-domain, as in part b. of Figure 3-8, one can see that Q_{iy} is correct, and Q_{ix} is simply off by L_x, an error that is corrected by performing the normal boundary crossing check for the x-boundaries. Because there is the possibility that a spring may be lying across both the x- and y-boundaries, we must apply the normal x-boundary check twice: once as an accompaniment to the y-boundary check, and once in case of a pre-existing x-boundary crossing. Furthermore, the y-boundary check should be performed first. Eq. 3.19 formalizes the procedure for checking for spring boundary crossings with Lees-Edwards boundary conditions.

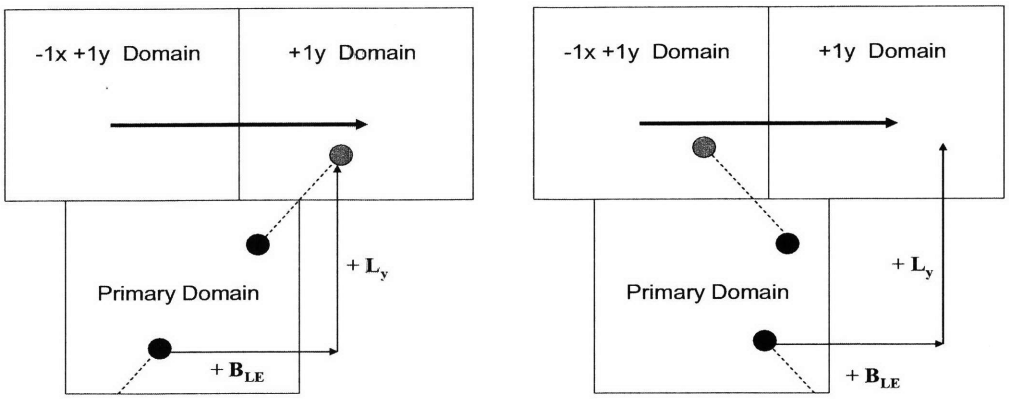

Figure 3-8: Two examples of springs crossing the moving LE boundary.

$$
\begin{array}{lll}
1. \quad if \quad Q_{iy} > \frac{1}{2}L_y & then & Q_{iy} = Q_{iy} - L_y \\
 & & Q_{ix} = Q_{ix} - \delta_{LE} \\
2. \quad if \quad Q_{iy} < -\frac{1}{2}L_y & then & Q_{iy} = Q_{iy} + L_y \\
 & & Q_{ix} = Q_{ix} + \delta_{LE} \\
3. \quad if \quad Q_{ix} > \frac{1}{2}L_x & then & Q_{ix} = Q_{ix} - L_x \\
4. \quad if \quad Q_{ix} < -\frac{1}{2}L_x & then & Q_{ix} = Q_{ix} + L_x \\
5. \quad if \quad Q_{ix} > \frac{1}{2}L_x & then & Q_{ix} = Q_{ix} - L_x \\
6. \quad if \quad Q_{ix} < -\frac{1}{2}L_x & then & Q_{ix} = Q_{ix} + L_x \\
7. \quad if \quad Q_{iz} > \frac{1}{2}L_z & then & Q_{iz} = Q_{iz} - L_z \\
8. \quad if \quad Q_{iz} < -\frac{1}{2}L_z & then & Q_{iz} = Q_{iz} + L_z
\end{array}
\tag{3.19}
$$

3.4 Shearfree Flow

Simple shearfree flows are defined by the velocity field

$$v_x = -\frac{1}{2}\dot{\varepsilon}\,(1+b)\,x \tag{3.20}$$

$$v_y = -\frac{1}{2}\dot{\varepsilon}\,(1-b)\,y \tag{3.21}$$

$$v_z = \dot{\varepsilon} z \tag{3.22}$$

where $\dot{\varepsilon}$ is the elongation rate. The parameter b ranges from $0 \leq b \leq 1$, and determines the direction in which the shearfree flow operates. For specific choices of b, special shearfree flows are obtained:

Elongational Flow:	$b = 0,\ \dot{\varepsilon} > 0$
Biaxial Stretching Flow:	$b = 0,\ \dot{\varepsilon} < 0$
Planar Elongation Flow:	$b = 1$

A steady shearfree flow is one which for which $\dot{\varepsilon}$ does not vary in time. In order to simulate a steady shearfree flow of a polymer solution, the simulation must run until the molecules have reached a steady configuration, and the stresses have been constant for a long time, during which an average can be taken. Shearfree flows are distinguished from many other flows in that neighboring fluid elements move away from each other at an exponential rate. As Bird et. al. note, two fluid elements initially separated by a distance l_0 will be separated by a distance l after time Δt, such that

$$l = l_0 e^{\dot{\varepsilon}\Delta t} \tag{3.23}$$

Fluid elements which may contain parts of a macromolecule separate from each other much faster in elongational flow than is typical in shear flows. The result of this is that macromolecules typically experience much greater deformations in shearfree flows than

in shear flows at similar strain rates.

The stress tensor for a shearfree flow is

$$\boldsymbol{\pi} = p\boldsymbol{\delta} + \boldsymbol{\tau} = \begin{pmatrix} p+\tau_{xx} & 0 & 0 \\ 0 & p+\tau_{yy} & 0 \\ 0 & 0 & p+\tau_{zz} \end{pmatrix}. \tag{3.24}$$

From this, we measure two stress quantities of interest; $\tau_{zz} - \tau_{xx}$ and $\tau_{yy} - \tau_{xx}$, which lead to two viscosity functions,

$$\tau_{zz} - \tau_{xx} = -\bar{\eta}_1(\dot{\varepsilon}, b)\dot{\varepsilon} \tag{3.25}$$

and

$$\tau_{yy} - \tau_{xx} = -\bar{\eta}_2(\dot{\varepsilon}, b)\dot{\varepsilon} \tag{3.26}$$

3.4.1 Explicit Particle Simulations

Simulation techniques that model polymer solutions as explicit particles which are assigned a physical location face a series of difficulties that do not arise in continuum simulations or even in Brownian dynamics simulations of dilute polymers. When the fluid is a continuum, its properties are governed by inputs specified by the modeler. Even inflow and outflow boundaries do not present a challenge. One simply specifies the fluid state. In explicit methods, such precision is not possible. The temperature, pressure, velocity, and even the structure of the fluid, as described by the radial gyration function, are determined by the positions and velocities of the individual particles. As a result, special care must be taken to ensure that particles that leave the simulation domain are reintroduced in such a way as not to change the properties of the fluid. Periodic boundary conditions are ideal for overcoming this difficulty, because there is no beginning or end to the domain.

Periodic boundary conditions are easily adapted to the simulation of unidirectional

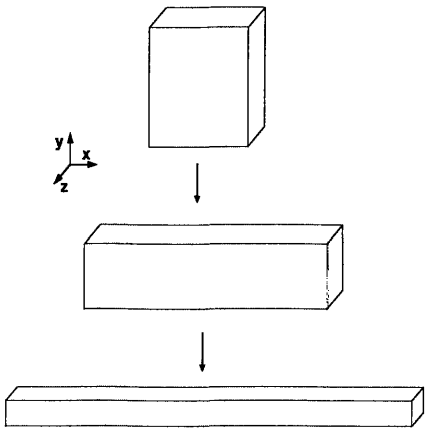

Figure 3-9: Simulating planar elongational flow in a rectangular periodic domain. In order to satisfy the mass balance, the borders must move with the flow. After a short time, the contacting dimension grows smaller than the minimum distance required to resolve the orientation of polymer springs.

shear flow because the mass balance across opposing (or, in another view, adjacent) boundaries are naturally satisfied. The number of particles entering the domain at one boundary is always equal to the number leaving the opposite side, regardless of the shear rate. Flows which are not unidirectional do not have it so easy. We take as an illustrative example a cubic domain undergoing planar elongational flow ($b = 1$), pictured in Figure 3-9. The stagnation point is at the origin in the middle of the domain. The fluid velocity in the y-direction is $v_y = -\dot{\epsilon}y$, thus the flowrate across the $+y$-boundary into the domain is $0.5L_y\dot{\epsilon}$. The inflow at the $-y$-boundary is the same. In order to resolve this problem and restore the mass balance across opposing boundaries, the domain must deform affinely with the flow. Unfortunately, this severely limits the time duration over which one can run a simulation, as the size of the domain in the contracting dimension will quickly reach its minimum length, which for a polymer solution is half the maximum spring extension. As we are seeking to simulate polymer chains with very long relaxation times, this limitation is severe. This is particularly true if we wish to study steady elongational flow, as a long

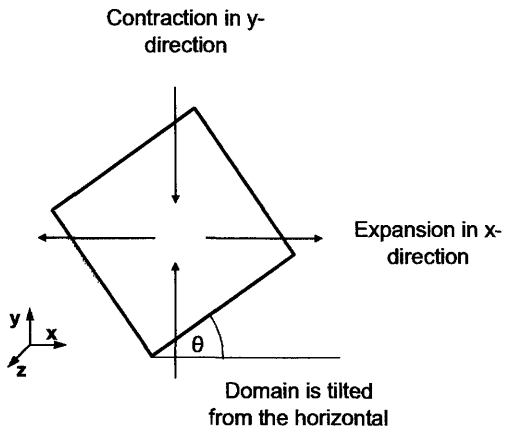

Figure 3-10: Diagram of Kraynik and Reinelts planar elongational flow cell. The cell is periodic in all three dimensions, and is tilted with respect to the flow axes by and angle θ.

initialization period is frequently required for the macromolecules to assume their highly deformed shapes.

3.4.2 Kraynik and Reinelt Boundary Conditions

Kraynik and Reinelt have devised a periodic unit cell for planar elongation flow which is able to avoid the problem of finite time limitation described above for a rectangular periodic domain. They begin with a square, spatially periodic domain, which is tilted with respect to the axes of elongation by an angle θ, as pictured in Figure 3-10. A planar elongational flow is then applied as defined in standard Cartesian coordinates, and the domain boundaries deform affinely with the flow, expanding in the z-direction and contracting in x. This ensures that the flux of particles across the periodic boundaries is zero. There is no flow in the y-direction, so the periodicity of the fluid in that direction is unaffected. From this point on, we will describe the method in terms of the $z-$ and $x-$ dimensions only, as there is no interesting behavior in the neutral $y-$direction. Kraynik

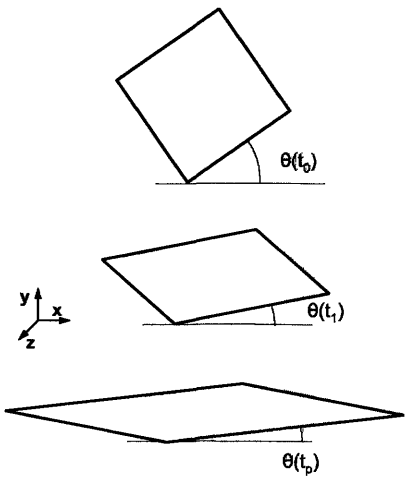

Figure 3-11: Progression of the deformation of a Kraynik and Reinelt periodic cell undergoing planar elongational flow. The angle $\theta(t)$ that the domain makes to the horizontal changes as the cell is deformed.

and Reinelt show that for several discrete values of θ, this arrangement leads to spatial as well as temporal periodicity, so that at a Hencky strain of ϵ_p, there exists in the domain a set of internal boundaries which coincide with the original domain boundaries as they were at $t = 0$. At this point, the original boundaries are re-established, and the particles which are found to lie outside the (new) domain are reintroduced via the normal periodic boundary rules described in Section 3.2. Table 3.27 gives the first few orientations found by Kraynik and Reinelt to exhibit periodicity in Hencky strain.

Case	ϵ_p	θ
1	0.96242	0.553574
2	1.762747	0.392699
3	2.389526	0.294001
4	2.703576	0.613886

(3.27)

In practice it is common to choose case 1, as it has the shortest period, and thus results in the least deformed domain at the resetting point. The original rotated square becomes a highly elongated parallelogram at ϵ_p, at which point the distance between the periodic boundaries is at a minimum. It is this distance that limits the allowable maximum spring extension.

3.4.3 Implementation of KR Boundary Conditions in DPD

Application of the periodic boundary conditions to the rotated domain shown in Figure 3-10 involves a great deal of awkward and inefficient computation, as the boundaries are continuously shifting in relation to the $x - z$ plane that defines the flow field. Todd and Daivis have suggested that for purposes of applying the periodic boundary conditions, the whole domain may be rotated clockwise as in Figure 3-12 until one of the boundaries is parallel to the $z-$axis. The angle at which the domain is offset from the z-axis, $\theta(t)$,

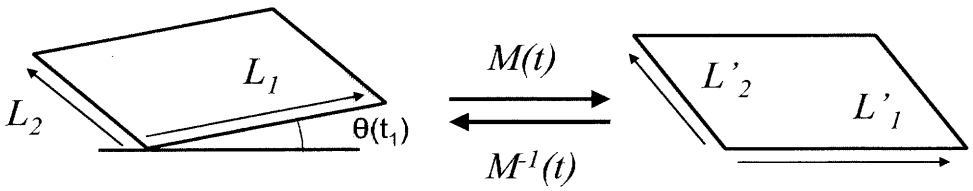

Figure 3-12: Rotation of the KR periodic domain into the calculation-friendly orientation.

begins at the value given in Table 3.27, and is reduced as the domain is elongated. The rotation is effected by applying a coordinate transformation to the positions of the particles,

$$\mathbf{r}_i' = \mathbf{M}(t)\mathbf{r}_i \tag{3.28}$$

where $\mathbf{r}_i'$ is the new transformed position. The transformation matrix $\mathbf{M}(t)$ is defined as

$$\mathbf{M}(t) = \begin{pmatrix} \cos\theta(t) & \sin\theta(t) \\ -\sin\theta(t) & \cos\theta(t) \end{pmatrix} \tag{3.29}$$

which serves to rotate the particle positions by an angle $-\theta(t)$ about the y-axis. The rotated reference frame simplifies considerably the application of the periodic boundary conditions. In the true orientation, a particle's position relative to any domain or cell boundary was a function of both the x and z-dimensional coordinates, as well as the orientation angle $\theta(t)$. In the rotated frame of reference, having one boundary parallel to the z-axis allows us to describe a particle's position relative to one of the boundaries as a function of a single dimensional coordinate, $\mathbf{r}_x'$. This new reference frame is useful for more easily calculating the distance vectors between particle pairs for the conservative force D_{ij}, as well as the spring connector vectors Q_i, because the absolute positions of the particles are not important, as long as the separation distances are faithfully maintained through the coordinate transformation. Before any particle dynamics calculations can be performed, the domain must be rotated back to its natural position by appling the inverse transformation,

$$\mathbf{r}_i = \mathbf{M}^{-1}(t)\mathbf{r}_i' \tag{3.30}$$

which rotates the domain through the orientation angle $\theta(t)$ about the y-axis. The inverse transformation $\mathbf{M}^{-1}(t)$ is given by

$$\mathbf{M}^{-1}(t) = \begin{pmatrix} \cos\theta(t) & -\sin\theta(t) \\ \sin\theta(t) & \cos\theta(t) \end{pmatrix} \tag{3.31}$$

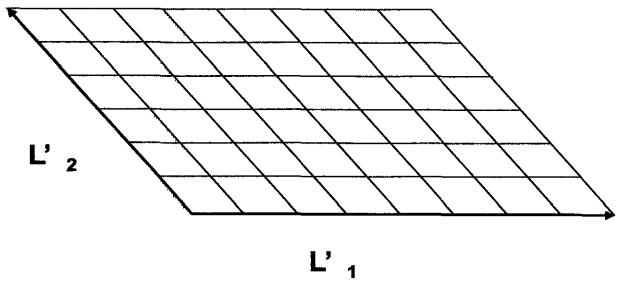

Figure 3-13: Diagram of Kraynik and Reinelt domain rotated into the periodic friendly frame, and subdivided into cells for particle sorting. Here $a = 8$ and $b = 6$.

Calculation of Particle Pair Separation in the Rotated Reference Frame

The linked celllist technique for calculating particle pair separation distances described in Section 3.2.2 is applied in nearly the same fashion for KR boundary conditions as for standard Cartesian periodic boundary conditions at equilibrium, with the exception that the component cells into which the domain is subdivided are not always rectangular. Rather, the vectors that define each cell, $L_1^{'(cell)}$ and $L_2^{'(cell)}$, must be fractions of the domain boundary vectors such that

$$aL_1^{'(cell)} = L_1' \quad \text{and} \quad bL_2^{'(cell)} = L_2' \tag{3.32}$$

where a and b are integers. This ensures that the domain will be divided into a whole number of equally-sized cells. The sorting cells deform to follow the shape of the domain as a whole. This arrangement ensures that the cells which are in communication with each other across periodic boundaries will maintain the same neighbor relationships as the domain elongates. Smaller individual cells lead to greater computational savings, so it is desirable to set a and b as large as possible. At $t = 0$, when the rotated domain is rectangular, the individual cells are cubes of side length r_c, because the shortest distance

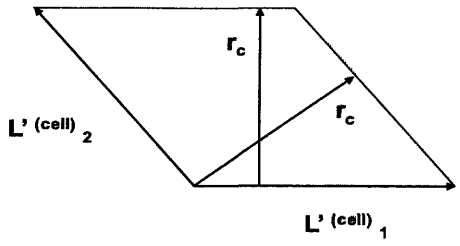

Figure 3-14: Minimum dimensions for sorting cells: The distance between parallel boundaries of the cell must always be greater than the DPD particle intercation distance r_c.

across the cell is in the Cartesian directions. As the cell begins to elongate with the domain, this minimum distance changes as well. For a parallelogram-shaped cell, we require that the distance between each pair of opposing parallel sides be greater than the particle interaction length r_c as illustrated by Figure 3-14.Necessarily, as the domain becomes more elongated, a and b, the number of cells in each dimension, is reduced. With more particles in each cell, the number of particle pairs whose separation distance must be calculated increases, and the time savings realized from using the linked celllist algorithm is less and less. For this reason, we are further motivated to choose Case 1, which results in the least deformed domain at the resetting point.

The rules governing particle pairs that sit astride periodic boundaries are the same for KR boundaries as they are for standard cubic periodic domains, as described in Section 3.2.2 with the exception that L_x and L_y are replaced by L_1' and L_2', which are not perpendicular to each other. We also note that because we are calculating the pair

distances in a rotated frame, $\mathbf{D}'_{ij}t$. It is much simpler to test

$$\begin{aligned}
&if \quad D'_{ijx} > 2r_c \quad then \quad \mathbf{D}'_{ij} = \mathbf{D}'_{ij} - \mathbf{L}_2 \\
&if \quad D'_{ijx} < -2r_c \quad then \quad \mathbf{D}'_{ij} = \mathbf{D}'_{ij} + \mathbf{L}_2 \\
&if \quad D'_{ijz} > 2r_c \quad then \quad \mathbf{D}'_{ij} = \mathbf{D}'_{ij} - \mathbf{L}_1 \\
&if \quad D_{ijz} < -2r_c \quad then \quad \mathbf{D}'_{ij} = \mathbf{D}'_{ij} + \mathbf{L}_2 \\
&if \quad D_{ijy} > 2r_c \quad then \quad D_{ijy} = D_{ijy} - L_y \\
&if \quad D_{ijy} < -2r_c \quad then \quad D_{ijy} = D_{ijy} + L_y
\end{aligned} \tag{3.33}$$

Calculation of Spring Distance

The issue of correcting boundary crossings is relatively easy for the case of particle pair distances, because the linked celllist algorithm identifies which pairs of particles interact across a boundary. When calculating spring lengths, this information is not available, so a separate check must be performed. In the rotated reference frame, the domain's z'-dimension length is given by $L'_{1z'}$ and the length of the x'-dimension is $L'_{2x'}$. We check for springs whose x' projection crosses a boundary first, because the resultant correction affects both $Q_{x'}$ and $Q_{z'}$. In that case $Q_{x'}$ is adjusted by $\pm L'_{2x'}$ and $Q_{z'}$is adjusted by $L'_{2z'}$. Following this step, crossings in the z'-direction are detected. The periodic boundary in the y-direction is independent and can be performed at any time. The spring length

correction algorithm is summarized in Table 3.34.

$$
\begin{array}{lll}
1. \quad if \quad Q_{ix'} > \frac{1}{2}L'_{2x'} & then & Q_{ix'} = Q_{ix'} - L'_{2x'} \\
 & & Q_{iz'} = Q_{iz'} - L_{2z'} \\
2. \quad if \quad Q_{ix'} < -\frac{1}{2}L'_{2x'} & then & Q_{ix'} = Q_{ix'} + L'_{2x'} \\
 & & Q_{iz'} = Q_{iz'} + L_{2z'} \\
3. \quad if \quad Q_{iz'} > \frac{1}{2}L'_{1z'} & then & Q_{iz'} = Q_{iz'} - L'_{1z'} \\
4. \quad if \quad Q_{iz'} < -\frac{1}{2}L'_{1z'} & then & Q_{iz'} = Q_{iz'} + L'_{1z'} \\
5. \quad if \quad Q_{iy} > \frac{1}{2}L_y & then & Q_{iy} = Q_{iy} - L_y \\
6. \quad if \quad Q_{iy} < -\frac{1}{2}L_y & then & Q_{iy} = Q_{iy} + L_y
\end{array}
\tag{3.34}
$$

Reintroduction of Particles

After the position update step, the position of some particles will be outside the simulation domain, so they must be reintroduced. The first step in doing so is actually identifying which particles are no longer within the domain. This is most easily accomplished in the rotated periodic-friendly orientation. Here we check first for particles that have left the domain in the x direction, as this is straightforward and a function of r_{ix} only. Any particle for which $r'_{ix} < 0$ or $r'_{ix} > L'_{2x}$ is no longer within the simulation domain. Reintroduction requires a modification of both r_{iz} and r_{ix}. In the z-direction, a particle is outside the domain if

$$
r'_{iz} + \left(r'_{ix} \frac{L'_{2z}}{L'_{2x}} \right) < 0 \quad \text{or} \quad r'_{iz} + \left(r'_{ix} \frac{L'_{2z}}{L'_{2x}} \right) > L'_{1z} \tag{3.35}
$$

where the additional term accounts for the slope of the L'_2 boundary vector. Reintroduction of the particle then requires only a modification in r'_{iz}. The rules for particle reintroduction are summarized in table 3.36 in the order in which they must be imple-

mented.

$$\begin{aligned}
\text{if } r'_{ix} < 0 \qquad & r'_{ix} = r'_{ix} + L'_{2x} \\
& r'_{iz} = r'_{iz} + L'_{2z} \\
\text{if } r'_{ix} > L'_{2x} \qquad & r'_{ix} = r'_{ix} - L'_{2x} \\
& r'_{iz} = r'_{iz} - L'_{2z} \\
\text{if } \; r'_{iz} + \left(r'_{ix}\frac{L'_{2z}}{L'_{2x}}\right) < 0 \qquad & r'_{iz} = r'_{iz} + L'_{1z} \\
\text{if } \; r'_{iz} + \left(r'_{ix}\frac{L'_{2z}}{L'_{2x}}\right) > L'_{1z} \qquad & r'_{iz} = r'_{iz} - L'_{1z} \\
\text{if } \; r_{iy} < 0 \qquad & r_{iy} = r_{iy} + L_y \\
\text{if } \; r_{iy} > L_y \qquad & r_{iy} = r_{iy} - L_y
\end{aligned} \tag{3.36}$$

Updating the Border Vectors

At each timestep, the shape of the domain must be updated to reflect the deformation of the fluid contained within it. This operation is undertaken in the natural (tilted) reference frame, and is accomplished by recalculating the border vectors according to

$$\mathbf{L}_1(t') = \mathbf{L}_1(0)e^{\dot{\epsilon}t'} \text{ and } \mathbf{L}_2(t') = \mathbf{L}_2(0)e^{\dot{\epsilon}t'} \tag{3.37}$$

We note that t' here denotes the time that has elapsed since the most recent domain resetting operation, rather than that absolute time elapsed. In addition to resetting the domain vectors, a new value for θ is calculated with

$$\theta(t') = \tan^{-1}\left(\frac{\mathbf{L}_{1x}(t')}{\mathbf{L}_{1z}(t')}\right) \tag{3.38}$$

the rotated periodic-friendly domain vectors are also recalculated, according to

$$\mathbf{L}'_i = \mathbf{M}(t)\mathbf{L}_i \tag{3.39}$$

as well as the number of cells to be employed in the linked celllist algorithm. Upon changing the shape of the simulation domain, it is inevitable that a certain number of

particles will find themselves outside of the domain borders, and must be re-introduced. It is important that the deformation of the domain is truly affine, and that the stagnation point that exists at the center of the domain is maintained at the same point. The domain's origin is set at the intersection of L_1 and L_2 so that the domain rotates about the origin when we transition from the natural to the periodic-friendly orientation. For correct affine deformation however, it is more convenient if the origin is at the stagnation point. To that end, before the resizing step is taken, the position of each particle is updated according to

$$\mathbf{r}_i = \mathbf{r}_i - \left(\frac{1}{2}L_1(t' - \Delta t) + \frac{1}{2}L_2(t' - \Delta t)\right) \tag{3.40}$$

which effectively resets the origin to the center of the domain. After the new border vectors have been calculated, the origin is returned to the intersection of the border vectors via

$$\mathbf{r}_i = \mathbf{r}_i + \left(\frac{1}{2}L_1(t') + \frac{1}{2}L_2(t')\right) \tag{3.41}$$

We assure ourselves that the domain is deforming about the stagnation point by checking to ensure that an equal number of particles are found outside each pair of periodic boundaries at each time step. This implies that the area swept out by each moving boundary is equal.

Resetting the Domain

After the fluid has reached ε_p, the critical Hencky strain, the domain must be reset back to the original configuration so that the process can begin all over again. In order to achieve true temporal periodicity the resetting step must not change anything about the configuration of the constituent particles. All particle pairs which existed previously must be preserved, and the total stress-state of the system must not undergo any sudden dislocations. In order to demonstrate that these conditions are met, we look at the domain before and after the resetting process as an exchange between internal and external

periodic boundaries. The concept is illustrated for a static square domain in Figure 3-15. If a periodic domain is repeated infinitely in every direction, then the information

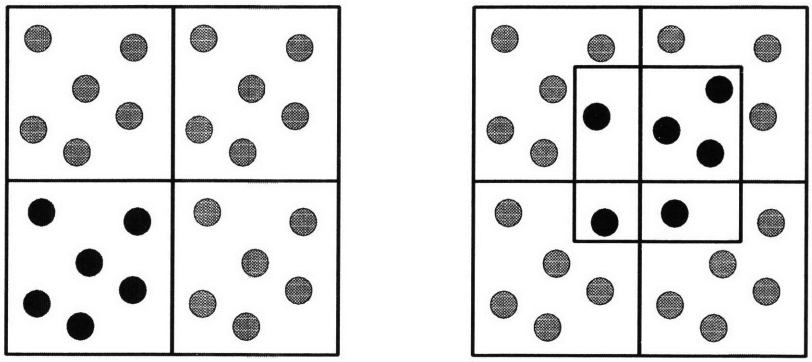

Figure 3-15: If a periodic domain is viewed as an infinite bulk, the location of the domain boundaries themselves can be changed arbitrarily without changing the structure of the system. In part a.) the dark box is the primary domain, while in part b.) the primary domain has been reassigned, without changing any particle pair relationships, or altering the number and identity of the particles in the primary domian.

contained in the primary domain is also available as a combination of a portion of the primary domain, and a portion of adjacent image domains. The relationship between particles that lie across a periodic boundary is no different than the relationship between particles separated by any arbitrary plane cut through the domain. As this is true, reassigning where the periodic boundaries cut through the infinite bulk has no effect of the structure of the fluid. This is the process by which the KR domain is reset, although the geometry is less straightforward. Figure 3-16 shows the infinite bulk before deformation, with the highly elongated domain superimposed. The resetting step is simply a redrawing of the location of the periodic boundaries. After the boundaries are reset, application of the periodic boundary conditions return all the particles to the inside of the primary domain.

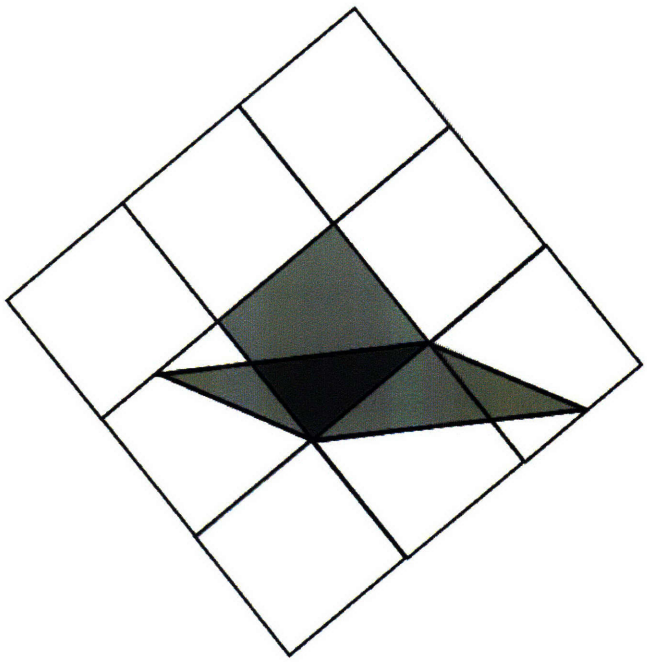

Figure 3-16: The infinte bulk formed by the primary domain and its surrounding repeat images. The primary domian before and after the KR reset step are shaded.

Imposition of Planar Elongational Flow

The Kraynik and Reinelt boundary conditions provide a framework within which simulation of planar elongational flow is possible. They describe the movement of the boundaries of the domain, so that a fluid which is undergoing planar elongational flow can be contained without intruding on the dynamics of the flow itself. This is a necessary, but is not sufficient condition for successful simulation. We have yet to discuss the forces that will actually cause the DPD particles to move in the manner we wish. At first glance, it may appear that this can be accomplished simply by moving the boundary conditions. At each timestep, as the boundaries change shape, particles that are swept out of the domain are reintroduced along the opposite boundary. There will form areas of higher density where the boundaries are contracting, and areas of lower density where the boundaries are expanding. This method of flow imposition will work as long as the rate of deformation is much smaller than the rate at which the system responds to density fluctuations, which can be interpreted as the speed of sound in the fluid. In the case of DPD, this condition does not generally hold true. By grouping large numbers of solvent molecules into DPD particles, the speed of sound is reduced significantly, and the fluid's response to density gradients is slowed down. (This is yet another result of the fact that the Schmidt number for DPD is much smaller than that of physical liquids.) An analogous physical picture is that of a box of gas which is deforming via the KR boundary conditions. As the box expands, the velocity of the outermost point will be given by $v = e^x$. When this value is larger than the rms velocity of the gas molecules, there will form an area of low density. In summary, the DPD particles simply do not move fast enough on their own accord to keep pace with the deformation of the domain at its edges. As a result, simulating a planar elongational flow using only the KR boundary conditions results in nonhomogeneous density distributions, as well as a strong box-size dependence. This problem has been addressed in the past by workers in Non-equilibrium Molecular Dynamics (NEMD), so we will take a cue from them, and add to our simulation the SSLOD equations of Evans and Morriss.

The SSLOD Equations

The SSLOD equations, so named because they are an adaptation of an earlier formulation called DOLLS, are a technique for imposing a flow field on a fluid made up of discrete particles. It is essential that the SSLOD equations be implemented in concert with appropriate boundary conditions, such that no gradients exist at the domain boundaries. From a qualitative standpoint, the SSLOD equations simply assume that a flow field is in existence, and then forces are added to the particles such that they conform to the assumed flow field. In this way, a non-equilibrium system is created in which the constituent particles behave much as they would in an equilibrium setting, except that they are in bulk motion. The SSLOD equations of motion are

$$\dot{\mathbf{r}}_i = \frac{\mathbf{p}_i}{m_i} + \mathbf{r}_i \cdot \boldsymbol{\nabla}\mathbf{v} \tag{3.42}$$

and

$$\dot{\mathbf{p}}_i = \mathbf{F}_i - \mathbf{p}_i \cdot \boldsymbol{\nabla}\mathbf{v} \tag{3.43}$$

where once again we note that in the case of our DPD simulations, m_i is always equal to unity, so that $\mathbf{p}_i$ can always be viewed simply as the velocity. The SSLOD equations are best understood as a modification of Newton's equations of motion to take into account a background flowfield. The second term in Eq. 3.42 forces the particle's position to change with the applied flow field, while the extra term in Eq. 3.43 adjusts the particle's velocity to account for the unnatural change in position. The SSLOD equations were developed to allow for the simulation of non-steady state shear flow, in a way that would allow the fluid to respond instantaneously to changes in the shear rate. It is, however, applicable to any flow field for which appropriate periodic boundary conditions can be developed.

The introduction of the SSLOD equations gives us two sets of velocity with which to contend, and it is important that we are clear as to which is being used at what time.

First, there is an absolute velocity, $\frac{d\mathbf{r}_i}{dt}$ which we will call the laboratory velocity, as this is the speed which would be measured by a stationary observer. The second is called the peculiar velocity, given by $\mathbf{p}_i$ in the above equations, which is the particle's velocity relative to the applied flow field. We define a streaming velocity field $\mathbf{v}(\mathbf{r}) = \mathbf{r} \cdot \nabla \mathbf{v}$ which is called the zero wavevector profile. In a laminar flow this is simply the bulk velocity field. The temperature is defined in terms of the peculiar velocity, so that the position of a particle within the flow field does not affect its contribution. The Lowe-Anderson thermostatting forces, however, must be calculated using the laboratory velocity, or else no net shear stress will result, and the thermostat will contribute nothing to fluid's overall viscosity.

3.5 Calculation of Field Quantities

3.5.1 Temperature Calculation

In DPD simulations, the temperature is set and held constant by the thermostat. It serves as an indictor of the accuracy of the solution of the equations of motion, as well as of the stability of the simulation as a whole. At equilibrium, the temperature is given by the total kinetic energy of the DPD particles,

$$T = \frac{1}{N} \sum_{i=1}^{N} \left(\mathbf{p}_i \cdot \mathbf{p}_i \right) / d \tag{3.44}$$

where $\mathbf{p}_i = m_i \mathbf{v}_i$ is the momentum of particle i, and d is the number of spatial dimensions. We note that for the simulations described here, the mass $m_i = m$ is the same for all particles, and mass in the system is scaled by m, so the temperature is actually measured as

$$T = \frac{1}{N} \sum_{i=1}^{N} \left(\mathbf{v}_i \cdot \mathbf{v}_i \right) / d \tag{3.45}$$

When a flow field is present, both a peculiar and a laboratory velocity can be measured. The temperature is calculated using the peculiar velocity, so that the bulk flow of the system does not add to the temperature. All of the simulations described in this work are of homogeneous domains, so we expect the temperature to be independent of spatial position. The temperature of a subregion of the domain can also be checked using Eq. 3.45. Checking to ensure that the temperature does not vary spatially is a good way to confirm that the flow is in fact homogeneous.

3.5.2 Calculation of Stress

We measure the overall stress state of the DPD system by adding up the contributions from all pairwise forces, as well as the kinetic contributions due to the velocity of the DPD particles themselves. In a domain of simple particles with periodic boundaries, where we have a reasonable expectation that the stress is homogeneous, this calculation is straightforward, given by the Irving-Kirkwood expression

$$\boldsymbol{\sigma}_{\alpha\beta} = -\frac{1}{V}\left\langle \sum_{i=1}^{N} v_{i\alpha} v_{i\beta} + \sum_{i=1}^{N}\sum_{j>i}^{N} r_{ij\alpha} F_{ij\beta} \right\rangle \tag{3.46}$$

where the first term accounts for the kinetic contributions due to particles transferring momentum by moving , and the second term represents all momentum transfers due to forces acting between particle pairs. This equation gives an averaged stress for the entire domian. It is perhaps worthwhile to expand Eq. 3.46 to include explicitly the action of the Lowe-Anderson thermostat with the impulsive actions of the thermostat presented in the form of a force:

$$\boldsymbol{\sigma}_{\alpha\beta} = -\frac{1}{V}\left\langle \sum_{i=1}^{N} v_{i\alpha} v_{i\beta} + \sum_{i=1}^{N}\sum_{j>i}^{N} r_{ij\alpha} F^{C}_{ij\beta} + \sum_{i=1}^{N}\sum_{j>i}^{N} r_{ij\alpha} \frac{\Delta_{ij\beta}}{\Delta t} \right\rangle. \tag{3.47}$$

In this expanded form, the second term refers only to the conservative force, while the third term includes the action of the LA thermostat, expressed as a force.

Polymer Contribution to Stress

When there are polymer molecules present, another term must be added to the stress equation to take into account the forces imposed on the fluid by the polymer springs. This contribution is calculated using the Kramers expression from kinetic theory:

$$\tau_{p\alpha\beta} = -n \left\langle \sum_{i=1}^{M} Q_{i\alpha} F^s_{i\beta} \right\rangle + n k_B T \delta_{\alpha\beta} \tag{3.48}$$

where $Q_{i\alpha}$ is the projection of the spring vector Q in the α direction, $F^s_{i\beta}$ is the projection of the force exerted by spring i in the β direction, and δ is the unit tensor. M is the total number of springs in the simulation. Adding the first term of the Kramers expression to Eq. 3.47 yields a complete expression for calculating the total stress tensor of a LA-DPD simulation which includes polymer molecules:

$$\boldsymbol{\sigma}_{\alpha\beta} = -\frac{1}{V} \left\langle \sum_{i=1}^{N} v_{i\alpha} v_{i\beta} + \sum_{i=1}^{N} \sum_{j>i}^{N} r_{ij\alpha} F^C_{ij\beta} + \sum_{i=1}^{N} \sum_{j>i}^{N} r_{ij\alpha} \frac{\Delta_{ij\beta}}{\Delta t} + \sum_{i=1}^{M} Q_{i\alpha} F^s_{i\beta} \right\rangle \tag{3.49}$$

Chapter 4

Modeling FENE Dumbbells with DPD

4.1 Introduction

In order to demonstrate the utility of DPD for studying the rheology of complex fluids, we wish to identify a simple test case with well established results that can be compared directly to the results produced by DPD. We have chosen for this role simple shear and planar elongation flow of a dilute solution of Finitely Extensible Nonlinear Elastic (FENE) dumbbells. FENE dumbbells are widely used as a polymer model because they are among the simplest kinetic theory models that can reproduce shear thinning. They represent a step up in complexity from Hookean dumbbells, which predict a constant viscosity at all shear rates.

4.2 Dumbbell Model

In bead-spring models, the entropic elasticity of sections of a polymer molecule are represented by massless springs connecting beads. The hydrodynamic force of the surrounding

fluid is applied to the molecule only at the beads. The entire mass of the molecule is concentrated in the beads as well. The simplest bead-spring model is the dumbbell, consisting of two beads with positions $\mathbf{r}_i$ and $\mathbf{r}_{i+1}$ connected by the spring vector $\mathbf{Q}_i$. In effect we are representing the entire length of the polymer molecule as a single segment. Naturally, such a simple model cannot fully reproduce the complex dynamics of a polymer molecule undergoing flow. The simplest elastic dumbbell is defined by the Hookean force law

$$\mathbf{F}(\mathbf{Q}) = H\mathbf{Q} \ , \tag{4.1}$$

which is useful for describing the behavior of polymers with small extension. This model holds very serious drawbacks for use in an explicit simulation such as DPD. Because the force is simply proportional to the distance between the two end beads, there is nothing in the Hookean force law to limit the ultimate length of the dumbbell. We are concerned with simulating molecules in a domain of limited size, so the choice of a Hookean dumbbell as a polymer model would require either a serious restriction in the strain rates that could be simulated, or else a very large domain would be called for lest the dumbbells extend to lengths greater than the simulation domain. Additionally, Hookean dumbbells are unable to reproduce nonlinear viscosity behavior in shear and elongational flows. For these reasons, we look to a slightly more detailed force law, the Finitely Extensible Nonlinear Elastic (FENE) model.

Flory[31] showed that as a polymer molecule is extended significantly, the entropic force becomes nonlinear. The force required to hold the ends of a chain at a specified separation is given by the inverse Langevin function. Warner has suggested an approximation to this function which is more easily computed. His model is known as the FENE force law, and is given by

$$\mathbf{F}(\mathbf{Q}) = \frac{H\mathbf{Q}}{\left(1 - \frac{Q^2}{Q_0^2}\right)} \tag{4.2}$$

where Q_0 is the maximum extension of the dumbbell. Physically, Q_0 is the contour length of the polymer. At small extensions, the spring force is linear, and quite similar

to the Hookean force law. As the molecule approaches it's maximum extension, the force diverges. Two different time constants can be written for FENE dumbbells. The Hookean time constant, which is the same as that of a Hookean dumbbell, is

$$\lambda_H = \frac{\zeta}{4H} \tag{4.3}$$

where ζ is the drag coefficient of a bead relative to the surrounding fluid. A second time constant is that of a rigid dumbbell.

$$\lambda_Q = \frac{\zeta Q_0^2}{12kT}. \tag{4.4}$$

The ratio of these two time constants give us b, a measure of the extensibility of the FENE dumbbell.

$$b = \frac{3\lambda_Q}{\lambda_H} = \frac{HQ_0^2}{kT} \tag{4.5}$$

When b is very large, the FENE spring resembles a Hookean spring.

The nonlinearity of the FENE spring force law makes writing an analytical constitutive equation impossible without resorting to a closure approximation, but Bird *et al.*[8] have calculated a series expansion approximation in powers of the velocity gradient $\dot{\gamma}$ for η and Ψ_1 for FENE dumbbells in dilute solution. This expansion is correct for small rates of extension. The first two terms are reproduced below.

$$\frac{\eta - \eta_s}{nkT\lambda_H} = \frac{b}{b+5}\left[1 - \frac{2b^2(4b+17)}{(b+5)(b+7)(b+9)(2b+7)}\left(\lambda_H\dot{\gamma}\right)^2 + \cdots\right] \tag{4.6}$$

$$\frac{\Psi_1}{nkT\lambda_H^2} = \frac{2b^2}{(b+5)(b+7)}\left[1 - \frac{2b^2(20b3 + 315b2 + 1578b + 2569)}{(b+5)(b+7)(b+9)(b+11)(2b+7)^2}\left(\lambda_H\dot{\gamma}\right)^2 + \cdots\right] \tag{4.7}$$

where η_s is the contribution to the viscosity from the solvent, and n is the number density of dumbbells. We note that these relations indicate that the scaled material functions for dilute FENE dumbbell solutions are dependent only on b, the extensibility parameter.

The equilibrium size for FENE dumbbells is

$$\frac{\langle Q^2 \rangle}{Q_0^2} = \frac{3}{b+5} \tag{4.8}$$

Because no closed constitutive equation is available, the behavior of the stress tensor, (and by extension, the material functions) at larger strain rates is only accessible through stochastic simulation techniques such as Brownian dynamics (BD) or in our case, DPD. Brownian dynamics is particularly well-suited to the problem of measuring the material function and spring extension behavior of dilute FENE dumbbells undergoing flow. In dilute BD calculations, the solvent is treated as a Newtonian continuum which interacts with the explicitly modeled polymer molecule via the hydrodynamic drag on the end beads, along with a random Brownian force on each bead that represents thermal motion. As we are interested primarily in homogeneous velocity fields here, there is no need to define a physical domain in BD. Rather, the orientation and length of the connector vector $\mathbf{Q}$ is updated at every time step without reference to the absolute location of the molecule in space. Herrchen and Ottinger[39] give the following stochastic differential equation which governs the evolution of the FENE dumbbell in time,

$$d\widehat{\mathbf{Q}} = \left(\widehat{\boldsymbol{\kappa}} \cdot \widehat{\mathbf{Q}} - \frac{1}{2} \frac{1}{1 - \widehat{Q}^2/b} \widehat{\mathbf{Q}} \right) d\widehat{t} + d\mathbf{W}(\widehat{t}) \tag{4.9}$$

where units of length are given by $(k_B T/H)^{\frac{1}{2}}$, and units of time, by $\lambda_H = \frac{\zeta}{4H}$. These result in the following dimensionless quantities:

$$\widehat{\mathbf{Q}} = \mathbf{Q}/\left(k_B T/H\right)^{\frac{1}{2}}, \quad \widehat{t} = t/\lambda_H, \quad \widehat{\boldsymbol{\kappa}} = \boldsymbol{\kappa}/\,\lambda_H\,. \tag{4.10}$$

We note that $\widehat{Q}_0^2 = b$. $W(t)$ is a three-dimensional Weiner process. Eq. 4.9 is integrated numerically over a long time and for a large ensemble of dumbbells. The dimensionless

polymer stress tensor is given by the Kramers form of the stress tensor,

$$\frac{\boldsymbol{\tau}_p}{nk_BT} = -\left\langle \frac{\widehat{\mathbf{Q}}\widehat{\mathbf{Q}}}{1-\widehat{\mathbf{Q}}^2/b} \right\rangle + \boldsymbol{\delta} \tag{4.11}$$

which leads to dimensionless material functions

$$\frac{\eta(\dot{\gamma}) - \eta_s}{nkT\lambda_H} = -\frac{1}{\lambda_H\dot{\gamma}}\frac{\tau_{p,xy}}{nk_BT} \tag{4.12}$$

and

$$\frac{\Psi_1(\dot{\gamma})}{nkT\lambda_H^2} = -\frac{1}{(\dot{\gamma}\lambda_H)^2}\frac{\tau_{p,xx}-\tau_{p,yy}}{nk_BT}. \tag{4.13}$$

We expect that the material functions calculated from a Brownian dynamics simulation will match those predicted Eqs. 4.6 and 4.7 for small values of $\dot{\gamma}\lambda_H$. Fan[24] was the first to publish comprehensive shear thinning results for Brownian dynamics simulations of dilute FENE dumbbell solutions. Figure 4-1 shows his results, Bird *et al.*'s expansion results, and the results of BD simulations I have run to demonstrate that BD simulations can serve as a reliable benchmark against which DPD simulation results can be compared.

In order to characterize a dilute FENE dumbbell solution using Brownian dynamics, only one quantity, is required. This is b, the extensibility parameter. All other model parameters are contained within the scaling units. This means that once the modeler has chosen b, the BD results that can be expected are fully specified.

We seek to make a direct comparison between the results of a dilute solution of FENE dumbbells simulated by Brownian dynamics, for which the process is straightforward and the results well known, and DPD, for which such results have never been reported. Toward this purpose, we will match the conditions of the DPD simulation as closely as possible to the BD case. We note that we have chosen to use BD without hydrodynamic interaction or excluded volume potential, despite the fact that we expect to see these effects to some degree in the DPD results. We have made this choice specifically because we want a "clean" benchmark, against which the effects of DPD's HI and EV will be

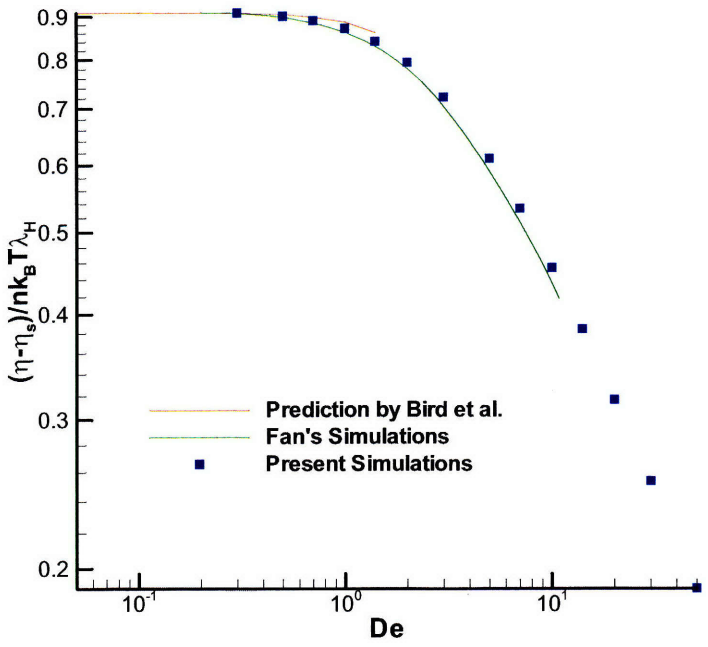

Figure 4-1: Comparison of the polymer contribution to the viscosity for FENE dumbbells from Bird *et al.*[8], Fan[24], and the present simulations.

easier to identify.

4.2.1 Polymers in DPD

Polymer molecules are created in DPD by connecting simple DPD solvent particles with entropic springs. The interactions between these polymer beads and other solvent beads in the simulation are not affected by the change. Rather, an additional spring force is applied to those particles which are part of a polymer molecule. Thus for the Lowe-Anderson thermostat formulation of DPD, which will be used for all of the following polymer simulations, the total force on particle i is given by

$$\mathbf{F}_i = \sum_{j \neq i} \left[\mathbf{F}_{ij}^C \left(\mathbf{r}_{ij} \right) + \mathbf{F}_{ij}^{LA} \left(\mathbf{r}_{ij}, \mathbf{v}_{ij} \right) \right] + \mathbf{F}_k^S \left(\mathbf{Q}_k \right). \tag{4.14}$$

One of the central differences between DPD and BD simulations of polymers are that the length and time scales inherent to the dumbbell, $(k_B T/H)^{\frac{1}{2}}$ and the Hookean time constant, $\lambda_H = \frac{\zeta}{4H}$, are not the only length and time scales present in DPD. The simple DPD fluid that makes up the solvent has its own characteristic length and time scales. Let us consider length scale first.

4.2.2 Length Scales for DPD Polymers

Lengths in DPD simulations are scaled by the particle interaction radius, r_c. Thus by specifying H, for the DPD FENE springs, we establish a relationship between the scales, r_c and $(k_B T/H)^{\frac{1}{2}}$. Once H has been chosen, we must still make an independent choice of b in order to establish the scaled (in terms of r_c) value of Q_0. While only one parameter, b, must be chosen to fully specify the BD problem, two are required for DPD. The choice of H can be interpreted as controlling the size of the solvent DPD molecules relative to the length of the spring, as illustrated in Figure 4-2. When, for a constant choice of b, H is larger and Q_0 is smaller, the DPD interaction range r_c is larger in relation

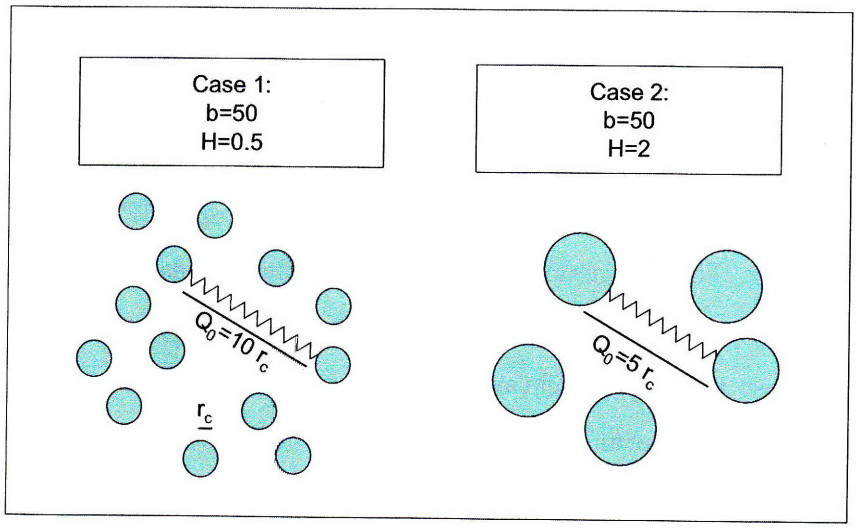

Figure 4-2: Illustration of the length scaling implications of the maximum dumbbell extension, Q_0.

to the BD length scale than in the case when H is small and Q_0 is larger. Thus, we adopt the point of view that a choice of smaller Q_0 for the DPD system represents a much more coarse-grained representation of both the polymer and solvent. The solvent DPD particles each contain a larger number of solvent molecules. Similarly, the polymer beads in Case 2 of Fig. 4-2 are much larger than those in Case 1. There is no way for Brownian dynamics to resolve this difference, so we compare both cases to the Brownian dynamics standard so as to determine whether one formulation is more faithful than the other. This distinction is particularly important, as the vast majority of studies of DPD modeling polymer molecules are performed with very small maximum extensions, sometimes as little as $Q_0 = 0.86r_c$ [62]. Further discussion of DPD length scales can be found in [5, 11, 19, 22, 23].

4.2.3 Time Scales for DPD Polymers

The standard time scale used in DPD simulations results from setting the temperature, k_BT, to unity. Because the temperature is defined as the average kinetic energy of the DPD particles, a time scale is resultant so as to define the average particle velocity correctly. In order to properly scale the results of a DPD simulation for comparison to BD, we must relate the DPD time scale to λ_H, which is used as the BD time unit. Having previously chosen H, we must now determine the value of ζ, the drag coefficient. This is not a straightforward task, as there is no reliable analytical relationship available between DPD system parameters and ζ. Instead, ζ must be measured directly. It is worth pointing out that the drag coefficient is nearly a linear function of the solvent viscosity. Because we are using the Lowe-Anderson thermostat, we are able to manipulate the solvent viscosity, and by extension the drag coefficient by changing Γ, the thermostatting frequency. This allows us one lever in manipulating the ratio of the two time constants. Unfortunately, experience shows that predictive relationships between Γ and ζ are not sufficiently precise for our purposes.

4.2.4 Drag Coefficient

In the case of Brownian Dynamics simulations, the drag coefficient ζ is scaled by the relaxation time, and does not appear in the governing equations. Physically this parameter governs the drag the solvent fluid exerts on the beads. It, along with the spring constant H, determines the relaxation rate of the FENE dumbbell, and is related physically to the viscosity of the solvent. For DPD, the drag coefficient is not chosen directly, but rather must be measured by the modeler. It is dependent on the density as well as the thermostatting rate Γ. The most straightforward method of measuring the drag coefficient is to choose a single test DPD particle in a bath of DPD fluid at rest and apply a body force to it. The velocity of the test particle is then measured over a long period of time, and an average taken. The drag coefficient is simply defined as $\zeta = \frac{F_{applied}}{v_{particle}}$. Several precautions

must be taken when measuring the drag coefficient in this way. First, the negative of the body force applied to the test particle must be distributed to the rest of the particles in the fluid to ensure that total system momentum is conserved. If the body force of the test particle is given by F_b, every other particle in the simulation must experience a body force $\frac{-F_b}{N-1}$ where N is the total number of DPD particles. Additionally, it is important that the domain size be large enough so that box-size effects are unimportant. I have found that a $10 \times 10 \times 10$ cubic domain is sufficiently large for this purpose. The chief drawback to this method is that it is quite inefficient computationally. As we have chosen our DPD particle number density to be $\rho = 4$, a single test particle, from which we are able to draw one data point, requires a simulation of 4000 total DPD particles. Even averaging over $500,000$ timesteps, variations in the calculated drag coefficient from this method can be as high as $10 - 15\%$.

An alternate method of measuring the drag coefficient is available from kinetic theory. If we examine the Kramers and Giesekus forms of the stress tensor, given in Eq.4.15 and 4.16

$$\boldsymbol{\tau}_p = -n\langle \mathbf{F}^{(\mathbf{c})}\mathbf{Q}\rangle + nkT\boldsymbol{\delta} \tag{4.15}$$

$$\boldsymbol{\tau}_p = \frac{n\zeta}{4}\langle \mathbf{QQ}\rangle_{(1)} \tag{4.16}$$

we note that only one of the two expressions contains the drag coefficient. By setting the two expressions equal to each other, we can calculate ζ. Let us begin by examining the upper convected derivative of the the $\langle \mathbf{QQ}\rangle$ tensor. For simple shear flow, we find

$$\langle \mathbf{QQ}\rangle_{(1)} = \frac{\partial}{\partial t}\begin{pmatrix} \langle QQ\rangle_{xx} & \langle QQ\rangle_{xy} & 0 \\ \langle QQ\rangle_{xy} & \langle QQ\rangle_{yy} & 0 \\ 0 & 0 & \langle QQ\rangle_{zz} \end{pmatrix} - \begin{pmatrix} 2\langle QQ\rangle_{yx} & \langle QQ\rangle_{yy} & 0 \\ \langle QQ\rangle_{yy} & 0 & 0 \\ 0 & 0 & 0 \end{pmatrix}\dot{\gamma}_{xy} \tag{4.17}$$

As we are interested in simulating a steady state flow, the first term drops out, and

one can write an equation for ζ in terms of invariants of the $\langle QQ \rangle$ and $\langle F^{(c)}Q \rangle$, tensors.

$$\zeta = \frac{-\langle F^{(c)}Q \rangle + kT}{\frac{1}{2}\langle QQ \rangle \dot{\gamma}_{xy}} \tag{4.18}$$

Figure 4-3 shows ζ calculated from Eq. 4.18 for long dumbbells with $Q_0 = 20$ under shear flow. We show results for two values of the Lowe-Anderson parameter Γ, which represent high and low viscosity solvents. We immediately note two problems. First,

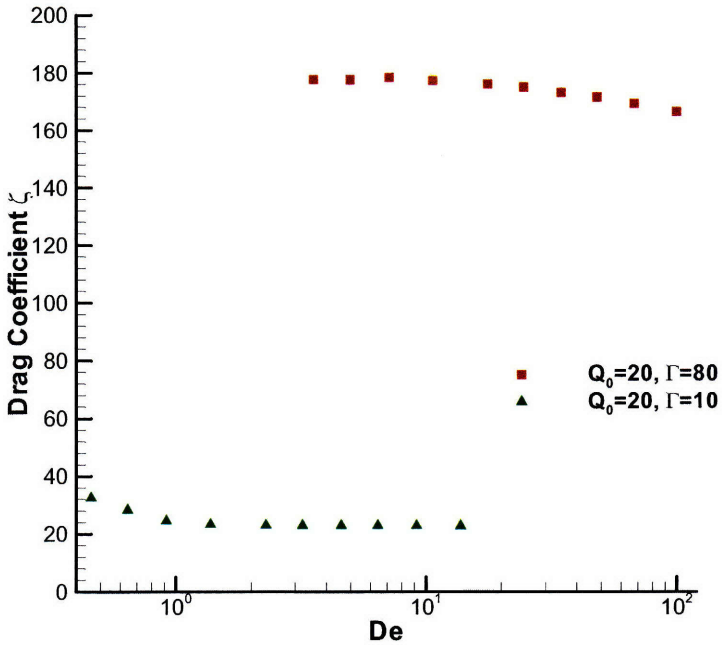

Figure 4-3: Drag coefficient measured with Eq. 4.18 for $Q_0 = 20$ dumbbells at two values of Γ.

at low De, there is a sharp increase in the measured drag coefficient. This is a result of the excluded volume potential described above, which is present even for such a long dumbbell. This means that at low strain rates a significant population of dumbbells have an extension less than r_c, and thus experience an additional repulsive force which is not

anticipated in Eq. 4.18. At very large values of De, which are sampled in the higher viscosity solvent case, we note that ζ decreases slightly with increasing strain rate. This suggests to us that the assumption upon which the Giesekus expression of the stress tensor is based, namely that ζ is a constant, may not be reliable in the case of DPD. In both cases, however, an estimate of ζ can be made in order to properly scale the rheological results.

4.2.5 Hydrodynamic Interaction

In the BD simulations described above, there is no hydrodynamic interaction included in the model. In other words, the motion of one bead through the solvent is assumed not to disrupt the solvent's velocity field, and thus has no effect on the hydrodynamic drag felt by any other polymer beads. There is no reason to expect that this holds true for DPD, as the motion of the explicit solvent DPD molecules are affected by the motion of the polymer beads through them. Unfortunately, there is no a priori method of measuring the effect of the hydrodynamic interaction on DPD polymers. It is reasonable to expect, however, that the larger the interaction range of the DPD particles is in relation to the maximum spring extension, the greater the effect of the hydrodynamic interaction will be.

4.2.6 Excluded Volume

Because all DPD particles, whether polymer or solvent, are governed by the same set of forces, the two end beads of a polymer dumbbell will experience a repulsion force if the spring extension distance $Q(t)$ is less than the particle interaction radius r_c. In trying to compare DPD dumbbells to Brownian dynamics models, it is not clear how to characterized this interaction. On one hand, it is reasonable to view this force as an excluded volume interaction, as the two beads are prevented by the conservative repulsion force from occupying the same space. In BD simulations an excluded volume potential

is typically employed to control the solvent quality. In a good solvent, the polymer has a greater affinity for the solvent than for itself, which can be modeled as a repulsive force between polymer beads, as BD has no explicit solvent particles to control. In the BD simulations presented here there is no excluded volume interaction. On the other hand, there is no way to avoid the excluded volume potential in a DPD simulation. The coarse-grained nature of the DPD fluid means that a single particle is only interacting with a limited number of surrounding particles at any given time. The small number of neighbor particles increases the importance of each one for maintaining an isotropic pressure force on the bead in question. For this reason, it is not a good option to simply prevent beads on the same polymer molecule from repelling each other. When this is done, the pressure force from the surrounding solvent beads pushes the particles together, resulting in a shorter spring than is predicted by theory.

Figure 4-4 shows the equilibrium size of DPD FENE dumbbells with $b = 50$ as a function of the maximum extension Q_0, along with the theory prediction from Eq. 4.8. As one would expect, a shorter dumbbell is more likely to have a spring extension distance within the interaction range of its composite beads, and is thus subjected to the added repulsive force which is not anticipated in Eq. 4.8 . As a result, it will be more elongated relative to the predicted extension. We make the observation that dumbbells with a very short maximum extension are expected to have material functions that diverge more from the BD case than do those of longer dumbbells, especially in the zero-shear-rate range. This distinction is important, as the vast majority of previous work modeling polymers with DPD have chosen a maximum spring extension that will result is a significant bead repulsion interaction. It should be noted that the difficulty described here is not a hindrance to successfully modeling a physical polymer. Rather it is a problem when the object is to hew as closely as possible to the FENE dumbbell model.

4.2.7 Limitation on Strain Rate

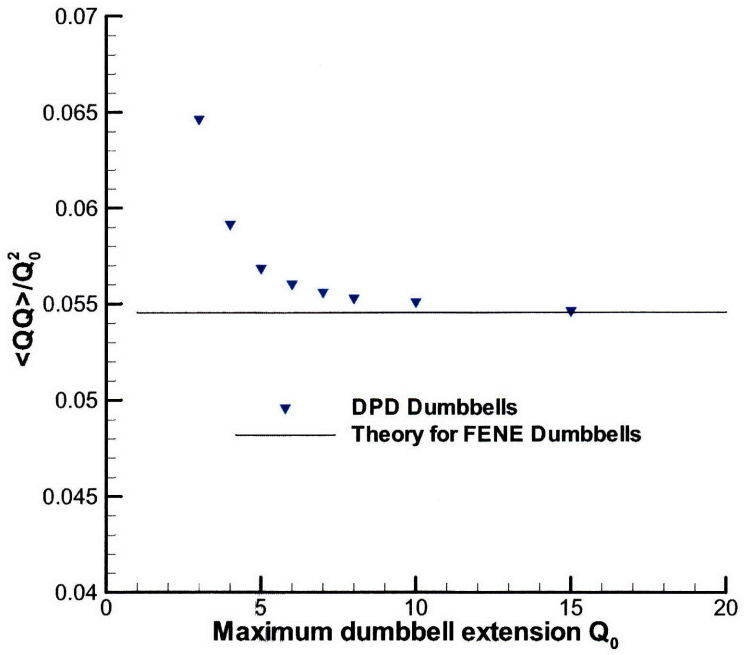

Figure 4-4: Mean squared equilibrium length of dumbbells as a function of the maximum extension length, Q_0; the smaller the dumbbell, the greater the deviation from the length predicted by theory.

As noted in Chapter 2, the viscosity of the DPD fluid with the Lowe-Anderson thermostat is variable, based on the choice of Γ, the thermostatting rate. As Γ is increased, the fluid viscosity increases, resulting in an increase in ζ, and consequently an increase in λ_H. As illustrated in Figure 4-5, the transition for FENE dumbbells from the zero-shear rate regime to the shear-thinning regime takes place over the range $0.1 < \mathrm{De} < 100$, so this is also the range of De that must be accessed using DPD. The range of shear rate values for which DPD simulations are practical are limited on both the high and low ends. At shear rates above 0.3 the viscosity of the simple DPD fluid begins to drop, suggesting that the system is no longer reliably behaving like a fluid. This is illustrated for two values of the Schmidt number in Figure 4-5. It appears that the shear-thinning effect begins at roughly the same absolute DPD shear rate without regard to the value of Γ. We note that the same behavior is observed in a DPD fluid that employs the original DPD thermostat. This would indicate that the limiting shear rate is a function of the conservative potential. At low shear rates, the computational costs become untenable, as the polymer stress becomes small in relation to the stochastic error. In this situation, either large ensembles or very long simulation times are required to recover data with acceptable levels of error. Bound by these constraints, it would be most useful to be able to effectively control the relaxation time of our molecules so as to more easily access the large range of De in which we are interested. In order to do so, however, we must first convince ourselves that changing Γ, and by extension changing Sc in the fluid does not affect the polymer dynamics in any meaningful way. We will demonstrate this by showing agreement between the material function behavior of solutions of DPD dumbbells which differ only in the viscosity of the solvent, as controlled by Γ.

4.2.8 Constraints on the Range of De to be Simulated

It is important that the modeler choose the parameters at his disposal, Γ and H, such that the interesting range of De coincides with the accessible range of shear rates, remembering

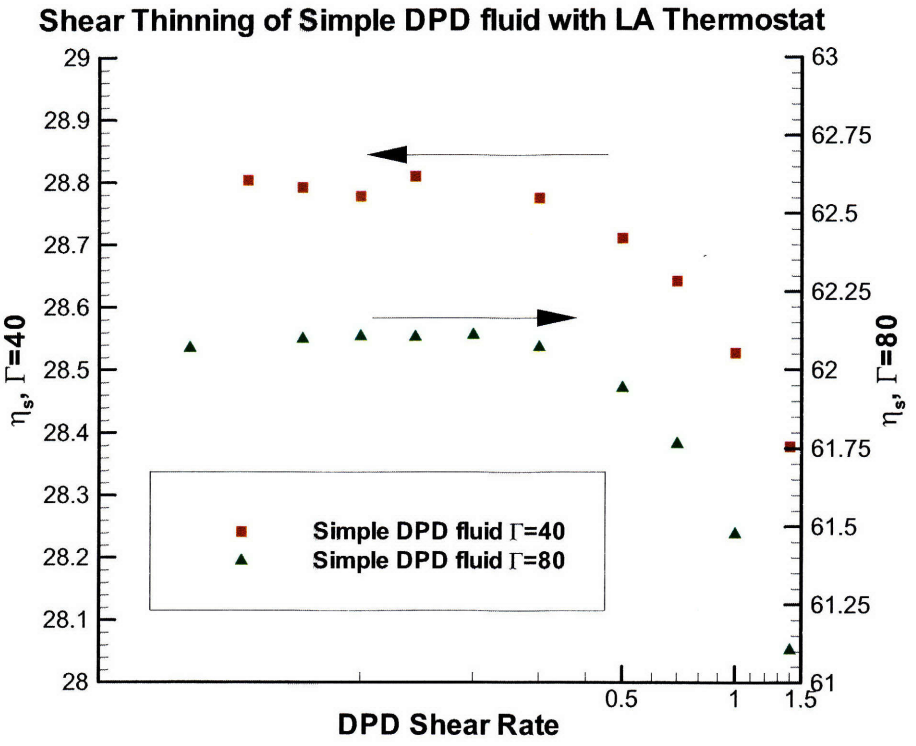

Figure 4-5: At a shear rate greater than 0.3, the simple DPD fluid (no dumbbells) begins to show shear-thinning behavior, indicating that the rate of strain is greater than the relaxation time of the simple DPD particles. The onset of shear-thinning is independent of the viscosity of the simple fluid.

that the shear rate is scaled by the Hookean time constant, $\lambda_H = \frac{\zeta}{4H}$. For the purposes of the comparison at hand, we have chosen the FENE parameter b to a value of 50. This represents a middling degree of extensibility, approximating neither a Hookean dumbbell, nor a rigid rod. The extensibility parameter $b = \frac{HQ_0}{4k_BT}$ leads to a relation between Q_0 and H so that choosing one specifies the other. Thus by choosing a longer dumbbell, H is reduced and λ_H increases. Within the range of accessible DPD shear rates, a longer dumbbell will thus be able to access a larger value of De. The simulation domain must be twice the maximum extensibility in the flow direction, and a multiple of that in the other two dimensions. It is thus advisable to set a reasonable upper limit of the maximum extension of the model dumbbell. In practice, I have not attempted any simulations of dumbbells with Q_0 greater than 20. Any further tuning of the time constant must be accomplished by changing ζ, which we access through Γ. Once again, we find that there are practical limits to increasing the time constant. Because $\Gamma\Delta t$ is defined as the likelihood that a particle pair will be thermalized at each timestep, the product of the two quantities has an upper limit of unity. Thus, significant increases in Γ must be accompanied by a reduction in the time step, imposing a significant computational cost. For $b = 50$ we are able to access the interesting range of shear rates within these constraints.

4.2.9 Dilution Approximation

In a Brownian dynamics context, the default assumption is dilution, because the solvent costs nothing to represent. It exists solely in the form of forces applied to the polymer beads. Each member of the ensemble is treated individually, and simulated for the allotted time in isolation. There is no need to establish a physical domain with boundaries. Rather, the center of mass of the dumbbell is always found at the origin, and the relative positions of the end beads are kept track of. Thus dilution represents the most efficient manner of simulation for BD. This is not the case for DPD, as we are beginning with an arrangement modeled on molecular dynamics which involves a physical domain filled with

particles, all of which must be simulated explicitly. As such, it is infeasible to simulate a single dumbbell in isolation, unless one has an infinite supply of computer time. The overhead costs associated with the simulation of all the accompanying solvent particles is too great. Rather, a more concentrated solution of polymer molecules is simulated under conditions that largely prevent individual polymer molecules from perceiving each other's presence. Two conditions are required for this assumption to hold. First, the DPD particles that make up both solvent and polymer must have identical interactions. In other words, a polymer DPD bead that encounters another bead must experience the same interaction regardless of the species of the 2nd bead. This condition can also be interpreted as requiring the solvent be a θ-solvent. The second condition is that of phantom springs, in which the FENE springs exist as a force between two beads, but do not otherwise interact with the rest of the domain. Thus, springs are free to pass through each other. Under these conditions, a DPD particle that is part of a dumbbell will interact with another polymer DPD particle with rules that are identical to an interaction with a solvent molecule. The conservative force interaction will be the same, and the LA thermostat interaction will be indistinguishable provided that the velocity distribution of solvent DPD particles does not differ too greatly from that of polymer particles. In this way we will simulate solutions of DPD dumbbells that function as though they were dilute, despite having considerable concentrations of dumbbells. This principle is illustrated in Fig. 4-6 which shows a linear dependence of solution viscosity to dumbbell concentration for solutions of dumbbells with $Q_0 = 8$ and $H = 0.78125$. The dumbbells were simulated undergoing simple shear flow at $\mathrm{De} = 0.56$ and 2.8, which represent the zero-shear viscosity region and the shear-thinning region. We have chosen 25% polymer as our standard, as this represents a compromise between minimizing the computational cost required to produce viscometric data, and a desire to avoid significant concentration effects.

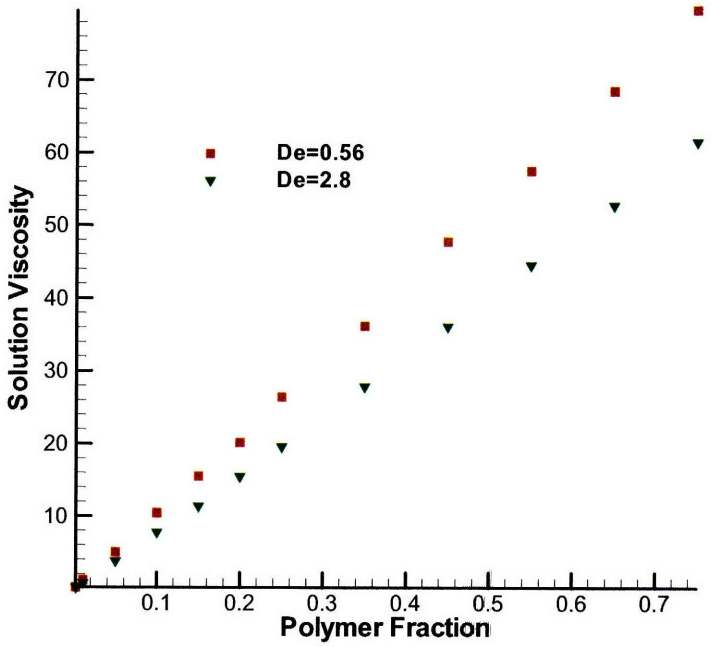

Figure 4-6: Viscosity dependence on polymer fraction for DPD dumbbells. The linear dependence of viscosity confirms that an approximation of dilution is reasonable for DPD dumbbells with phantom springs.

4.3 Results and Discussion

4.3.1 Shear Flow

The simulation results presented in this section represent the first attempt to compare the quantitative rheological results of simulations making use of the DPD model to the results produced by a more extensively studied method. We have chosen Brownian Dynamics simulations of dilute polymer dumbbells as the standard to which we will compare our DPD results. In all cases, the DPD simulations have been performed using the Lowe-Anderson thermostat. The domain is periodic in three dimensions, utilizing the Lees-Edwards boundary conditions to implement shear flow[1]. The SSLOD equations of nonequilibrium molecular dynamics are used to impose the flow profile throughout the fluid[21]. The number density of DPD particles is $\rho = 4$ for all simulations, with the temperature held constant at $k_BT = 1$. The temperature control from the LA thermostat is excellent, and no simulation shows a temperature error greater than 0.5%. In all cases the timestep is $\Delta t = 0.01$. Due to the limitations on the range of shear rates which are accessible to DPD, there is not perfect overlap between the ranges of De sampled for each dumbbell length. The range in De is expanded, however, by varying Γ. The values of Γ used range from 10 to 80, which corresponds to Schmidt numbers ranging from roughly 30 to 2000. Figure 4-7 shows the polymer contribution to the viscosity for the entire range of dumbbell solutions simulated with the DPD method. In all cases the FENE parameter $b = 50$, so all series can be thought of as representing the same physical molecule. For reference, the results of the dilute Brownian dynamics case is shown as a solid black line. We begin by noting that the longer DPD molecules as a rule hew more closely to the BD result across the entire spectrum of shear rates studied. We expect to see divergences from the BD case due to excluded volume and hydrodynamic interaction, both of which are likely to be more strongly expressed by a shorter, more coarse-grained DPD particle. In the zero-shear-rate regime, we note that the longest DPD particles show remarkable agreement with the BD result, while shorter particles

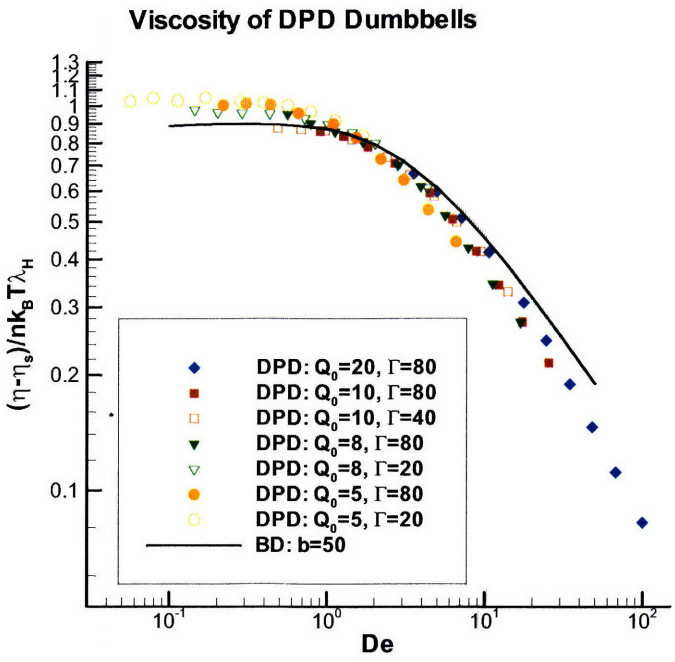

Figure 4-7: Polymer contribution to the viscosity for a range of DPD dumbbells along with the results for dilute Brownian dynamics. Results produced with high solvent viscosity are filled, while open symbols denote lower values of Γ.

overpredict the zero-shear-rate viscosity. This in consistent with our earlier observation that shorter DPD dumbbells are artificially extended at equilibrium as a result of the excluded volume interaction.

All DPD dumbbell models go through the transition from constant viscosity to the shear-thinning region at roughly the same De, in very close agreement with the BD results. This implies a faithful modeling of the fluid physics, and a quantitatively correct transition point at which the dumbbells begin to stretch and align with the flow. In the shear-thinning region, all DPD models overpredict the rate of shear thinning, resulting in a larger power law result than is predicted by the BD case. Once again, we note that the longest DPD dumbbells show the closest agreement with BD, which implies that the effect of hydrodynamic interaction is minimized for longer molecules, which correspond to a finer-grained DPD particle. All the DPD dumbbell solutions presented here were subjected to the same set of shear rates scaled in native DPD units. De is given as $\dot{\gamma}\lambda_H$, so the variation in De can be attributed to the differing values of H required to satisfy the condition that $b = 50$. Thus while we seek to compare the relative performance of DPD dumbbells constructed with differing maximum lengths, we note that each choice of Q_0 also affects the range of shear rates which can be accessed.

Figure 4-8 presents the first normal stress coefficient results for the entire suite of DPD dumbbell simulations alongside the BD result. The first normal stress coefficient results show significant qualitative similarities to the viscosity results reported above. We observe an overprediction of the zero-shear-rate first normal stress coefficient for the shorter dumbbells, while the longer dumbbells show remarkable fidelity to the BD prediction. The transition from zero-shear regime to the power law shear-thinning regime occurs at the correct De for all DPD dumbbells studied. In the shear-thinning regime, we note once again that the longest DPD dumbbells show the closest agreement with the BD results. The power-law slope is observed to be slightly more negative (faster shear-thinning behavior) as the dumbbell size is decreased. This observation further supports our contention that the hydrodynamic interaction, which we predict to have a

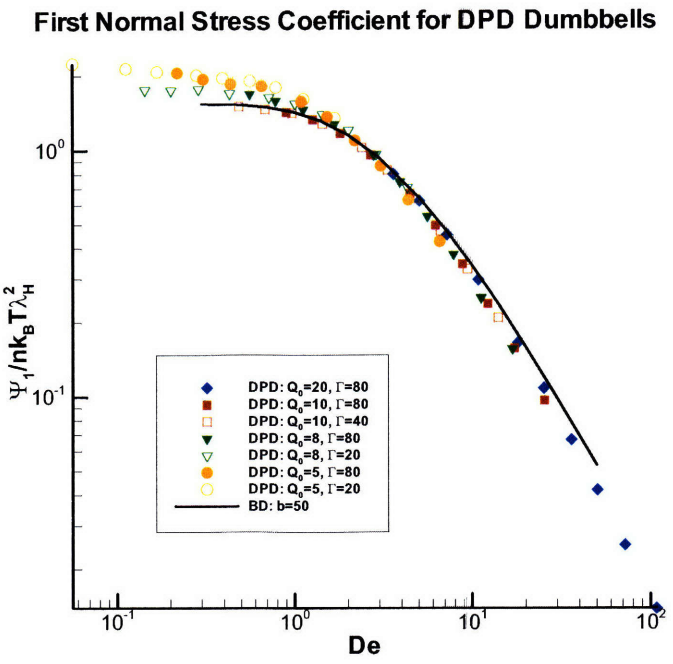

Figure 4-8: First normal stress coefficient for a range of DPD dumbbells along with the results for dilute Brownian dynamics.

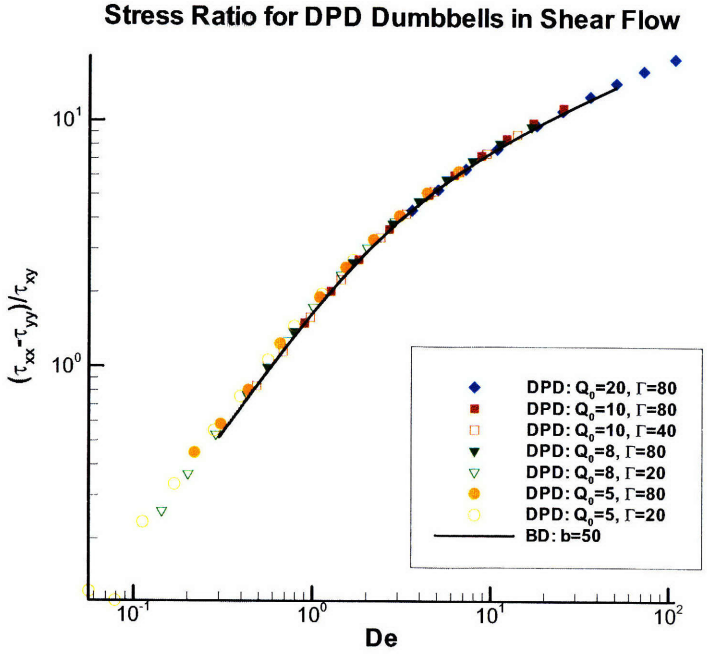

Figure 4-9: Stress ratio for a range of DPD dumbbells along with the results for dilute Brownian dynamics.

larger effect on shorter DPD dumbbells, is responsible for the greater degree of shear-thinning observed in DPD compared to the BD case. We note that the first normal stress coefficient results for DPD in the shear-thinning region adhere much more closely to the BD results than do the viscosity results for all dumbbell lengths. Figure 4-9 shows the stress ratio for each DPD dumbbell series along with the Brownian dynamics result. We note excellent agreement between the longer DPD dumbbells and the BD data, while we see that the shorter dumbbells show a slight overprediction at low De. Thus, while there is an overprediction in both the viscosity and the first normal stress coefficient, the normal stress difference is shown to be more important. This supports the contention that the low De differences between the DPD and BD results stem from the excluded volume interaction of the DPD beads.

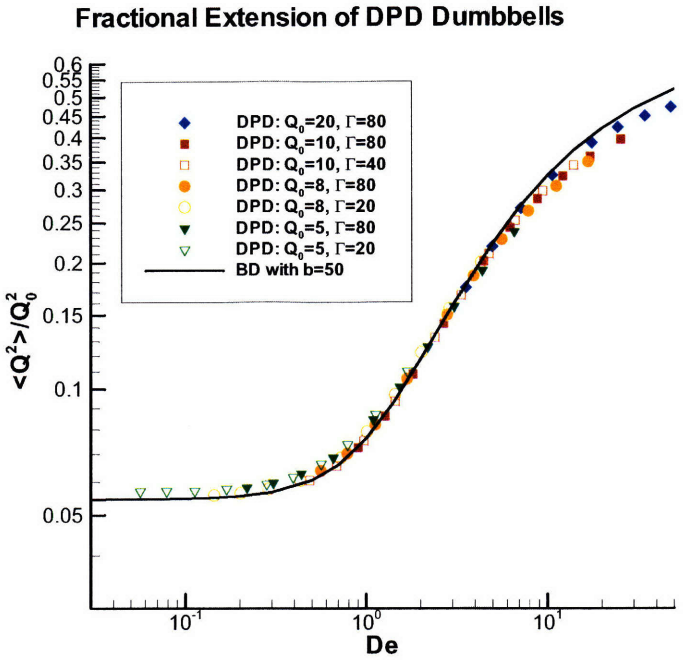

Figure 4-10: Fractional extension for a range of DPD dumbbells along with the results for dilute Brownian dynamics.

Figure 4-10 gives the mean squared fractional extension of the DPD dumbbells as a function of the Deborah number. We begin once again by noting the remarkable degree of agreement between the results from the two simulation methods. As one might expect, there is a slight overprediction of the dumbbell length at low De for the shortest dumbbells. Through the transition period, 1 <De< 10, all lengths of DPD dumbbell collapse atop the BD result. As the dumbbells elongate significantly, they reach the non-linear portion of the FENE force curve, and an inflection point appears in the fractional extension curve. Above this point, at roughly De= 10, the DPD dumbbells begin to show less extension than the BD case. The effect is more pronounced for shorter dumbbells than for longer ones. This result indicates that the faster shear-thinning of the viscosity noted earlier is a result of dumbbells undergoing less extension than in the BD case.

Schmidt Number Effects on Dumbbell Rheology

In the preceding results, the accessible range of strain rates was extended for each dumbbell length by simulating shear flows using varying values of the LA thermostat rate, Γ. In order to present results obtained at different Schmidt numbers as representing the same molecule, we must establish that the Schmidt number is unimportant in determining the rheological properties of the macromolecular model. The importance of the Schmidt number in determining the validity of DPD as a simulation method has been extensively debated[37, 79]. Figures 4-11 and 4-12 show the polymer contribution to the viscosity and the fractional extension results for the $Q_0 = 10$ DPD dumbbells alone. We note that

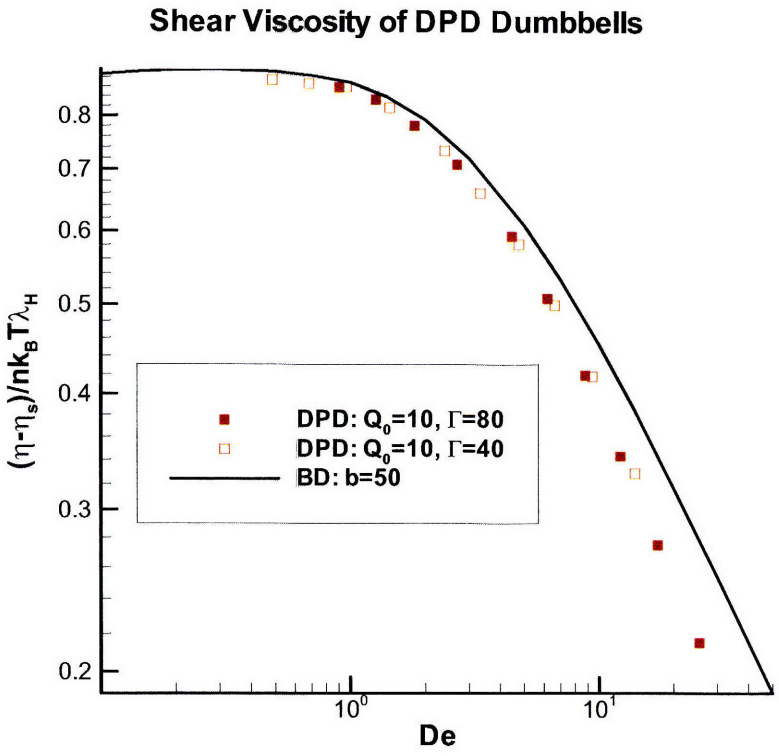

Figure 4-11: Viscosity of $Q_0 = 10$ dumbbells simulated at multiple values of Γ.

this is the same data presented in the earlier figures, isolated here for clarity. There is a

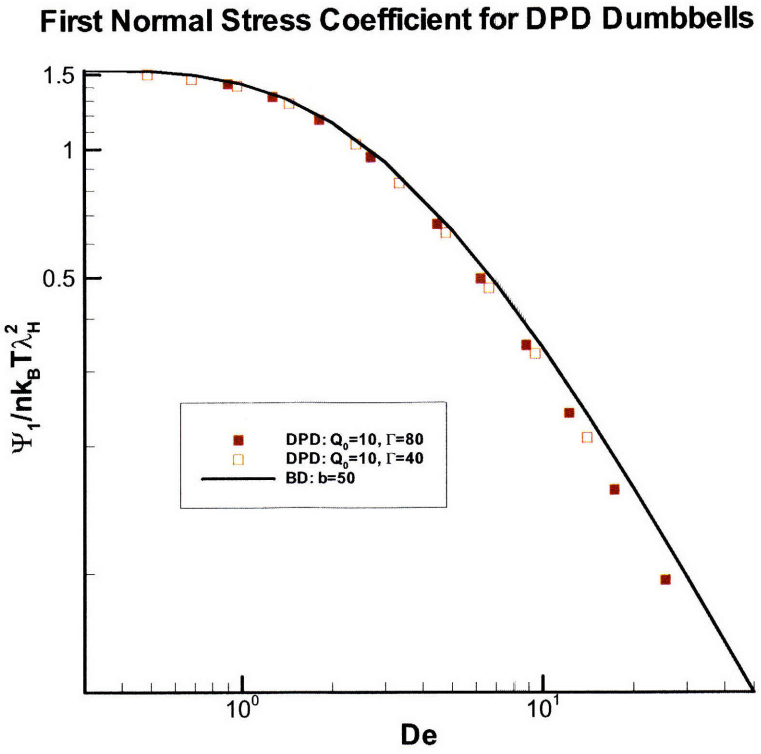

Figure 4-12: First normal stress coefficient of $Q_0 = 10$ dumbbells simulated at multiple values of Γ.

great deal of overlap in the shear rates simulated for $\Gamma = 80$ and $\Gamma = 40$, which allows us to compare the rheological results of the two series. Because the drag coefficient ζ changes with Γ, each series is scaled with its own relaxation time $\lambda_H = \zeta/4H$, but all other scalings between the two series are identical. The close agreement between the high and low Schmidt number simulations suggests that, outside of its effect on the time scaling, the Schmidt number is unimportant in determining the rheology of macromolecules simulated using DPD. Rather, we find that the sole importance of the Schmidt number is found in the fact that we are able to control the solvent viscosity by varying Γ.

4.3.2 Giesekus Anisotropic Drag Model

In using the Giesekus and Kramers forms of the stress tensor to calculate the drag coefficient as presented in Section 4.2.4, we noted that the calculated drag coefficient appears to decrease at large shear rates. This suggests that the assumption of a Maxwellian solvent velocity field, which is required in the development of the Giesekus form of the stress tensor, is not valid. It is clear that the solvent drag on polymer DPD beads cannot be satisfactorily explained with a single scalar drag coefficient. This is not an unexpected result, as we expect DPD to naturally exhibit hydrodynamic interaction. We look instead to an anisotropic friction tensor, $\boldsymbol{\zeta}$ that varies with the shear stress. Giesekus[35] has suggested Eq. 4.19 to calculate the friction factor

$$\boldsymbol{\zeta}^{-1} = \frac{1}{\zeta}(\boldsymbol{\delta} - \frac{a}{nkT}\boldsymbol{\tau}_p) \tag{4.19}$$

where a is a fitted parameter.

Sim *et al.*[74] have performed Brownian Dynamics simulations of dilute FENE dumbbells in shear flow that incorporate the Giesekus anisotropic friction tensor. Increasing the value of a has no effect on the zero-shear-rate viscosity, but results in faster shear-thinning behavior at high De. This behavior suggests that the drag coefficient in DPD

may follow this model, with larger values of a for smaller dumbbells.

Eq. 13.7-4 in Bird *et al.*[8] provides a starting point for making use of the relation in Eq. 4.19. We begin with the general equation for $\langle QQ \rangle_{(1)}$:

$$\frac{\langle \mathbf{QQ} \rangle_{(1)}}{2} = kT \left\langle \boldsymbol{\delta} : \left\{ \left(\frac{\partial}{\partial \mathbf{Q}} \boldsymbol{\zeta}^{-1} \right) \mathbf{Q} + \left[\left(\frac{\partial}{\partial \mathbf{Q}} \boldsymbol{\zeta}^{-1} \right) \mathbf{Q} \right]^{\dagger} \right\} \right\rangle - 2kT \left\langle \boldsymbol{\zeta}^{-1} \right\rangle - \left\langle \left\{ \boldsymbol{\zeta}^{-1} \cdot \mathbf{F}^{(c)} \mathbf{Q} \right\} + \left\{ \mathbf{Q} \mathbf{F}^{(c)} \cdot \boldsymbol{\zeta}^{-1} \right\} \right\rangle \quad (4.20)$$

Because $\boldsymbol{\zeta}^{-1}$, $\langle \mathbf{QQ} \rangle$, and $\langle \mathbf{F}^{(c)} \mathbf{Q} \rangle$ are all symmetric, substituting Eq. 4.19 into Eq. 4.20 results in an expression for $\langle \mathbf{QQ} \rangle_{(1)}$ dependent only on quantities that can be measured in a DPD simulation, and a.

$$\frac{n\zeta}{4} \langle \mathbf{QQ} \rangle_{(1)} = \boldsymbol{\tau}_p - a\boldsymbol{\tau}_p + \frac{a}{kT} \boldsymbol{\tau}_p \cdot \left\langle \mathbf{F}^{(c)} \mathbf{Q} \right\rangle \quad (4.21)$$

In the limit $a \to 0$, Eq. 4.21 reduces to the Giesekus expression for the stress tensor in the absence of hydrodynamic interaction.

We can now write an equation for a in terms of the traces of the tensors in Eq. 4.21.

$$a = \frac{\frac{n\zeta}{4} \langle QQ \rangle_{(1)} - \tau_p}{\frac{\tau_p}{kT} \cdot \langle F^{(c)} Q \rangle - \tau_p} \quad (4.22)$$

Thus by calculating a for each simulation, we can test whether the anisotropic drag model captures the observed shear-thinning behavior of the DPD dumbbells. Figure 4-13 gives the calculated value of a for the two longest dumbbells simulated with DPD. The very large values of a at low Deborah numbers are an artifact of the excluded volume potential. We can see, however, that at large molecular extension, a constant value of a is approached, and that it is smaller for the longer dumbbell. This is consistent with the predictions of Sim *et al.*[74], who predict faster shear-thinning as a is increased. The calculated values of a for shorter dumbbells are too affected by the excluded volume

interaction to yield comprehensible results. We nonetheless conclude that an anisotropic drag tensor model is useful in describing the progressively faster shear thinning that occurs at high De for shorter DPD dumbbells.

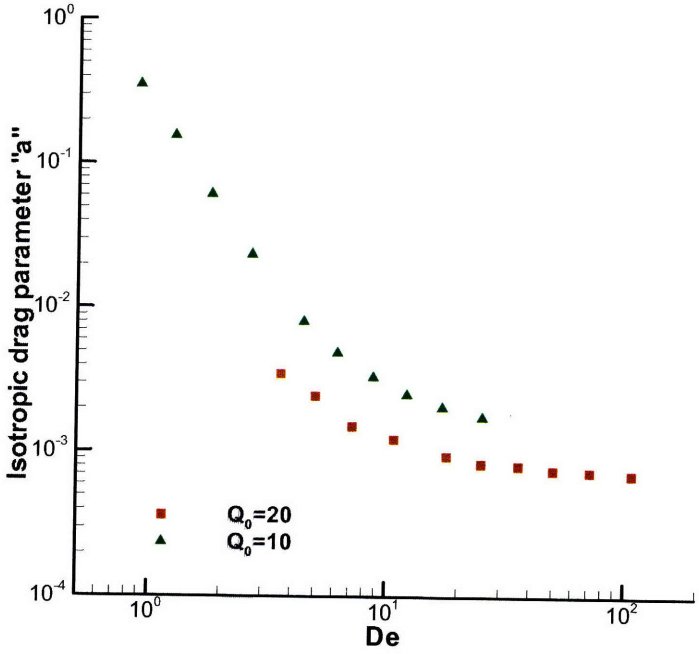

Figure 4-13: Calculated value of the Giesekus anisotropic drag parameter a. The value of a is strongly distorted by the influence of the excluded volume potential.

4.3.3 Planar Elongational Flow

The results presented here represent the first implementation of Kraynik and Reinelt's boundary conditions, and by extension planar elongational flow, using the DPD simulation technique. As such, these results serve to demonstrate the viability of the DPD method itself for modeling planar elongational flows. This is in addition to our goal of establishing the utility of DPD for rheological characterization of macromolecules. Like

the steady state shear flow experiments presented previously, all simulations are run with DPD number density $\rho = 4$, at temperature $k_B T = 1$, and with the flow field enforced by the SSLOD equations. In all cases $b = 50$.

In steady shear flow, the range of De over which a dumbbell elongates is quite large, so that a wide range of shear rates must be applied in order to examine the rheological response from the zero-shear region to the fully elongated, shear thinning region. In the case of planar elongational flows, several advantages emerge for the DPD modeler. First, elongational flow involves much stronger deformation of the fluid. This means that the interesting dynamics (particularly the extension of the polymer dumbbells) occurs as a much lower rate of strain. Because DPD is limited in the strain rates which are accessible to it, this is a significant advantage. Second, the interesting dynamics occur over a narrower band of De, which once again works to the advantage of DPD. As a result of this, we have been able to access the entire range of interesting strain rates using a single value of Γ for each DPD dumbbell model. Finally, as the deformation of the dumbbells is greater in a planar elongational flow, the stress response is also larger, which reduces the relative importance of stochastic error. As a result, the need for very long averaging periods is reduced.

Elongational Viscosity

Figure 4-14 shows the elongational viscosity of DPD dumbbells undergoing steady planar elongation. The $Q_0 = 20$ dumbbells show very close agreement with the results of the BD simulations throughout the range of De studied. As was observed in the shear flow results, a reduction in the length of the dumbbells relative to the DPD interaction length once again results in an overprediction of the viscosity at low De, and an underprediction as the molecules are stretched significantly. Here we note that both effects can be observed for the $Q_0 = 20$ case, but are much more apparent when $Q_0 = 5$. The Trouton ratio, which is the ratio of the viscosity to the elongational viscosity at low De is predicted by theory to be 4, and is show to be correct. Even for the case of $Q_0 = 5$ dumbbells, which

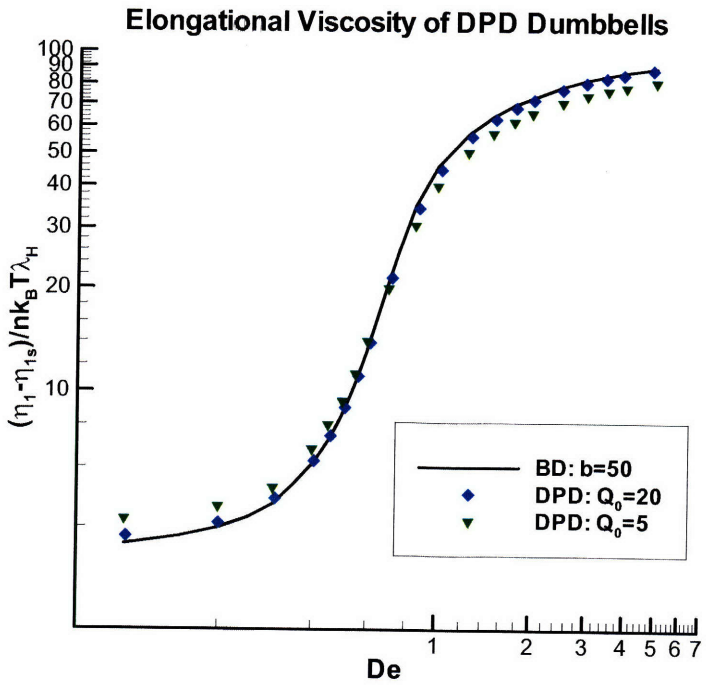

Figure 4-14: Elonagtional viscosity of DPD dumbbells in planar elongation flow

show the largest deviations from the BD results of any case presented, the Trouton ratio is preserved correctly, as both the shear and elongational viscosities are elevated.

Fractional Extension

The fractional extension in planar elongational flow is shown in Figure 4-15, showing very good agreement between DPD dumbbells and Brownian dynamics. As in the elongational viscosity, the longer DPD dumbbells show the greatest fidelity to the BD case over the full range of De. At low De, the shorter $Q_0 = 5$ dumbbells are slightly more extended, which is consistent with both shear flow, and equilibrium observations. Through the coil-stretch transition and above, the agreement between BD and the two DPD cases is remarkably good.

4.4 Conclusion

The central conclusion of the work presented here is that DPD is able to produce rheological results which match quantitatively the predictions from Brownian dynamics simulations. This represents the first attempt to match material functions produced via DPD simulations to those of a more widely studied model. While shear flow has been successfully reproduced in the past using DPD, the application of the Kraynik and Reinelt boundary conditions to the DPD model in order to simulate planar elongational flow is a first.

It has long been claimed that DPD produces both excluded volume and hydrodynamic interaction effects naturally due to the explicit modeling of the solvent with DPD particles. Little progress has been made in quantifying these claims, however. We have shown that using very long FENE dumbbells in DPD, which minimize the effects of both EV and HI, we are able to closely match the rheological results produced by a Brownian dynamics simulation which includes neither of these effects. As the length of the dumbbell is decreased relative to the DPD particle interaction length, deviations from the

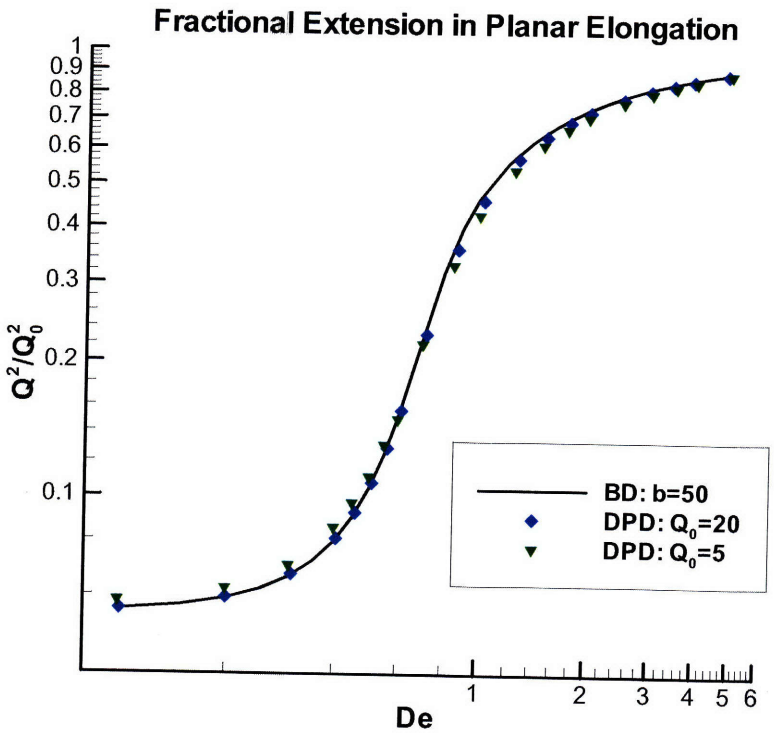

Figure 4-15: Fractional extension of DPD dumbbells in planar elongation flow

BD results begin to appear. First, at low strain rates, the excluded volume interaction between the dumbbell end beads forces the dumbbell to elongate more than is predicted by theory. This leads to larger values for the viscosity and first normal stress coefficient than are predicted by Brownian dynamics. This effect becomes progressively larger for shorter dumbbells. At large strain rates, DPD dumbbells of all lengths slightly underpredict the viscosity as compared to BD, with the deviation becoming more severe for shorter dumbbells. For the case of the longest dumbbells, we showed that this behavior is in agreement with Giesekus' anisotropic drag tensor model. In this way we propose a framework for interpreting the hydrodynamic interaction which has long been supposed to occur naturally in DPD systems. For shorter dumbbells, however, it is impossible to separate the HI behavior from the EV effect caused by endbead repulsion, and no conclusions concerning the utility of the Giesekus model could be reached.

Chapter 5

Non-Dilute Polymer Solutions

5.1 Introduction

In the previous chapter, we took pains to use DPD to simulate one of the simplest kinetic theory polymer models available, the FENE dumbbell, in order to show unambiguously the close agreement that is possible between DPD and another model. A polymer dumbbell, however, is a poor use of DPD, as it can be simulated more easily and more cheaply using other methods. In this chapter, we seek to explore some of the capabilities of DPD that make it attractive as a modeling method. The chief advantage of the DPD method is the flexibility the modeler has in constructing a model polymer molecule. The chemistry of the DPD particles can be adjusted easily to vary the makeup of the polymer or the solvent quality. The computational cost of increasing the number of beads in a bead-spring chain is roughly linear, and non-linear molecules are simulated as easily as straight-chain molecules. Finally, intermolecular interactions come about quite naturally, so concentration effects are included without a great deal of adjustment to the structure of the DPD model.

All these theoretical advantages of DPD were noted very early in its development as a model, but rheological studies of model polymer systems under flow using DPD have been slow in coming. In particular, there has been very little data reported concerning the

behavior of the material functions such as the viscosity and first normal stress coefficient as they vary with the strain rate. The goals of this chapter are thus two-fold; we wish first to simulate a polymer system which includes some of the reported advantages DPD enjoys in order to show that the model is capable of producing rheologically correct results. This first goal might be thought of as "proving the model". Having answered the first question of whether DPD *can* be used to study polymer rheology, we will then attempt to answer the more subtle question of whether it *should*. As noted in the previous chapter, DPD can be used to study a dilute system of polymer dumbbells, but the computational cost is far too great to make it worth the effort in practice when similar results can be produced using Brownian dynamics at a much smaller cost.

In this chapter we present a rheological investigation into systems of DPD bead-spring chain polymers undergoing shear and planar elongational flow. We examine the effect of both the solvent quality and of the concentration on the rheology of these solutions throughout the semi-dilute range. The practical limit of concentration that DPD is able to model is examined. For the specific case of planar elongational flow, this thesis represents the first report of DPD being used to model this type of flow. A spring-spring repulsion force is introduced to prevent springs from passing through each other.

5.2 Spring-Spring Repulsions

In Chapter 4, the challenge of establishing a condition of dilution was given much attention. We sought to show that individual DPD polymer molecules do not affect the rheological behavior of any other macromolecules in the simulation. In this chapter, we will attack the opposite problem. Rather than trying to avoid them, we seek to capture the effects of polymer beads and springs on each other in this chapter. In a solution or melt of DPD polymers, the individual macromolecules can affect each other through two methods. The first, which is present even in the dilute case, is bead-bead interactions. When we wished to simulate a dilute case, we restricted ourselves to a θ-solvent, so that

the interactions between solvent and polymer beads are indistinguishable. For concentrated solutions, that restriction can be relaxed. Pan and Manke [61] have examined the effects of solvent quality on the equilibrium configuration of DPD polymer chains by varying the repulsion force coefficient a_{ij}. In the case of that study, the only variation in the coefficient was for polymer-solvent interactions. Pursuing the idea further, one sees that the same principle can be applied to the architecture of a polymer molecule itself, so that a block copolymer could be modeled by designating a chemical species for each bead.

The other addition to the DPD model system that is required in order to move from the dilute to the concentrated regime is a spring-spring interaction. In the physical realm, two polymer coils can interpenetrate each other, but the backbones of two chains are not able to pass through each other. While a bead-spring chain is a highly simplified model of a polymer molecule, this steric hindrance must be retained if concentration dependent behavior is to be faithfully reproduced. The first step in implementing a spring repulsion force is to determine where the springs are relative to each other.

5.2.1 Determination of Inter-Spring Distance

Kumar and Larson[47] have proposed a method for calculating the closest approach distance between two line segments (polymer springs, in our case) in three dimensional space which we have adopted. The two springs are defined by their midpoints, $\mathbf{P}_1$ and $\mathbf{P}_2$, and $\mathbf{R}_1$ and $\mathbf{R}_2$, the vectors that govern their length and direction. If the springs are envisioned to lie along infinite lines, a vector $\mathbf{D}$ is defined as any vector connecting the two lines,

$$\mathbf{D} = \mathbf{P}_1 + t_1\mathbf{R}_1 - (\mathbf{P}_2 + t_2\mathbf{R}_2) \tag{5.1}$$

with t_1 and t_2 as parameters that define the location of the endpoints of the vector $\mathbf{D}$ on the lines. To find the point of closest approach between the lines, we find the minimum

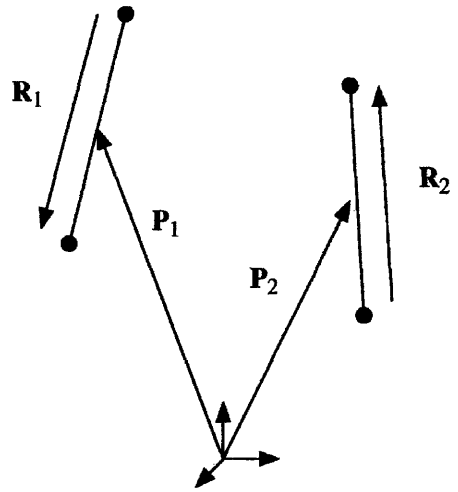

Figure 5-1: Nomenclature used in calculating the closest approach between springs: The vectors designating the spring midpoints are $\mathbf{P}_1$ and $\mathbf{P}_2$ while the length and direction of the springs are given by $\mathbf{R}_1$ and $\mathbf{R}_2$.

of the magnitude of $\mathbf{D}$, $D^2 = \mathbf{D} \cdot \mathbf{D}$, with respect to t_1 and t_2, requiring that

$$0 = \frac{\partial D^2}{\partial t_1} = \frac{\partial D^2}{\partial t_2}. \tag{5.2}$$

The solution of Eq. 5.2 leads to expressions for t_1 and t_2:

$$t_1 = \frac{(\mathbf{P}_1 - \mathbf{P}_2) \cdot (R_2^2 \mathbf{R}_1 - R_{21} \mathbf{R}_2)}{R_{12}^2 - R_1^2 R_2^2} \tag{5.3}$$

$$t_2 = \frac{(\mathbf{P}_2 - \mathbf{P}_1) \cdot (R_1^2 \mathbf{R}_2 - R_{21} \mathbf{R}_1)}{R_{12}^2 - R_1^2 R_2^2} \tag{5.4}$$

where $R_{21} = \mathbf{R}_1 \cdot \mathbf{R}_2$, $R_1^2 = \mathbf{R}_1 \cdot \mathbf{R}_1$ and $R_2^2 = \mathbf{R}_2 \cdot \mathbf{R}_2$.

It is important to note that the parameters t_1 and t_2 give the positions of the point of closest approach between the infinite lines, rather than the springs that lie along them. If $-0.5 < t_i < 0.5$ for both t_1 and t_2, we know that the points of closest approach occur along the length of each spring. If either t_1 or t_2 is outside the above interval, this signifies that the closest approach lies at the endpoint, and t_i is made equal to ± 0.5. In

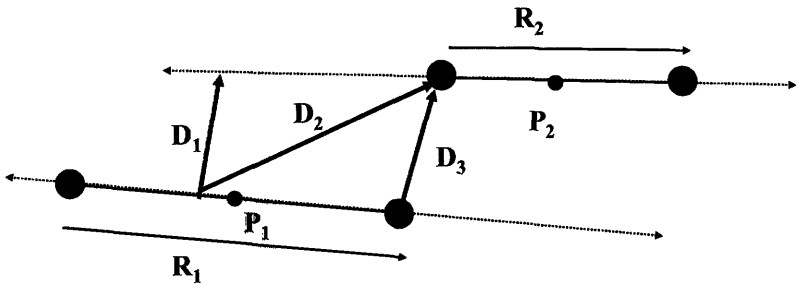

Figure 5-2: Failure of Kumar and Larson's method: Springs 1 and 2 are nearly parallel, and the closest approach between their defining lines intersects Spring 1 ($\mathbf{D}_1$). $t_2 < -0.5$, so it is reset to $t_2 = -0.5$, but since $-0.5 < t_1 < 0.5$, it is not reset, leading the algorithm to report $\mathbf{D}_2$ as the closest approach between the springs. The additional checks described here then identify $\mathbf{D}_3$ as the correct approach vector.

the event that only one of the t parameters is outside the interval, care must be taken, as very nearly parallel springs can cause the above algorithm to give incorrect results. This problem is illustrated in Figure 5-2.

When two springs are nearly parallel, it is possible for the vector of closest approach between the two *lines* to intersect one of the segments, while the shortest distance between the two *segments* themselves may pass only through the endpoints. In order to avoid errors of this type, a check is performed anytime $|t_i| > 0.5$. The magnitude of the distance vector, D is calculated for the four possible cases when $t_1 = \pm 0.5$ and $t_2 = \pm 0.5$. If any of these produce a shorter approach distance, t_i is changed accordingly.

5.2.2 Implementation of Spring-Spring Repulsions

Springs in the DPD simulations presented here can be as long as one-half the length of a side of the domain. Consequently, springs are frequently found to be lying across periodic boundaries. Under flow conditions the periodic images of the domain may be shifting past each other, as in shear flow with Lees-Edwards boundary conditions, or the domain itself may be deforming, as is the case for planar elongational flow. As a result,

the calculation of the distance between each pair of springs must be performed with some care.

Shear Flow with Lees-Edwards Boundary Conditions

Before any distances between individual pairs of springs are calculated in the spring repulsion algorithm, $\mathbf{P}_i$ and $\mathbf{R}_i$ for each spring is calculated and stored, where $\mathbf{R}_i = \mathbf{r}_{i+1} - \mathbf{r}_i$ and $\mathbf{P}_i = \frac{\mathbf{r}_{i+1}+\mathbf{r}_1}{2}$. Next, the components of $\mathbf{R}_i$ are checked to identify springs which lie across a periodic boundary. We establish x as the flow direction, y as the shear direction, and z as the neutral direction. The shear direction must be checked first. If $R_{iy} > 0.5L_y$, this tells us that the spring lies across the y-boundary. L_y is then subtracted from R_{iy}, and $0.5L_y$ is subtracted from P_{iy} Likewise if $R_{iy} < -0.5L_y$, then L_y is added to R_{iy}, and $0.5L_y$ is added to P_{iy}. This is the standard periodic treatment. Additionally in the case of shear flow, if the spring crosses the y-boundary, R_{ix} must also be corrected to account for the motion of the periodic boundaries. If $R_{iy} > 0.5L_y$, then δL_x is subtracted from R_{ix}, where δ represents the fractional distance the $+1y$ periodic domain has traveled. The flow direction is checked for boundary crossings next, and the process must be performed twice, as the addition or subtraction of δL_x in the first step can cause the spring to cross the flow-direction periodic domain twice. Finally, the neutral direction is checked.

Planar Elongational Flow with Kraynik and Reinelt Boundary Conditions

In planar elongational flow, the domain boundaries do not lie along the Cartesian directions, so identifying instances of springs lying across the periodic boundaries can be geometrically confusing. The situation is improved dramatically by performing a solid rotation of the domain about the neutral y-direction so that one boundary lies along an axis. The details of the spring boundary check for planar elongational flow can be found in Chapter 3.

Once the centerpoint and direction of each spring has been calculated, the distances between springs can be measured. Once again, we are faced with the possibility of springs interacting across periodic bounds. The first step is to measure the distance between the springs' centers: $\mathbf{D}_P = \mathbf{P}_2 - \mathbf{P}_1$. the vector $\mathbf{D}_P$ is then subjected to the same process which has been described in detail above as if it were a spring. The spring pair center-to-center distance allows us to calculate a minimum possible approach distance between the spring pair, which would occur if both springs were fully extended and lying along the same line, as illustrated in Figure 5-3. Having accomplished this first step, we are able to

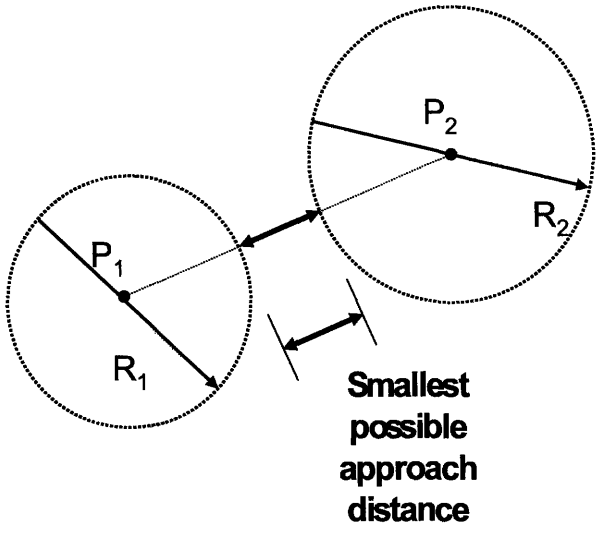

Figure 5-3: The center-to-center distance allows a minimum separation distance between the two springs to be calculated without knowing anything about the orientation of the springs. If the minimum possible distance is greater than the spring-spring interaction distance, the spring pair can be discarded without further calculation.

winnow down the list of spring pairs for which the actual closest approach distance must be calculated, as any spring pair for which D_P is greater than $\frac{R_1+R_2}{2} + \frac{r_c}{3}$ is geometrically precluded from experiencing an interaction. This greatly reduces the computational load

of calculating spring-spring interactions. We are further able to improve the algorithm efficiency by tabulating a list of spring pairs whose minimum approach distance is below a certain threshold which is somewhat larger than the maximum interaction distance of $\frac{r_c}{3}$. At subsequent timesteps, only the approach distances of these spring pairs must be calculated. The list is then updated at a longer interval by recalculating the approach distance of every spring pair in the simulation. For the polymer models and concentrations described in this chapter, it is sufficient to keep a list of particle pairs with approach distances less than r_c if the list is updated once every 20 timesteps.

Pan and Manke[62] made the first attempt to introduce a spring-spring repulsion to DPD polymers to allow them to simulate a melt. They chose a linear repulsion force law modeled after the DPD bead conservative force,

$$F^{(s)}(D) = \begin{cases} 3a_{ij}W^{(c)}D & \text{if } D < \frac{1}{3}r_c \\ 0 & \text{if } D > \frac{1}{3}r_c \end{cases} \tag{5.5}$$

Where a and $W^{(c)}$ are the conservative force coefficient and weighting function respectively. This results in a spring-spring repulsion force law with a slope nine times greater than that of the conservative force. (It should be noted that Pan and Manke worked with the original DPD thermostat, as opposed to the Lowe-Anderson modification employed here.) This linear force law has many of the same advantages and disadvantages of the DPD model as a whole. Even at very small spring separation distances, the linear force law produces a finite repulsion force, so larger timesteps can be taken without threatening the stability of the simulation. As is the case for DPD beads, however, a soft spring-spring potential leads to a greater likelihood that springs will cross each other despite the repulsion force. While it is expected, and not upsetting that DPD beads frequently overlap and pass through each other, the same cannot be said for polymer springs. It is thus necessary for the linear repulsion force to be accompanied by a very large coefficient, in order to assure that springs do not cross each other. The problem is

further exacerbated by having large timesteps (the chief advantage to a linear force law), as the repulsion coefficient must be increased even more as the length of the timestep is increased. In contrast to this method, Kumar and Larson [47] propose an exponential spring-spring repulsion force law given by Eq. 5.6.

$$F^{(s)}(r_{ij}) = A\alpha e^{-\alpha r_{ij}} \tag{5.6}$$

The relative merits of the exponential force law proposed by Kumar and Larson are roughly opposite to those of Pan and Manke's . The force law acts over a much shorter range, so the unphysical added pressure that results in the system due to the implementation of a spring-spring repulsion law is much smaller. On the other hand, at very small separation distances, the exponential repulsion force becomes very large. Smaller time steps must be taken in order to ensure the stability of the simulation. The repulsive force produced by the two laws is compared as a function of spring separation distance in Figure 5-4. The parameters A and α are chosen as a compromise between computational

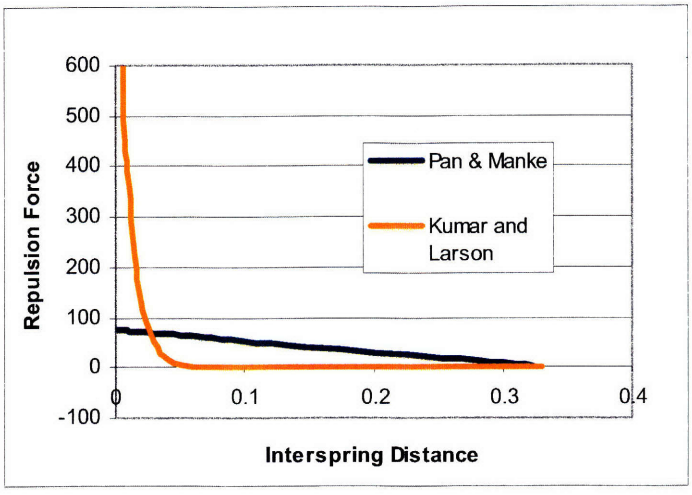

Figure 5-4: Spring-spring repulsions potentials proposed by Pan and Manke and by Kumar and Larson. The exponential potential has $A = 100$ and $\alpha = 10$.

convenience and efficacy in preventing spring crossing events. The choice of A has the

effect of controlling the inter-spring distance at which the force increases rapidly, while α controls the overall strength of the repulsion. While a larger α is more effective in preventing springs from crossing each other, it leads to a smaller maximum stable timestep size. In order to avoid rare destabilizing events in which two springs come very close to each other and thus experience an unphysically large repulsion force, a limit is placed on the allowable interspring distance. Any pair of springs found to be closer than $0.001r_c$ are treated as though their separation distance were $0.001r_c$. The choice of this safety valve setting balances a desire to prevent as many spring crossing events as possible, with a need to maintain stability in the simulation.

Spring Pair Distribution Function

In order to evaluate the effectiveness of the spring repulsion schemes presented above, some measure of the number of springs which are crossing each other is needed. While it is possible to identify instances of springs crossing each other geometrically, the algorithm for doing so is both tedious to implement, and costly to perform[47]. We instead look to a different method of evaluation that at once is easier to implement, and gives us other interesting information as well. As we have already identified all those springs which approach close enough to another spring to experience a repulsive force, it is trivial to produce a histogram of spring approach distances. This can also be thought of a pair-distribution function for springs within the DPD polymer solution. The population of the distribution function at spring separation distances very close to zero is an excellent representation of the relative frequency of springs crossing each other. In addition, this metric allows us to chart the shape of the distribution of spring separation distances, which allows us to better understand the effect on the structure of the polymer solution the inclusion of the spring-spring repulsion force has.

Effectiveness of Spring Repulsion Schemes

Figure 5-5 shows the spring pair distribution function for a solution of DPD $N = 20$ chains at equilibrium simulated for three cases; case1 is implemented with spring-spring repulsions enforced by Pan and Manke's algorithm, case 2 with the force law of Kumar and Larson, and case 3 with no repulsion force at all. One notices immediately that at

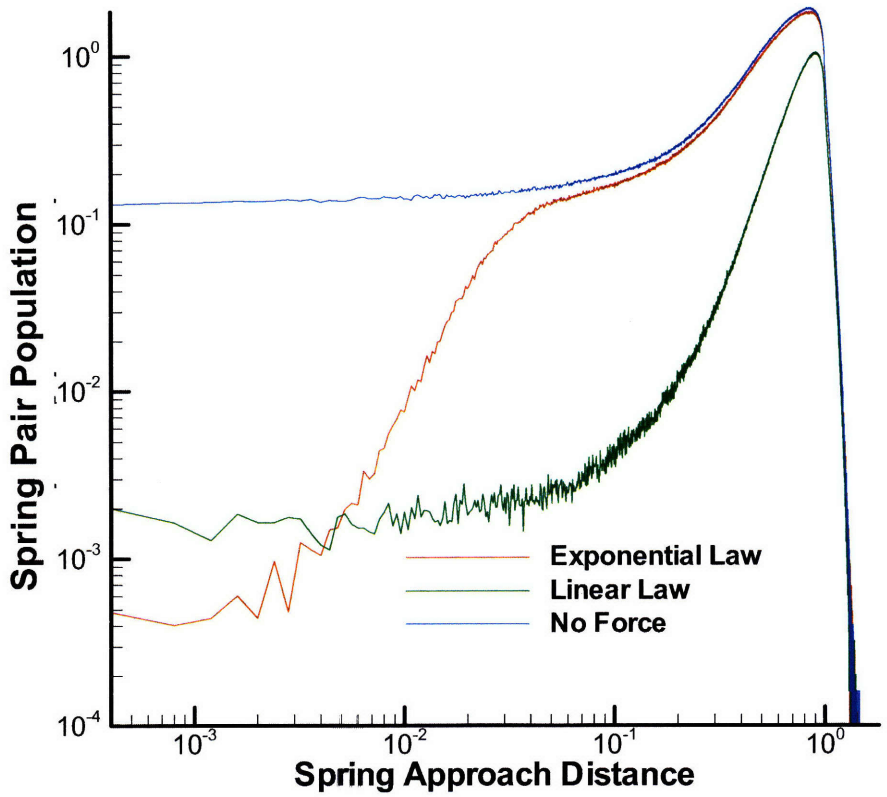

Figure 5-5: Spring pair distribution function for the two spring laws considered and for the case of no spring repulsions. The exponential force law produces a much more natural pair distribution function than does the linear force law.

spring separation distances very close to zero, both force laws result in a miniscule, though non-zero population of spring pairs. We thus learn that neither force law is capable of

completely eliminating spring crossing events, but that both are able to reduce their frequency to a negligible value. In this narrow sense, both algorithms are successful. We next look at the overall shape of the entire distribution function. In a physical sense, we are seeking to represent not a repulsive force, but rather a constraint. Physically, the backbones of individual polymer molecules cannot cross over each other. On the other hand, there is no reason for them to experience a repulsive force when they are merely close to each other. From this insight, we can glean that the ideal histogram profile would follow the curve of case 3 (no spring-spring repulsions) for any instantaneous snapshot in time. Here we see the superiority of the exponential force law of case 2, which shows a much smaller distortion in the overall shape of the histogram. This result is intuitive. A force law which acts over a shorter distance, and has a steeper slope is likely to yield a spring-spring distance distribution which hews more closely to the physical system which we seek to replicate. Against this ideal stands the practical limitation that we are simulating using discrete timesteps. Spring-spring repulsion laws which act over a shorter distance require smaller timesteps to maintain stability. Finally, we must note one additional difficulty that arises from our attempt to replace a constraint with a force law. An examination of Figure 5-5 shows that for each force law, there is a spring separation distance at which a sharp decrease occurs in the spring pair population. This coincides with the point at which the force begins to rapidly increase with decreasing separation distance. On can imagine that this critical distance defines a cylinder that surrounds each spring in the system, inside of which other springs are not tolerated. At low polymer concentrations, when the total volume of these "cylinders of force" is small in comparison with the volume of the domain as a whole, no unphysical effects are expected. On the other hand, as the concentration of polymers (and by extension, springs) in the system is increased, the total volume contained within these cylinders can approach or even exceed the total volume of the domain. When this happens, the total pressure force in the system increases dramatically, as springs are forced to invade each others' space, and strong unphysical ordering of the fluid is observed. At higher

concentrations still, the simulation almost always becomes unstable. As we are interested in non-equilibrium simulations, we must note that the same effect can be seen when the polymers are stretched by the flow. As the springs elongate, their cylinders of force gain volume, and the effect is the same as if the concentration were increased.

5.3 Bead-Spring Chain Polymer Model

In this work, flexible polymer molecules are modeled with a bead-spring chain constructed of DPD particles connected by entropic springs. This type of model is similar to those of Rouse and Zimm, with the exception that a different spring force law is chosen. Rouse and Zimm used Hookean springs, which are simple to use, and are amenable to the production of analytical results. For flows in the zero-shear rate regime, Hookean springs give adequate results, but at higher strain rates, they continue to elongate indefinitely. As a result, bead-spring chains constructed with Hookean springs are unable to model non-linear strain rate dependent properties such as shear rate dependence of the viscosity. True physical polymer molecules have a maxmium extension length, so a model which incorporates this limitation is desirable as well. We thus replace Hookean springs with finitely extensible non-linear elastic (FENE) springs instead. The FENE spring force law is given by

$$\mathbf{F}^s(\mathbf{Q}) = \frac{H\mathbf{Q}}{1 - \frac{Q^2}{Q_0^2}} \tag{5.7}$$

FENE springs are better able to capture non-linear rheological effects, but have been used less extensively for simulations, as analytical results are only possible with the inclusion of closure approximations due to the non-linearity of the spring-force law. For the simulations presented here, we have chosen to model the polymer molecule with chains of $N = 20$ beads connected by springs characterized by $Q_0 = 5$, and $H = 2$ which produces an extensibility parameter $b = 50$ for each spring. While the specific chain parameters have been chosen primarily for computational convenience, the choices

represent reasonable values for a short polymer chain molecule.

5.3.1 Polymer Concentration

For a solution of polymer and solvent molecules modeled with DPD, there are several ways of approaching the concentration of polymer. First and simplest, is the proportion of DPD particles in the simulation which are part of a polymer molecule. This is a useful measure internally to DPD, but does a poor job translating into other representations of polymer solutions because DPD particles are coarse-grained at a level which is somewhat ambiguous. The limited number density of DPD particles sets an unnaturally low upper limit on the concentration that can be achieved. Another method of measuring the concentration is based on the overlap concentration, c^*. The radius of gyration at equilibrium is defined as

$$R_G^2 = \sum_{i=1}^{N} (\mathbf{r}_i - \mathbf{r}_{CM})^2 \tag{5.8}$$

and gives an approximate measure of the radius of the polymer coil. c^* is defined as the concentration at which the total volume of polymer coils is equal to the total system volume. The volume inhabited by a single polymer coil is given by

$$V^{coil} = \frac{4}{3}\pi R_G^3 \tag{5.9}$$

so $c^* = 1$ when $nV^{coil} = V^{system}$. Scaling the concentration by c^* gives a new measure of concentration

$$c/c^* = \frac{\frac{4}{3}n\pi R_G^3}{V^{system}} \tag{5.10}$$

which gives an estimate of the level of interpenetration which should be expected among polymer molecules.

5.3.2 Solvent Quality

Solvent quality describes the chemical relationship between polymer and solvent molecules in solution. The simplest case is a θ-solvent, in which the chemical affinity of the polymer to itself is the same as its affinity for the solvent. In a poor solvent, the polymer prefers itself, and in a good solvent, the polymer prefers the solvent. Up to this point, we have worked exclusively with DPD as a θ-solvent. To form a θ-solvent in a DPD context, one simply sets a_{ij}, the conservative force coefficient, to be the same value for all pairs of particles, regardless of their identity as polymer or solvent. Following Groot and Warren[37] this value is set at $a_{ij} = 75/\rho$, or 18.25 for our simulations in which $\rho = 4$. A number of authors have explored using DPD to simulate polymers in both good and poor solvents. Kong *et al.*[61] have shown that a solution of polymer molecules in good solvent can be reproduced by setting a_{ij} to a lower value for pairwise interactions of a polymer and a solvent DPD particle, while maintaining the original repulsion value for both polymer-polymer and solvent-solvent interactions. Following their example, we model a solution of polymer in good solvent with the following conservative force law rules:

$$\text{Polymer-Polymer:} \quad a_{ij} = 18.25 \tag{5.11a}$$

$$\text{Solvent-Solvent:} \quad a_{ij} = 18.25 \tag{5.11b}$$

$$\text{Polymer-Solvent:} \quad a_{ij} = 13.125. \tag{5.11c}$$

This is a 30% reduction in the repulsion between unlike DPD beads. A number of effects result from this treatment which ought to be noted. The first, and intended consequence is an additional effective excluded volume potential between polymer beads, as compared to the θ-solvent case. The lower repulsion value for polymer-solvent interaction causes greater interpenetration of the polymer coil by solvent particles, which leads to a larger equilibrium coil size. We note that there is not, in fact, any excluded volume force being added, but rather a removal of some system pressure due to the reduced repulsion

between unlike polymer and solvent species. This leads to a second effect, in which the relative concentration of polymer vs. solvent particles in the solution changes the system pressure. At a ratio of 1 : 1 polymer to solvent beads, there is a minimum in the system pressure. As a result, there is no way to simulate an infinitely dilute solution of the good

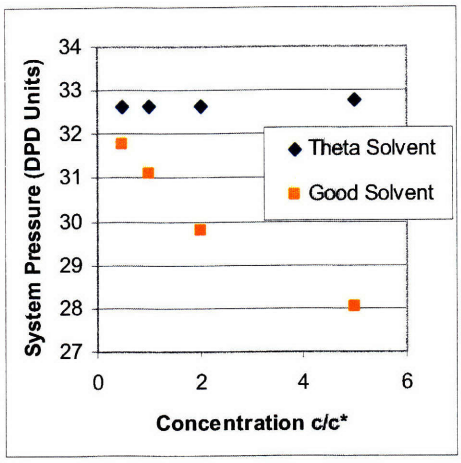

Figure 5-6: In a good solvent, the total system pressure depends on the polymer concentration due to the lower conservative force coefficient between unlike particles.

solvent case, as was done for a θ-solvent in the previous chapter. There will always be a concentration dependence on the system pressure.

In Figure 5-7 we show the behavior of the radius of gyration at equilibrium as a function of concentration for each solvent quality case. In the case of the θ-solvent, there is a small dependence of the coil size on concentration, as spring-spring repulsions limit the degree to which polymers coils can inhabit the same volume. The same effect is seen much more dramatically in the good solvent case, primarily because the coils are much larger at low concentration.

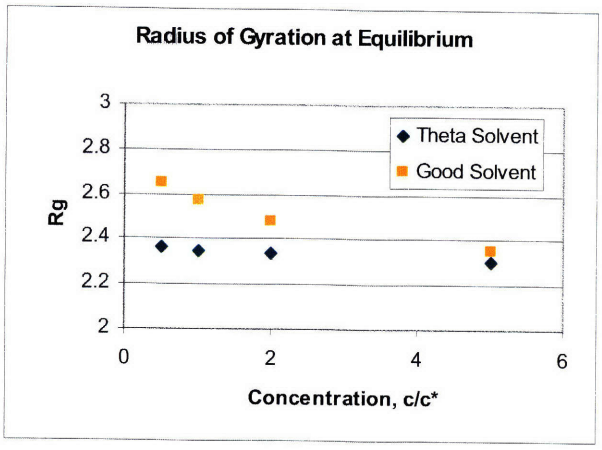

Figure 5-7: Radius of gyration of $N = 20$ bead-spring chain molecules at equilibrium for the range of concentration studied. The swelling of the coil in good solvent is restricted as the concentration increases.

5.4 Simulation Details

5.4.1 Planar Elongational Flow Experiments

Steady planar elongational flow is a homogeneous shearfree flow where ∇v is given by

$$\nabla v = \begin{pmatrix} -\dot{\varepsilon} & 0 & 0 \\ 0 & 0 & 0 \\ 0 & 0 & \dot{\varepsilon} \end{pmatrix}. \tag{5.12}$$

We note that in shearfree flows, the velocity gradients are in the flow directions, so the position of a fluid element changes exponentially as the fluid moves away from the origin. The total strain is measured in Hencky Strains, defined as

$$\epsilon = \dot{\epsilon} t \tag{5.13}$$

This type of flow leads to very strong deformation of the polymer shape. The flow is modeled in a periodic bounded domain with affinely deforming boundaries according to the method of Kraynik and Reinelt[46] (KR). The KR boundary system is periodic in both space and time, so the simulation represents an infinite bulk which can be simulated indefinitely. We are thus able to simulate the planar elongational flow over a long period of time, and can consequently reach very large Hencky Strains. Perkins *et al.*[63] have shown that polymer coils which are subjected to an elongational flow very near the critical coil-stretch transition strain rate reach their equilibrium length very slowly. Each individual molecule begins to uncoil at a random time which is not system dependent or predictable. As a result of this, the time to equilibrium becomes very long for the strain rates which are most interesting to us, over the range of elongation rates at which the steady state behavior changes most rapidly. As a result, planar elongation simulations near the coil-stretch transition are run for 75 Hencky strains, which provides a long enough time to reach equilibrium, followed by a period sufficient to sample the rheological behavior of the fluid.

In the extreme of low concentration, the challenge to modeling is one of computational expense. Specifically, as solvent must be simulated explicitly along with polymer, a low concentration results in a large overhead of solvent molecules for each polymer molecule in the simulation, and a minimum number must be present to obtain satisfactory levels of stochastic error. At high concentration, the limiting factor is based on the spring repulsions. If there are too many springs present, the timestep must be reduced significantly to maintain the stability of the simulation. The $N = 20$ polymer is studied at four concentration levels, corresponding roughly to $c/c^* = 0.5$, 1, 2, and 5. As a percentage of the DPD particles in the simulation which are polymer, this corresponds to 5%, 10%, 20% and 50%. It should be noted that the relationship between polymer fraction and concentration scaled by $c*$ is established by the coil size at equilibrium of the polymer under investigation, and would not be constant across other polymer models, including changes in N, Q_0, and H.

In addition to the variation in concentration, the simulation experiments were performed once under good solvent conditions, and once under θ-solvent conditions, so that the effects can be compared. The solvent quality has a strong effect on the equilibrium size of the polymer coil, and by extension affects the c^* concentration. For simplicity, the domain size and number of macromolecules was held constant for the good and θ-solvent simulations. As a result, we will be comparing simulations which have matching number concentrations, as opposed to matching c/c^* concentrations.

Strain Rate

The rate of strain is expressed as the Deborah number,

$$De = \frac{\dot{\varepsilon}}{\lambda_0}, \tag{5.14}$$

which scales the elongation rate with the longest relaxation time. At each concentration, a series of planar elongational flow simulations was performed, for a range of Deborah numbers, $0.05 < De < 3$, which is sufficient to observe the transition from a coil to a fully extended molecule. For each solvent quality condition, the set of elongation rates used was held constant across all four concentration setpoints. As we will show shortly, however, the concentration of polymer in the solution has a strong effect on the longest relaxation time of the polymers in solution. Thus there are two measures of the strain rate which may be used. The first is based on the relaxation time of the lowest concentration solution, $c/c^* = 0.5$, which is as close to dilute as we are able to simulate. In this way, the results of all concentrations can be compared on the basis of equivalent absolute strain rate. This will be denoted by $De_{0.5}$. Alternately, the results of each concentration setting can be scaled by the longest relaxation time calculated individually for said concentration, denoted by De.

Determination of Longest Relaxation Time

A bead-spring chain possesses a relaxation spectrum, which receives contributions from each of the relaxation modes (springs) in the molecule. We will eschew trying to accurately determine the entire spectrum in favor of measuring just the longest relaxation time, which has the largest effect on the coil-stretch dynamics of the molecule as it undergoes deformation. The longest relaxation time of chain molecules is dependent on the number of beads, N, the FENE spring-law parameters Q_0 and H, and the solvent viscosity, as controlled by the thermostatting frequency, Γ. There is no reliable predictive measure of the longest relaxation time, so a simulation experiment must be performed instead. Polymer molecules which have been fully stretched are allowed to relax back to equilibrium. The squared end-to-end vector decays according to

$$L^2 = L_0^2 e^{-t/\lambda_0} + L_e^2 \tag{5.15}$$

where L_0 is the contour length of the molecule, and L_e is the end-to-end vector at equilibrium, and λ_0 is the longest relaxation time. We take advantage of the fact that we already have a ready-made test cell in the elongational flow code. The solution to be tested is subjected to a planar elongation rate well above the coil-stretch transition for a sufficient time to ensure that all polymer molecules have reached nearly full elongation. The elongation rate is then reset to zero, and the solution is allowed to return to equilibrium. The value of the mean squared end-to-end vector is then fit to a curve of the form given in Eq. 5.15 using MATLAB's curve-fitting toolbox. For each concentration and solvent quality, the simulation was run three times, and an average resultant longest relaxation time calculated. Figure 5-8 illustrates these results. The dependence of time constant on concentration is given in Figure

5.4.2 Dynamic Results

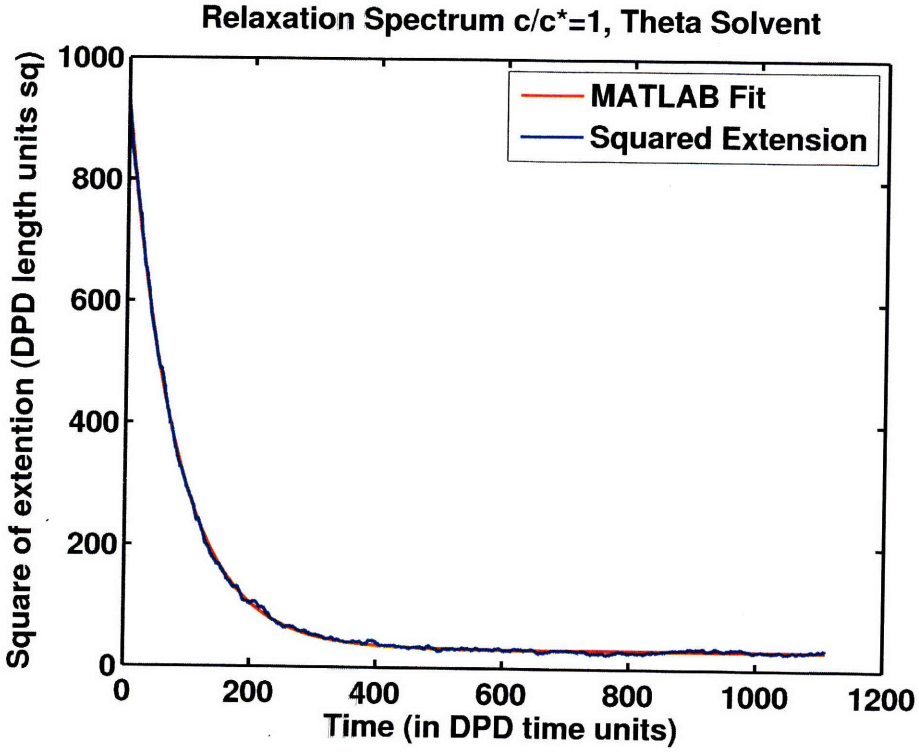

Figure 5-8: Decay of the squared end-to-end vector, fitted to an expontential curve in order to measure the relaxation time.

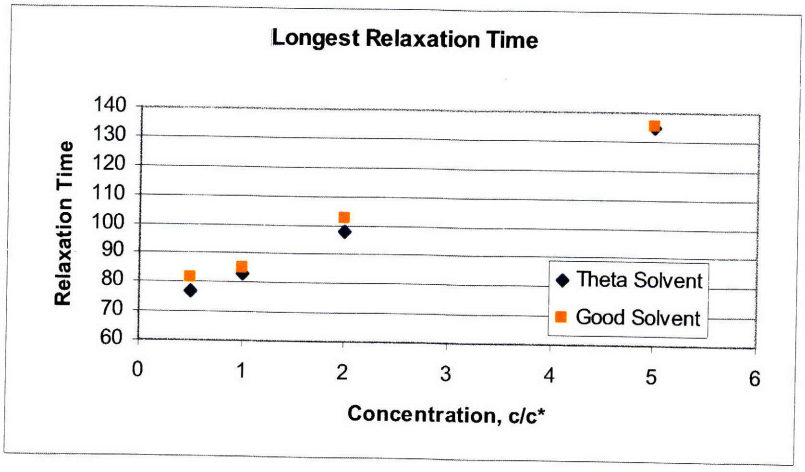

Figure 5-9: Relaxation time vs. concentration for both good and θ-solvents

We will begin with an examination of the evolution of the polymer molecules' shape under elongational flow. We consider the length of the end-to-end vector as a function of the two measures of the Deborah number described previously.

Extension

In Figure 5-10 we consider the evolution of the end-to-end vector of polymers immersed in a θ-solvent, scaled by $\mathrm{De}_{0.5}$ as calculated for the $c/c^* = 0.5$ case. In Figure 5-11 we

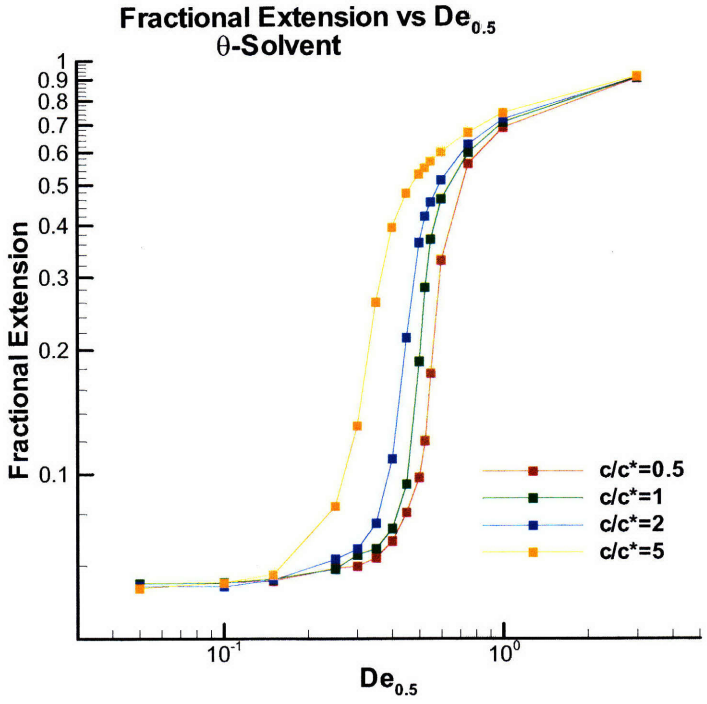

Figure 5-10: Fractional extension in planar elongational flow in a θ-solvent. The strain rate is scaled by the relaxation time of the $c/c* = 0.5$ solution. The fractional extension is defined as the total molecule length scaled by the contour length.

present the same extensional data as a function of De as calculated for each individual solution. We note immediately that there is a strong concentration dependence on the

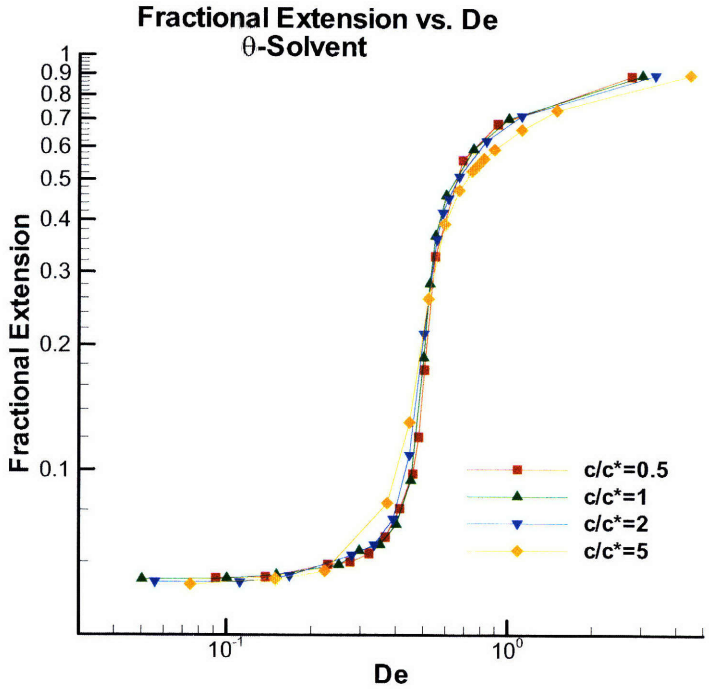

Figure 5-11: Fractional extension vs. De in planar elongational flow in a θ-solvent.

elongational flow rate at which significant extension of the molecules begins. When the curves are rescaled by the relaxation times of the individual solutions, they all collapse onto a single curve, with a sharp coil-stretch transition evident at De = 0.5 This is the result predicted by theory. At the largest concentration, $c/c^* = 5$, there is a broadening in the extension curve. The molecules begin to elongate at a lower De, and reach full extension more gradually as the De increases. This behavior suggests a broadening of the relaxation spectrum for the solution.

Figures 5-12 and 5-13 show the concentration dependence of the molecular extension behavior in a good solvent. We observe once again that the dependence of the relaxation

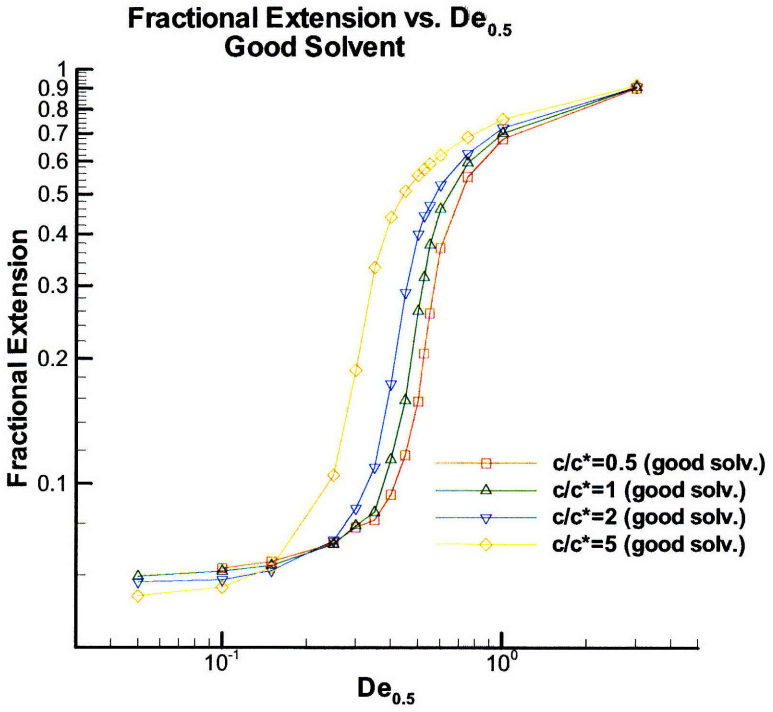

Figure 5-12: Fractional extension in planar elongational flow in a good solvent. The strain rate is scaled by the relaxation time of the $c/c* = 0.5$ solution.

time on concentration manifests itself as an earlier onset of the coil-stretch transition as the concentration is increased. Unlike the θ-solvent case, however, there is also a clearly

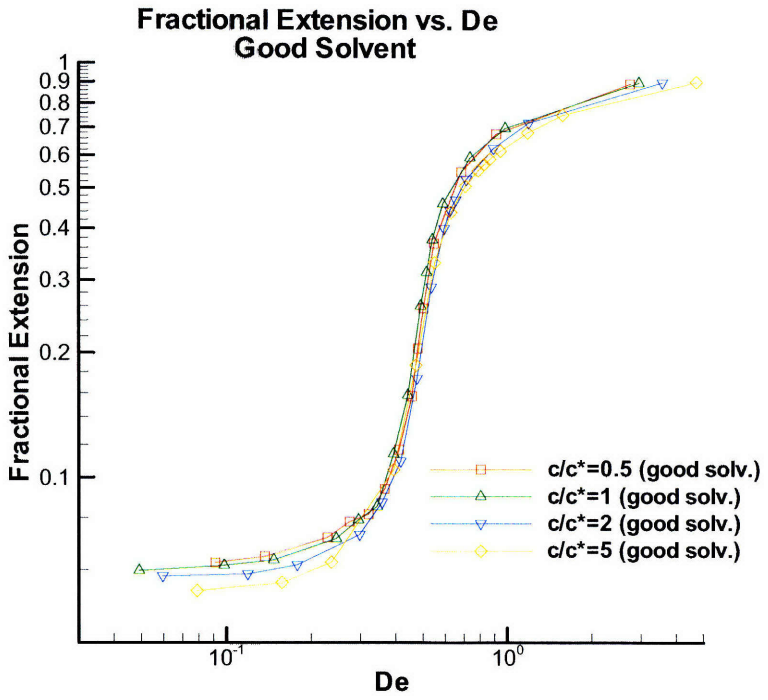

Figure 5-13: Fractional extension in planar elongational flow vs. De in a good solvent.

visible dependence on the molecular size at very low De, where the influence of the flow is not great. As the concentration grows, the size of the molecule shrinks. This is consistent with the R_G behavior at equilibrium. In the good solvent, polymer beads repel each other, so at low concentration, each coil expands as much as possible. As the concentration increases, however, the coils begin to overlap, and the beads are repelled by other polymer molecules, which leads to a smaller coil. This behavior is also consistent with the results reported by Stoltz et. al. [76]

We now consider a direct comparison between the extension behavior of like concentrations which differ only in the solvent quality. Figures 5-14 through 5-17 show the fractional extension behavior of each solution in θ and good solvent. The Deborah num-

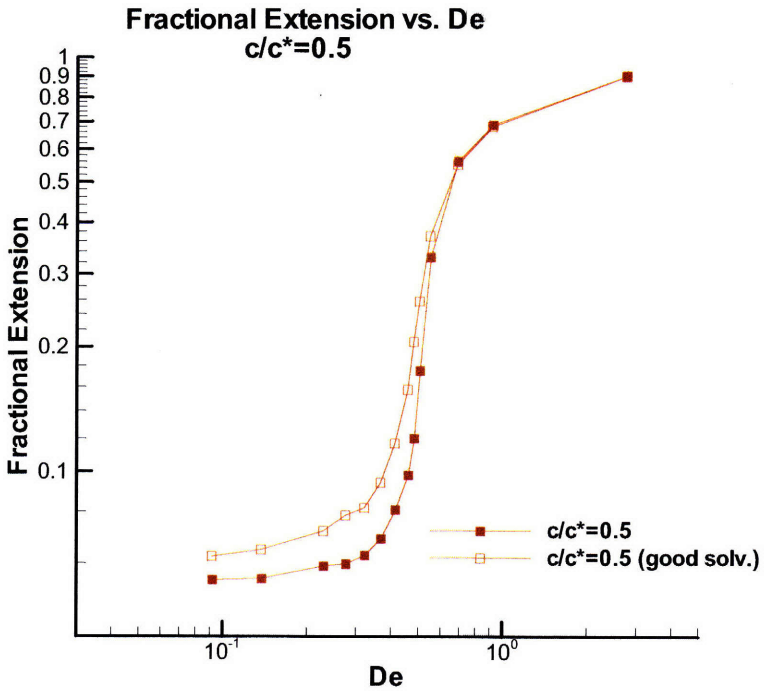

Figure 5-14: Fractional extension vs. De with $c/c* = 0.5$. The θ-solvent is represented by closed symbols, the good solvent with open.

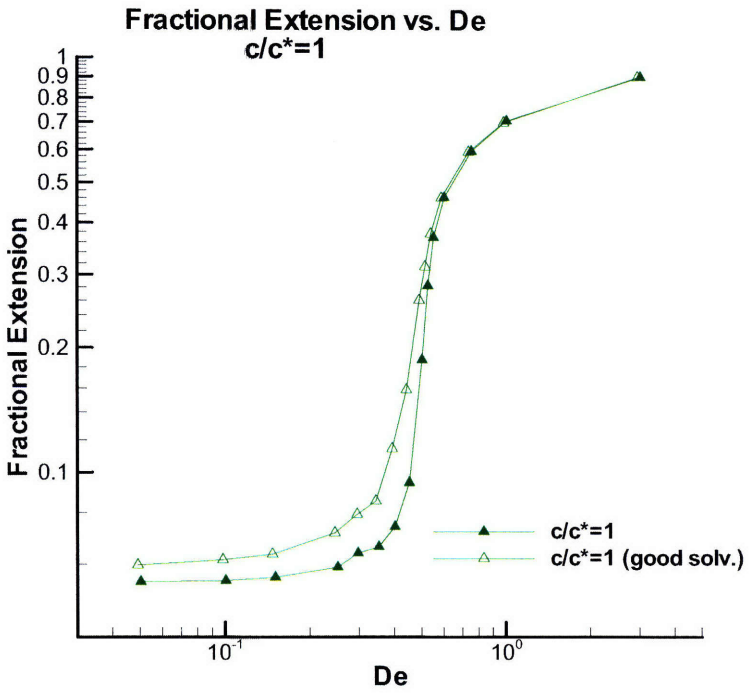

Figure 5-15: Fractional extension vs. De with $c/c* = 1$. The θ-solvent is represented by closed symbols, the good solvent with open.

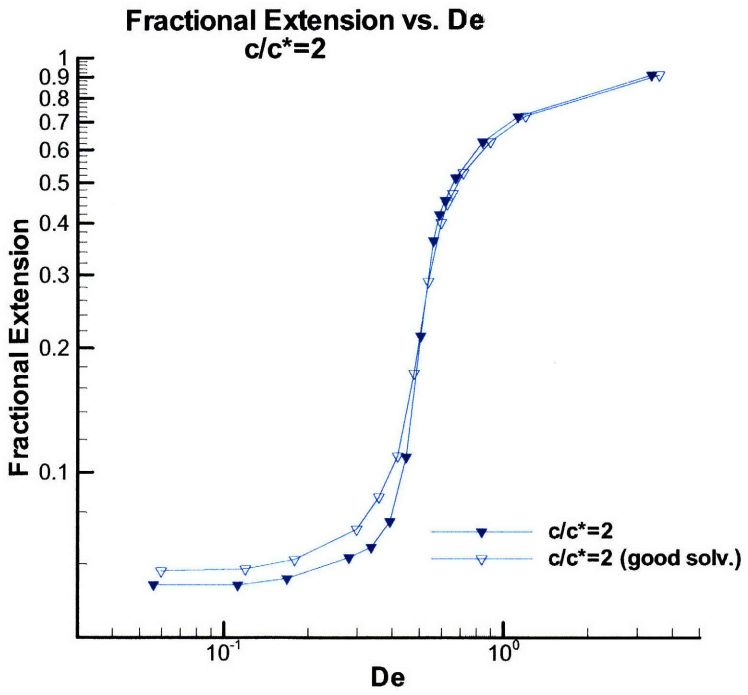

Figure 5-16: Fractional extension vs. De with $c/c* = 2$. The θ-solvent is represented by closed symbols, the good solvent with open.

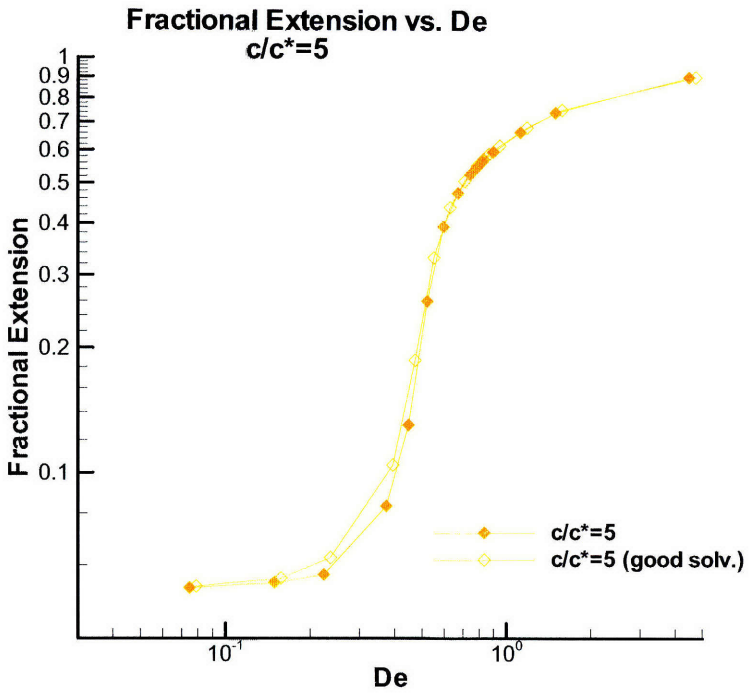

Figure 5-17: Fractional extension vs. De with $c/c* = 5$. The θ-solvent is represented by closed symbols, the good solvent with open.

ber for each series is calculated based on the individual relaxation time of the solution. Beginning with $c/c^* = 5$, we observe very little difference in the elongation between the two solvent types, which indicates that at this high level of concentration, the excluded volume effect is less important. At lower concentrations, we see that the fractional extension at low De is comparatively greater for the good solvent as the concentration decreases. The larger equilibrium coil size observed in the good solvent also contributes to an earlier onset of the coil-stretch transition. At high De, the fractional extension curves overlap at every concentration which suggests that, as the molecules are fully extended, there is little important interaction between polymer chains.

Elongational Viscosity

In planar elongational flow, the evolution of the polymeric contribution to the elongational viscosity as the strain rate changes is dominated by the strong deformation of the polymer molecules. As opposed to shear flow, in which the viscosity is observed to decrease as the strain rate is increased, the viscosity of a polymer solution under elongational flow undergoes a rapid increase as the polymer molecules transition from a coiled to an extended shape. Below the critical strain rate De = 0.5, the polymer molecules remain more or less in a coiled state, although there is some deformation of the coil shape. At the critical strain rate, however, the combination of the deformation due to the contraction flow in the x-direction and the expansion flow in the z-direction become great enough to cause the polymer molecules to elongate and take on a linear shape. In the elongation direction, the hydrodynamic drag force on a polymer bead increases exponentially with separation distance, so once a molecule begins to unravel, the process is rapid and irreversible as long as the polymer remains in the flow field. Figures 5-18 and 5-19 show the elongational viscosity behavior of the $N = 20$ chains in a θ-solvent scaled by $\mathrm{De}_{0.5}$ and De respectively. The elongational viscosity is scaled by the inverse of the concentration, c^*/c which eliminates the linear dependence of the polymer viscosity on the concentration. The shape of the viscosity curve is similar to the fractional elongation

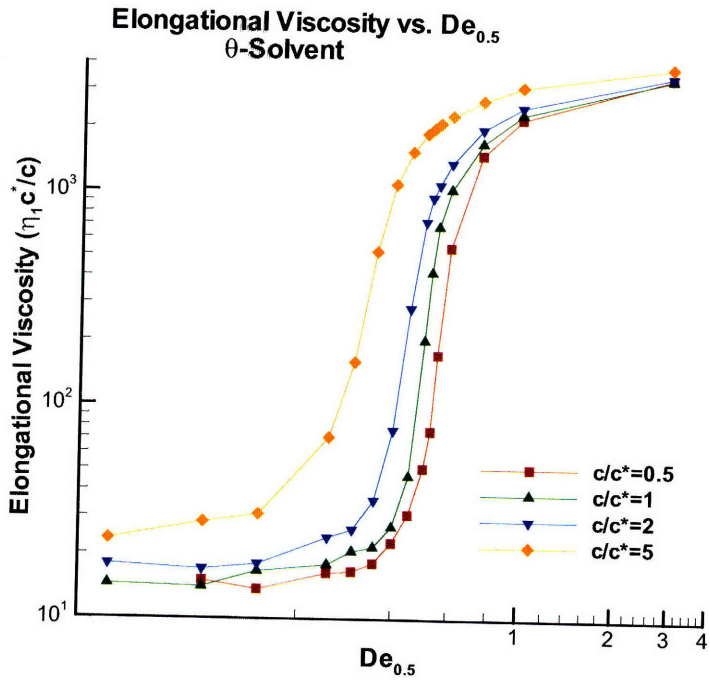

Figure 5-18: Elongational viscosity in a θ-solvent vs. $De_{0.5}$ in planar elongational flow

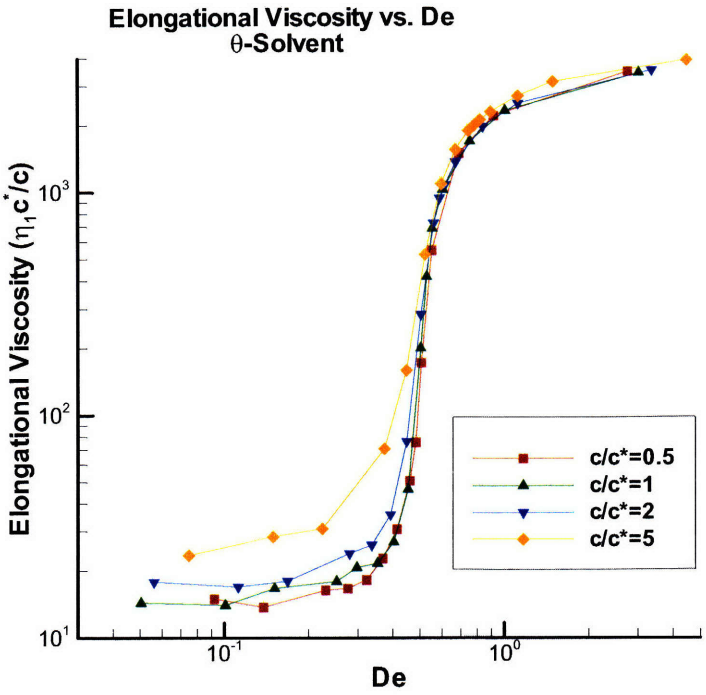

Figure 5-19: Elongational viscosity in a θ-solvent vs. De in planar elongational flow

curve. Once again, we see that the coil-stretch transition occurs at an earlier strain rate as the concentration increases. Examining Figure 5-19, we note that there is a small concentration dependence of the viscosity at low strain rate, but that the coil-stretch transition occurs at De = 0.5 for all concentrations. At large strain rates, there is no observable concentration dependence, as the molecules are highly elongated and are not expected to interact with each other significantly.

Figures 5-20 and 5-21 show the elongational viscosity of the $N = 20$ chains in a good solvent. As the concentration increases, the coil-stretch transition occurs at a lower

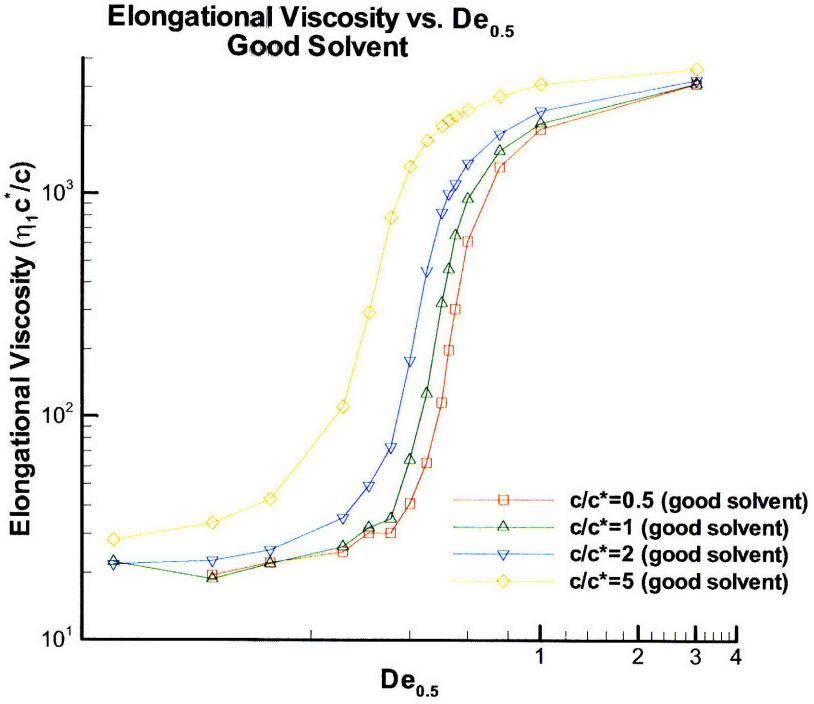

Figure 5-20: Elongational viscosity in a good solvent vs. $De_{0.5}$ in planar elongational flow

absolute strain rate. When the data is rescaled according to the individual relaxation times, in Figure 5-21, we see different behavior than the θ-solvent case. At low elongation rates, only the highest concentration, $c/c^* = 5$, shows an elevated viscosity. In order to

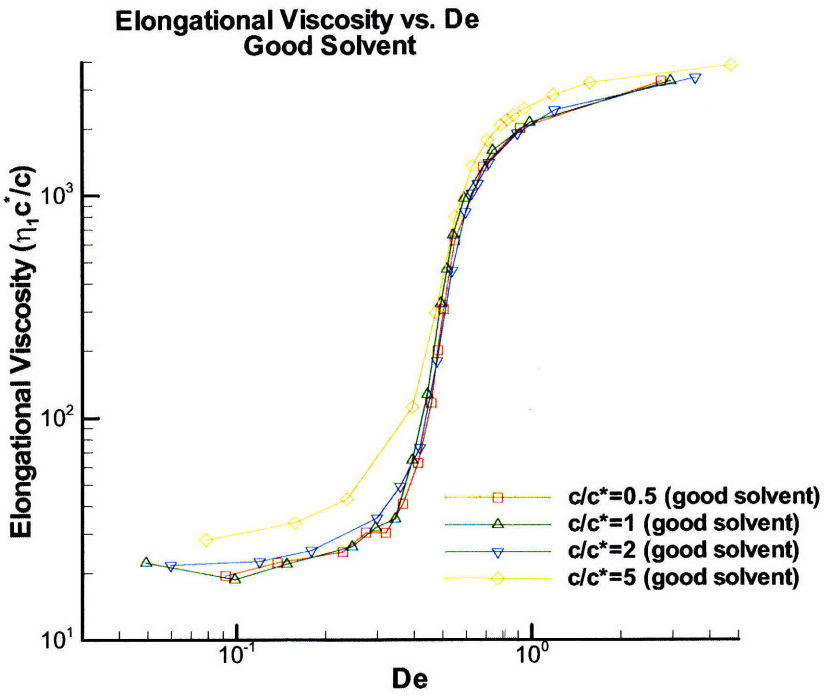

Figure 5-21: Elongational viscosity in a good solvent vs. De in planar elongational flow

understand this, we look back at the fractional elongation data in Figure 5-13. There are two opposing effects at work here. As the concentration increases, the movement of the macromolecules is hindered by the presence of other polymers, which tends to increase the viscosity, as illustrated by the θ-solvent case. On the other hand, the smaller coil size observed in Figure 5-7 is likely to decrease the viscosity. At large strain rates, the highest concentration shows a greater viscosity, in contrast to the θ-solvent case. It is likely that the excluded volume effect is the cause of this, as the polymer beads are likely to come into contact with each other regardless of the shape of the macromolecules.

In Figures 5-22 through 5-25 we show direct comparisons of the good and θ-solvent elongational viscosity vs. De for each individual concentration studied, in order to more closely examine the solvent quality dependence. The most immediately notable difference between the solvent types across all concentrations is that the good solvent always shows a larger elongational viscosity at low strain rate. This is directly related to the larger coil size exhibited by the polymer molecules in the good solvent. The relative difference between the low-strain viscosity of the two solvent types does decrease as the concentration is increased. This effect is in harmony with the suppression in equilibrium coil size observed in the good solvent as the concentration is increased. The case of $c/c* = 5$ is especially instructive, because there is little difference observed in the fractional extension at low strain rate, but there is a much larger difference in the elongational viscosity. This implies that the EV interaction of the good solvent also makes a contribution to the elongational viscosity which is independent of the effect created by the larger coil size.

At the point of the coil-stretch transition, we note that the θ-solvent experiences a much sharper transition, so that the range of De over which the molecule becomes fully elongated is smaller than in the good solvent case. Once a strain rate at which the molecules are fully stretched is reached, however, the curves lay atop one another. This illustrates a transition in which the EV interaction of the good solvent case becomes less and less important. Finally, at high strain rates, the θ-solvent shows a slightly larger

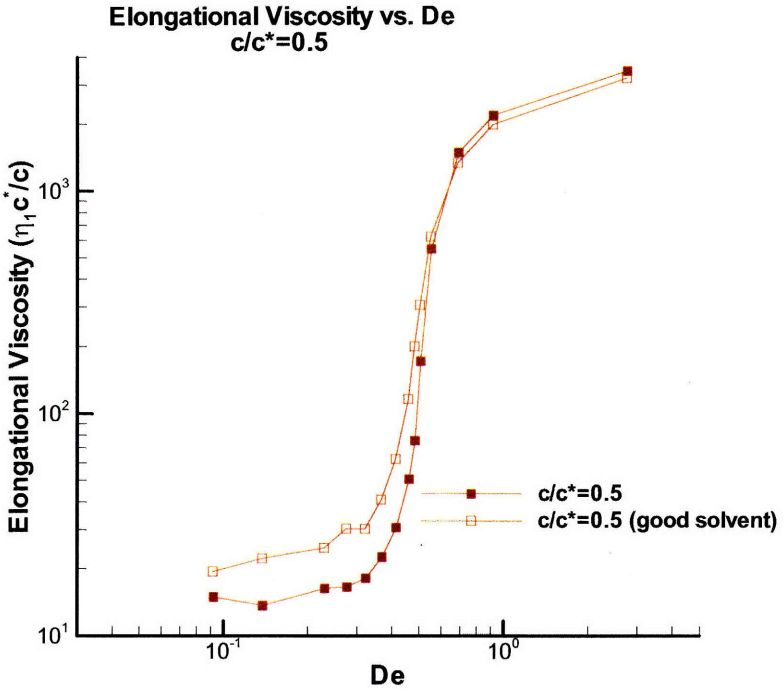

Figure 5-22: Comparison of the elongational viscosity of $c/c* = 0.5$ vs. De betweeen the good and θ-solvent cases.

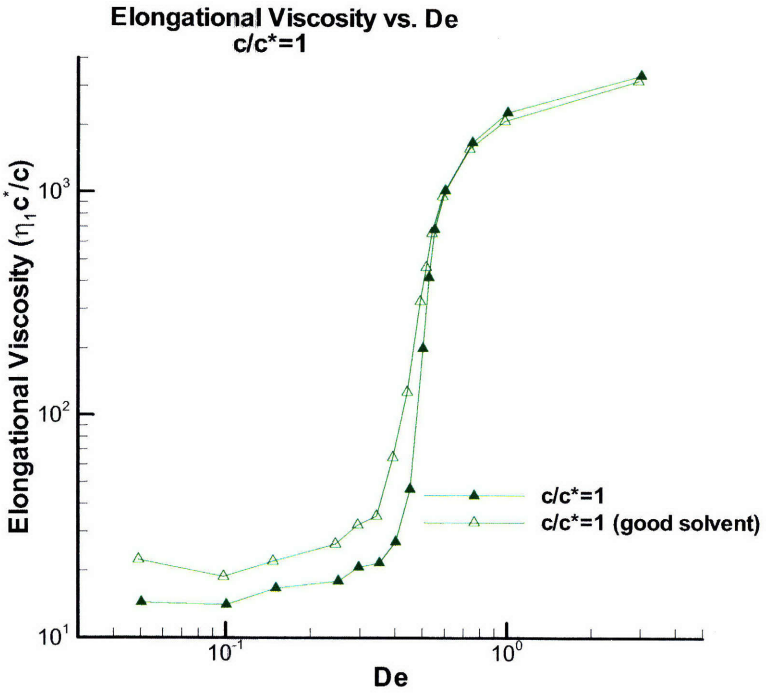

Figure 5-23: Comparison of the elongational viscosity of $c/c* = 1$ vs. De betweeen the good and θ-solvent cases.

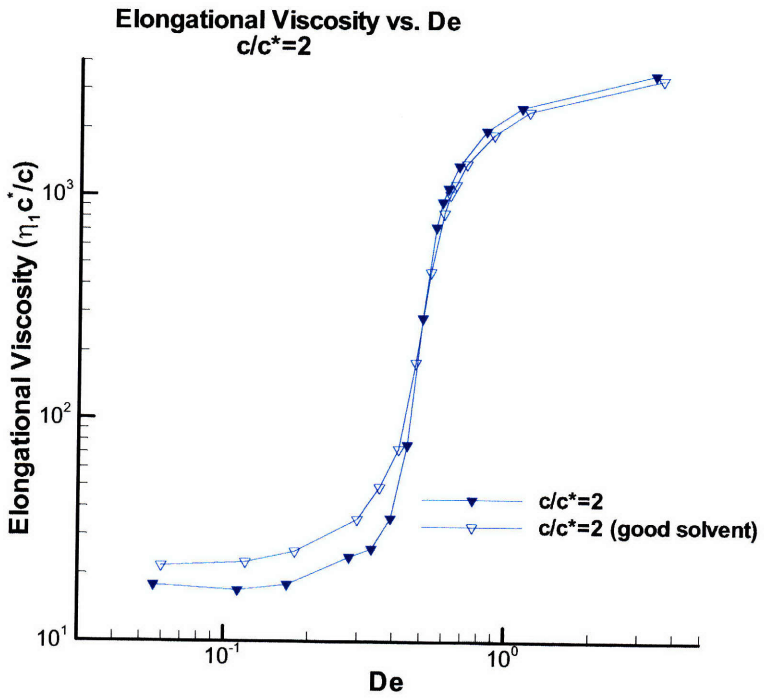

Figure 5-24: Comparison of the elongational viscosity of $c/c* = 2$ vs. De betweeen the good and θ-solvent cases.

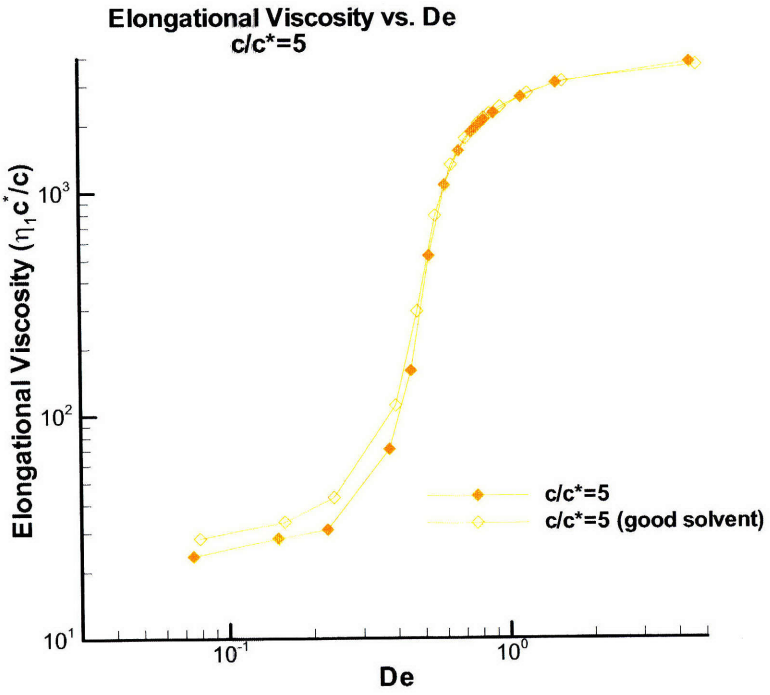

Figure 5-25: Comparison of the elongational viscosity of $c/c* = 5$ vs. De betweeen the good and θ-solvent cases.

elongation viscosity, with the effect tapering off as the concentration is increased.

Effect of Spring-Spring Repulsions

The computational cost of preventing springs from crossing each other is quite high, so it is instructive to examine the importance of this portion of the model in determining the behavior of the solution. Stoltz *et al.*[76] used Brownian Dynamics to study the planar elongation of bead-spring chains in a good solvent only, and determined that the excluded volume potential was sufficient to prevent chains from crossing each other, and so eschewed the use of a spring-spring potential. While this logic potentially has currency for the good solvent case, it is surely not applicable to a θ-solvent, in which no net EV potential should exist. In Figure 5-26 we present the added pressure in the system due to spring-spring repulsions for all eight elongation series presented thus far. The added pressure is normalized by the number of macromolecules in each solution to eliminate the linear concentration dependence. This metric serves as a proxy for the number and importance of spring-spring repulsions in the solution. At a first pass, we note immediately that while there is a visible difference in the behavior of the good and θ-solvent solutions, the concentration is clearly the dominant factor in determining the likelihood of springs coming into contact with each other. We will begin by examining the good solvent behavior. The added pressure depends strongly on the concentration, and increases through the coil-stretch transition. The sudden increase in pressure at the coil stretch transition is a little counter-intuitive in that an elongated molecule is not expected to interact with other molecules as strongly as a coiled molecule. Opposing this is an artifact of the polymer model being used. Each spring is surrounded by a cylindrical volume of exclusion. As the individual springs in each polymer molecule are stretched, the total exclusion volume in the domain is increased, which results in more powerful and more frequent spring-spring repulsion events. Nonetheless, at the highest concentration we are able to observe a decrease in the spring repulsion at the highest strain rate, as the effect of the molecules lining up overcomes the affect of the added exclusion volume.

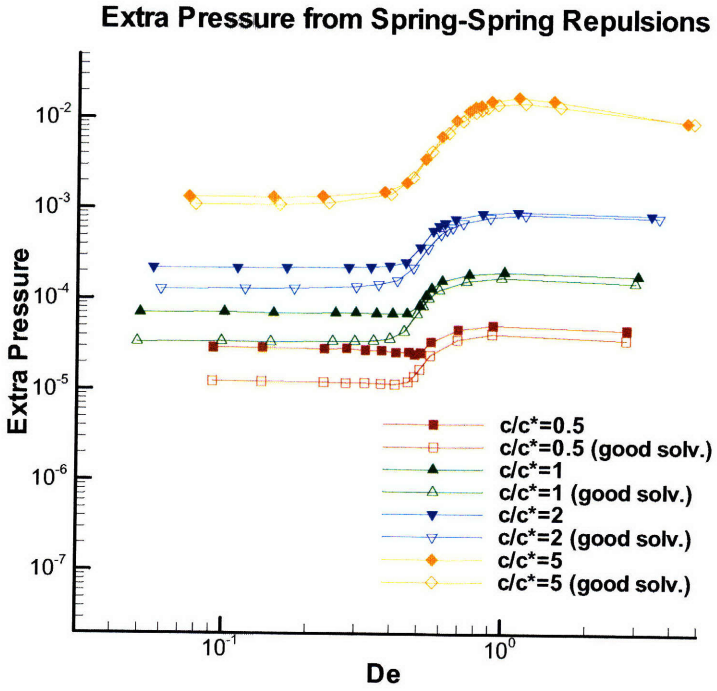

Figure 5-26: Extra pressure in the system due to spring-spring repulsion forces; The extra pressure is a proxy for the number and intensity of spring repulsion events within the flow.

The θ-solvent case shows some additional interesting results. Overall, a greater extra pressure is experienced in the θ-solvent case at each concentration level. The lack of an EV interaction between polymer beads is chiefly responsible for this, as it has the effect of screening polymer molecules from each other in the good solvent case, but not in the θ-solvent case. At the lowest concentration, another effect is visible. The total extra pressure actually declines initially as the molecules begin to align in the flow, and then increases sharply through the coil-stretch transition. At low concentrations and at low strain rate, the polymer molecules are in a coil configuration, and intraparticle spring repulsions are the chief contributor to the extra pressure. As the strain rate increases, the molecule begins to untangle into a linearly oriented strand before the average spring length begins to increase. It is during this phase, when the molecules are oriented but the springs are not stretched that we observe a minimum in the extra pressure with a θ-solvent. At higher concentrations, the importance of intramolecular spring repulsions is less, and the effect is not observed.

5.4.3 Steady Shear Flow Experiments

Steady homogeneous shear flow is a unidirectional flow where ∇v is given by

$$\nabla v = \begin{pmatrix} 0 & \dot{\gamma} & 0 \\ 0 & 0 & 0 \\ 0 & 0 & 0 \end{pmatrix} \tag{5.16}$$

and the velocity field is defined as $v_x = \dot{\gamma} y$. The flow is modeled in a 3D periodic domain with Lees-Edwards boundary conditions to enforce the velocity at the boundary. As compared to planar elongational flow, the deformation of polymer molecules occurs much more gradually in shear flow. There is no sharp transitional period comparable to the coil-stretch transition, so while a much larger range of Deborah numbers must be simulated to see the interesting dynamics, there is no need for the fine gradations employed in

PEF. We simulate Deborah numbers ranging from approximately 0.1 to roughly 300, which covers the full range of molecular extensions, from a coil to the elongated tumbling stage. The same set of concentrations and solvent qualities are investigated as in the PEF experiments.

Due to the need to sample a larger range of shear rates, the steady shear flow simulations have been carried out using two values of Γ. For low De, $\Gamma = 5$ as was the case for the planar elongational flow. In order to access larger De, a second set of simulations have been carried out with $\Gamma = 50$. The ten-fold increase in the solvent viscosity allows us to sample an extra decade of Deborah numbers. Where the two series overlap, the data from both is plotted.

Extension

In shear flow, we find that the most faithful representation of polymer extension is the radius of gyration, as that metric better captures the overall molecular size as the molecules align and tumble in the shear flow. The molecular extension in shear flow is much more gradual than in elongational flow. Once again we will present the results in two ways; scaled first by the individual Deborah number of the solution, with $\mathrm{De} = \dot{\gamma}\lambda$ where λ is the longest relaxation time of the molecules at the given concentration, and by $\mathrm{De}_{0.5}$, the Deborah number of the lowest concentration, so that all concentrations may be compared at identical absolute rates of strain. Figure 5-27 presents the radius of gyration vs. De for the θ-solvent case. For all concentrations, a softer S-shaped curve is followed as compared to planar elongational flow, as the molecules transition from a near-equilibrium coil to a more fully elongated shape. At low shear rates, all the curves are identical, as is to be expected, as there is little concentration dependency in the equilibrium coil size with a θ-solvent. As the molecules elongate, we note that a lower concentration leads to earlier elongation in the middle range of Deborah numbers, after which all the curves fall back onto each other at high De. Figure 5-28 shows the radius of gyration data for the same simulations, this time plotted against $\mathrm{De}_{0.5}$. Once again we note that there

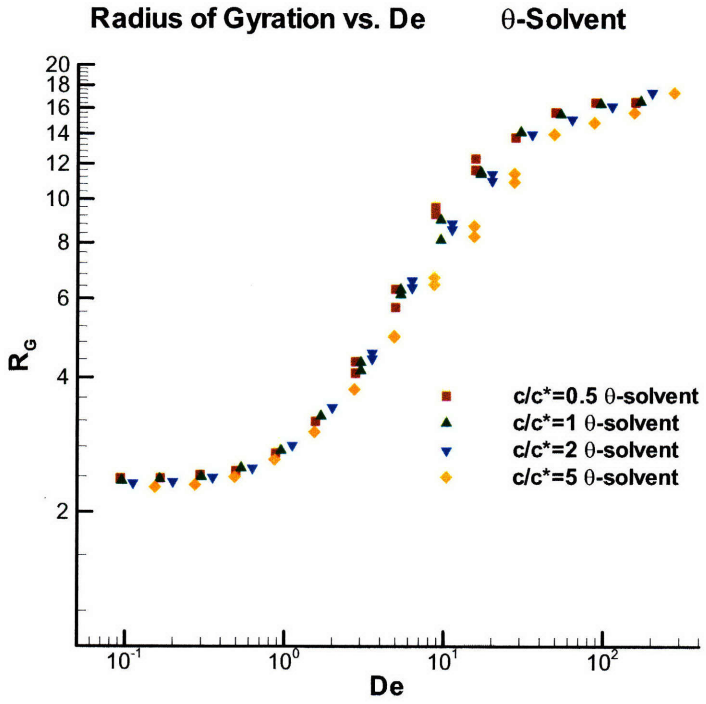

Figure 5-27: Radius of gyration vs. De in a θ-solvent

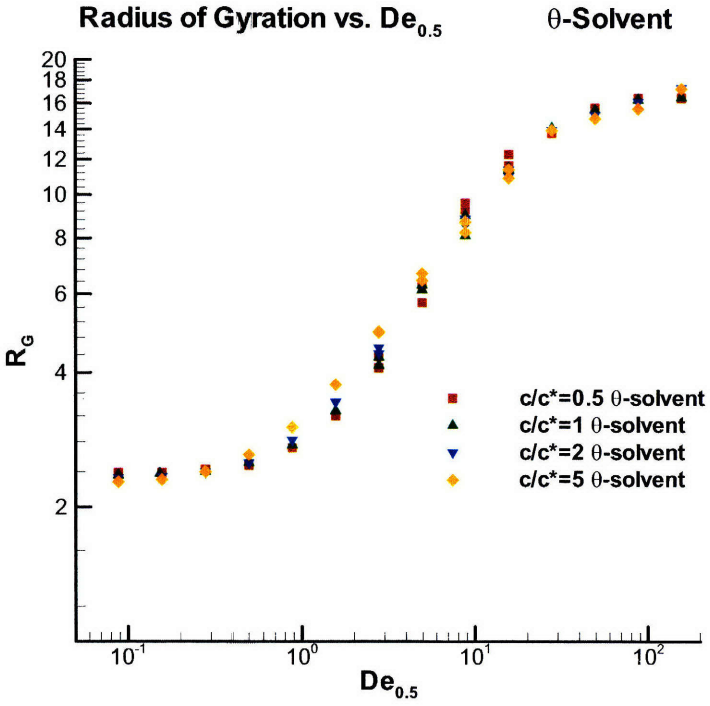

Figure 5-28: Radius of gyration vs. $De_{0.5}$ in a θ-solvent

is agreement between the different concentrations at low and high strain rate. In this view however, we note that in the middle range of $De_{0.5}$, at higher concentrations, the molecules are shown to elongate at slightly lower absolute strain rates. Thus we see that the elevated relaxation time of the higher concentration leads to a modest increase in the rate at which elongation of the molecules occurs, but which is slower than is predicted. Figures 5-29 and 5-30 show the molecular size profiles for the good solvent case.

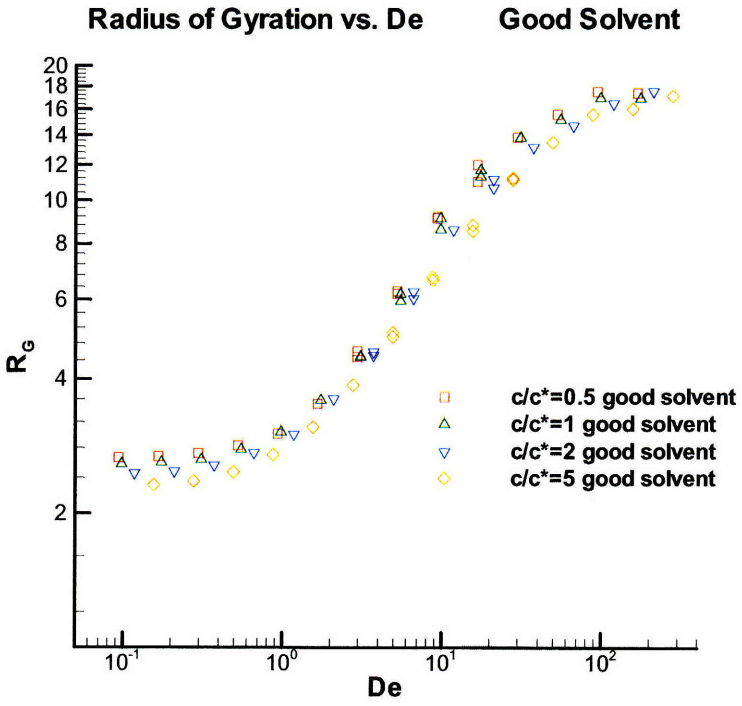

Figure 5-29: Radius of Gyration vs. De in a good solvent

At low rates of strain, there is a concentration dependence on the molecular size which follows the equilibrium case. Like in the θ-solvent, the elongation in the middle range of strain rates occurs faster for greater concentrations, though the effect is less than that which would be predicted by the measured relaxation time of the solutions. In Figures 5-31 through 5-34 the radius of gyration as a function of solvent quality is compared

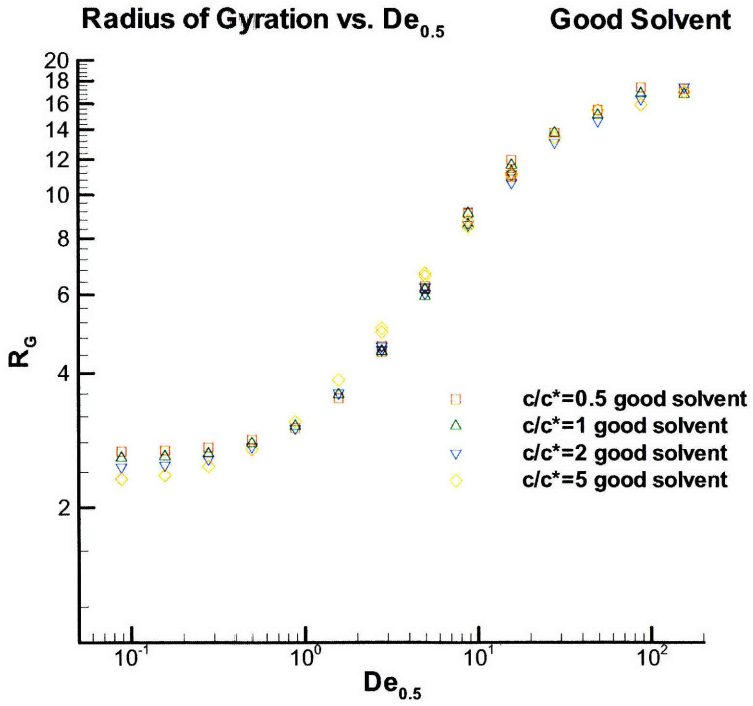

Figure 5-30: Radius of gyration vs. $De_{0.5}$ in a good solvent

for each concentration. Across all concentrations studied, the good solvent produces a larger radius of gyration until the molecules begin to elongate between De = 1 and De = 10, at which point the solvent quality ceases to play an important role in determining the extension. The increased intramolecular excluded volume effect of the good solvent which is responsible for the larger coil size at equilibrium loses its effect as the molecules are elongated in the shear flow.

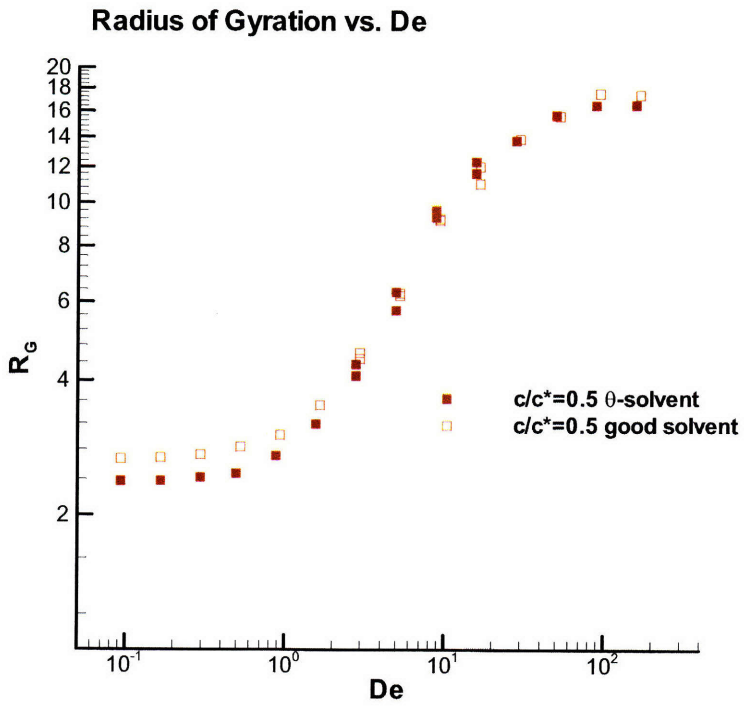

Figure 5-31: Radius of Gyration vs. De for good and θ-solvents at $c/c* = 0.5$

Viscosity

In Figures 5-35 and 5-36 the polymer contribution to the viscosity in a θ-solvent is presented vs. De and $De_{0.5}$ respectively. The viscosity is scaled by $c*/c$ to eliminate the linear dependence of viscosity on concentration. As the concentration is increased, the

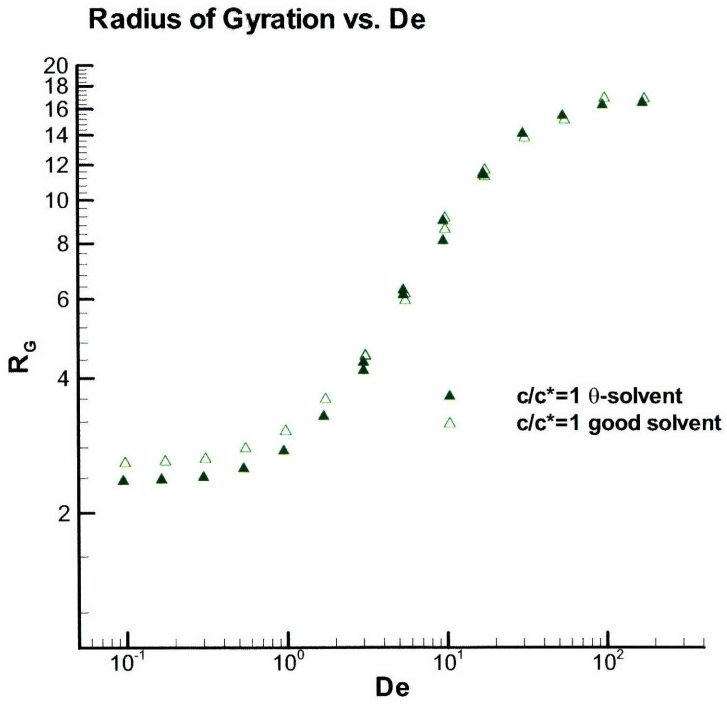

Figure 5-32: Radius of Gyration vs. De for good and θ-solvents at $c/c* = 1$

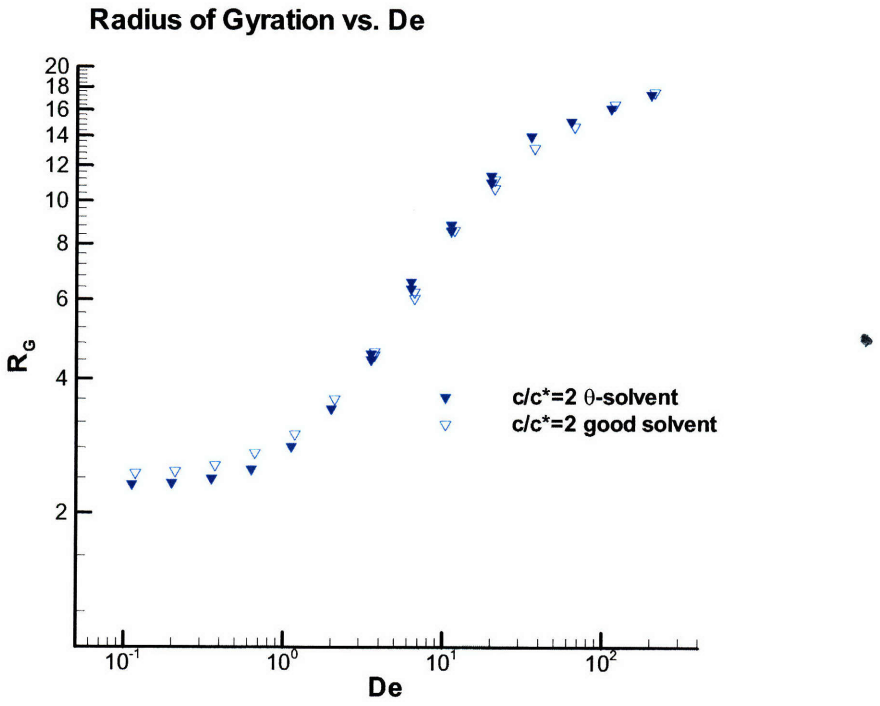

Figure 5-33: Radius of Gyration vs. De for good and θ-solvents at $c/c* = 2$

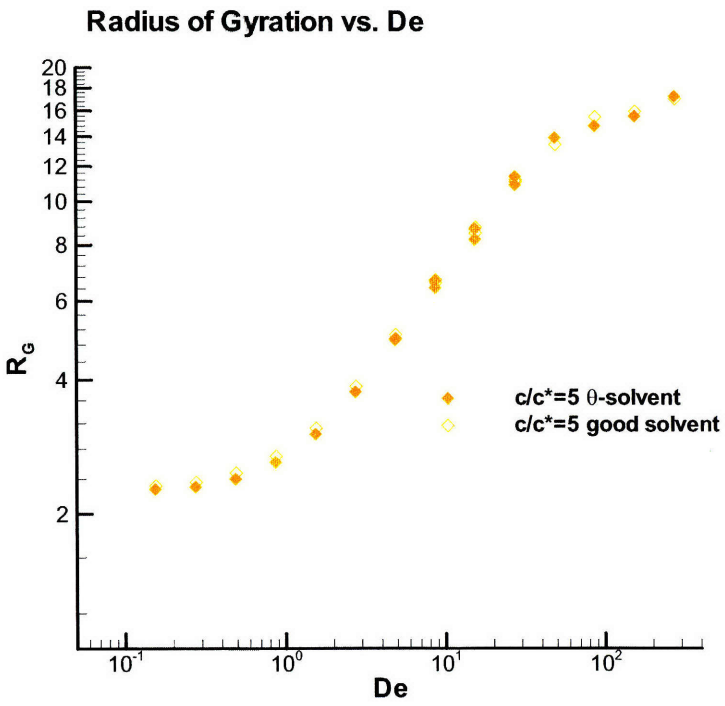

Figure 5-34: Radius of Gyration vs. De for good and θ-solvents at $c/c* = 5$

zero-shear-rate viscosity increases. This effect is consistent with the results of Stoltz *et al.*[76].

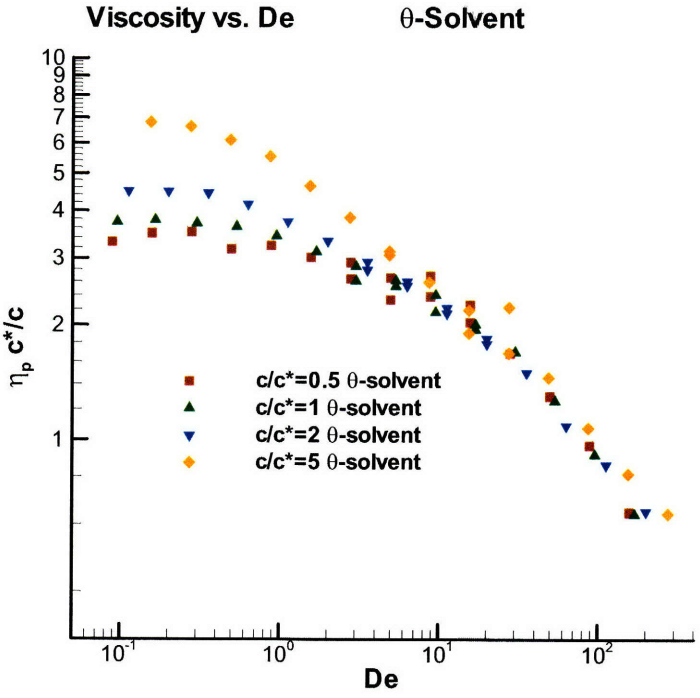

Figure 5-35: Polymer contribution to the viscosity vs. De in a θ-solvent

Figures 5-37 and 5-38 show the shear dependent behavior of the polymer viscosity in a good solvent. Once again, this data is presented once as a function of De, and once as a function of $De_{0.5}$. As in the θ-solvent case, the zero-shear-rate viscosity increases with concentration. There is, however, a secondary effect at work which reduces the magnitude of the increase. A larger coil, which is present in the good solvent at lower concentration, causes an increase in the zero-shear-rate viscosity, as can be seen to varying degrees in Figures 5-39 through 5-42, in which the viscosity of the good and θ-solvent solutions are compared for each concentration. Because the good solvent experiences a decrease in coil size as concentration increases, this has the opposite effect, tending to decrease the

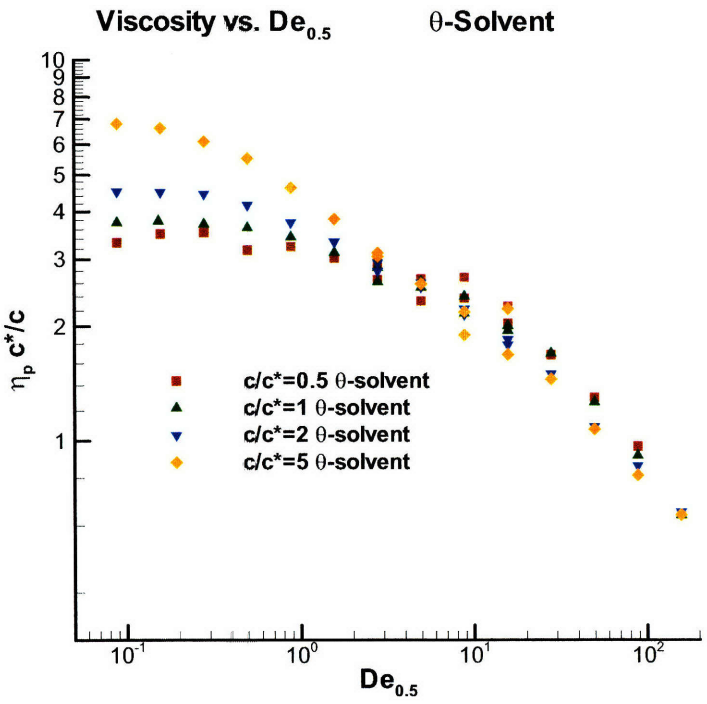

Figure 5-36: Polymer contribution to the viscosity vs. $De_{0.5}$ in a θ-solvent

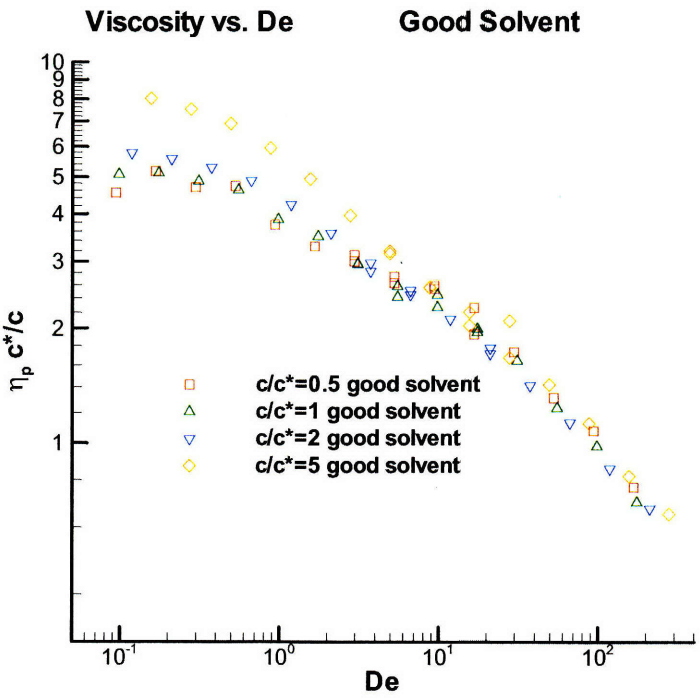

Figure 5-37: Polymer contribution to the viscosity vs. De in a good solvent

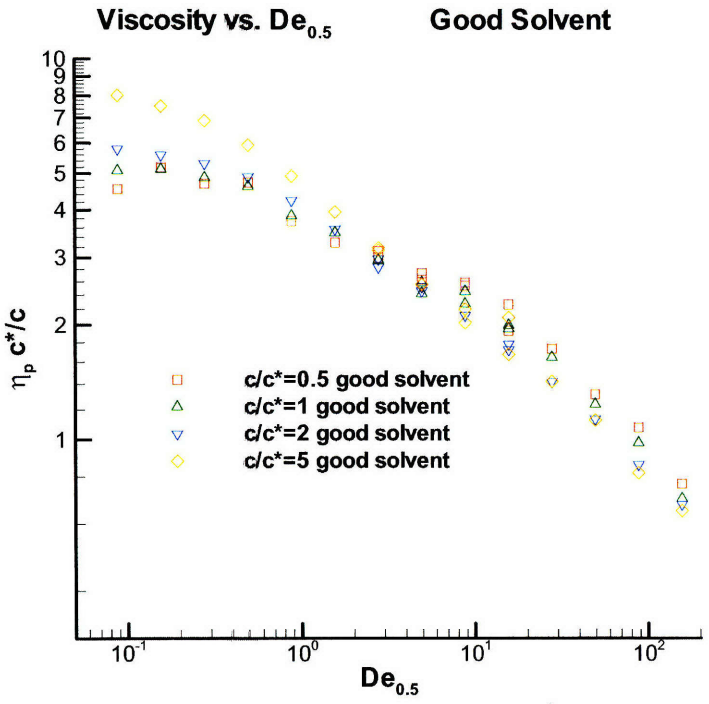

Figure 5-38: Polymer contribution to the viscosity vs. $De_{0.5}$ in a good solvent.

viscosity as the concentration increases.

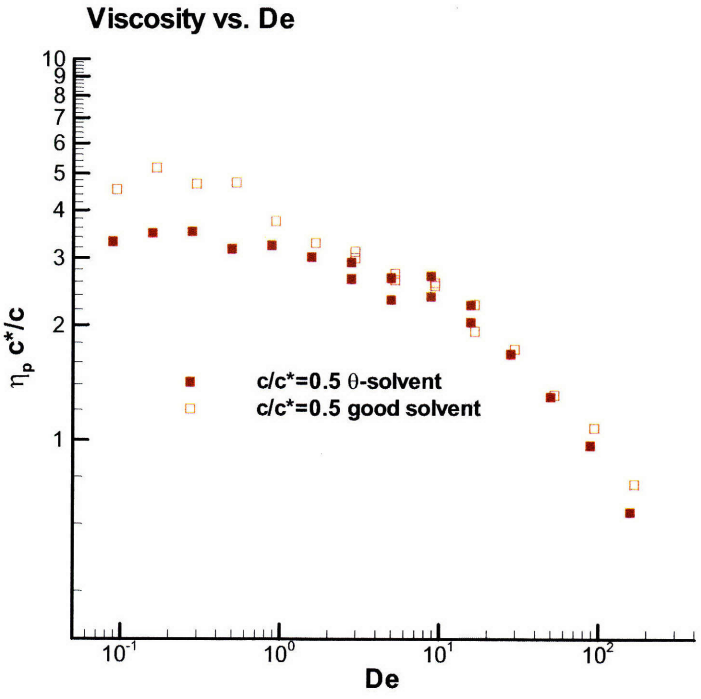

Figure 5-39: Polymer contribution to the viscosity vs. De for good and θ-solvents at $c/c* = 0.5$

First Normal Stress Coefficient

In Figures 5-43 and 5-44 the first normal stress coefficient for the θ-solvent is shown. Figures 5-45 and 5-46 give the same for the good solvent. As was the case for the viscosity, the results are scaled by $c*/c$ to remove the linear dependence on concentration. Encouragingly, Ψ_1 shows the expected qualitative behavior, with a relatively constant zero-shear-rate value, which transitions into strong shear-thinning at an approximate shear rate of De = 1. Much like the viscosity results, in both solvent qualities there is a clear zero-shear-rate dependence of the first normal stress coefficient on concentration. When examined as a function of De, the dependence continues throughout the range of

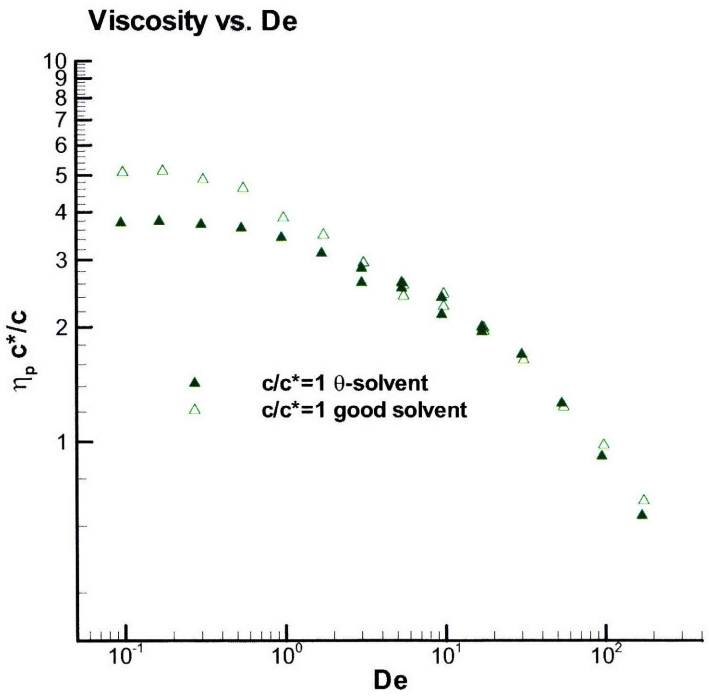

Figure 5-40: Polymer contribution to the viscosity vs. De for good and θ-solvents at $c/c* = 1$

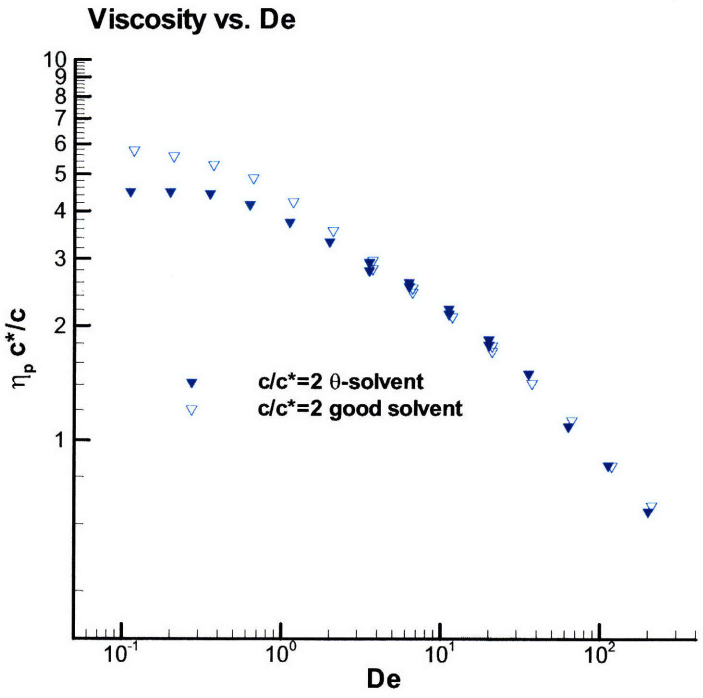

Figure 5-41: Polymer contribution to the viscosity vs. De for good and θ-solvents at $c/c* = 2$

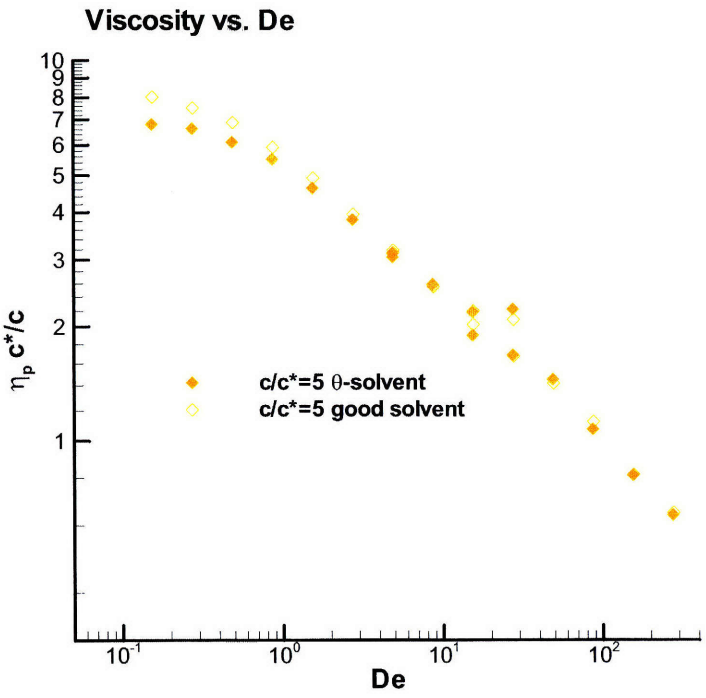

Figure 5-42: Polymer contribution to the viscosity vs. De for good and θ-solvents at $c/c* = 5$

shear rates studied. When plotted as a function of a constant shear rate, however, the data for each concentration collapses onto a single power-law curve.

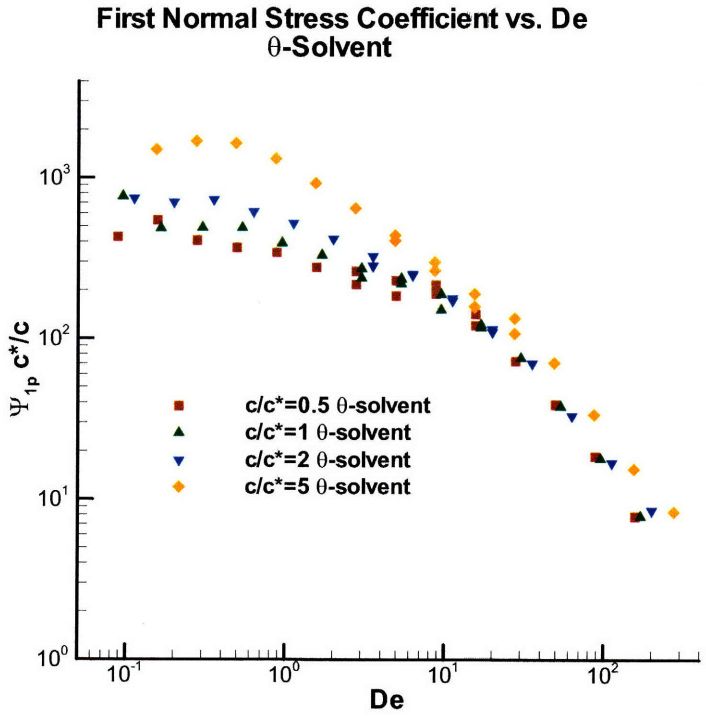

Figure 5-43: The first normal stress coefficient vs. De in a θ-solvent.

Figures 5-47 through 5-50 show the first normal stress coefficient vs. De for the two solvent qualities at each individual concentration, to highlight the effect of solvent quality. In the zero-shear-rate range, the good solvent shows a consistently larger first normal stress coefficient, but as the Deborah number increases, and the importance of intramolecular excluded volume interactions become less important, the difference between the two solvent qualities diminishes. The first normal stress coefficient is quite susceptible to noise error, as is evidenced by the less-than-perfect smoothness of the curves

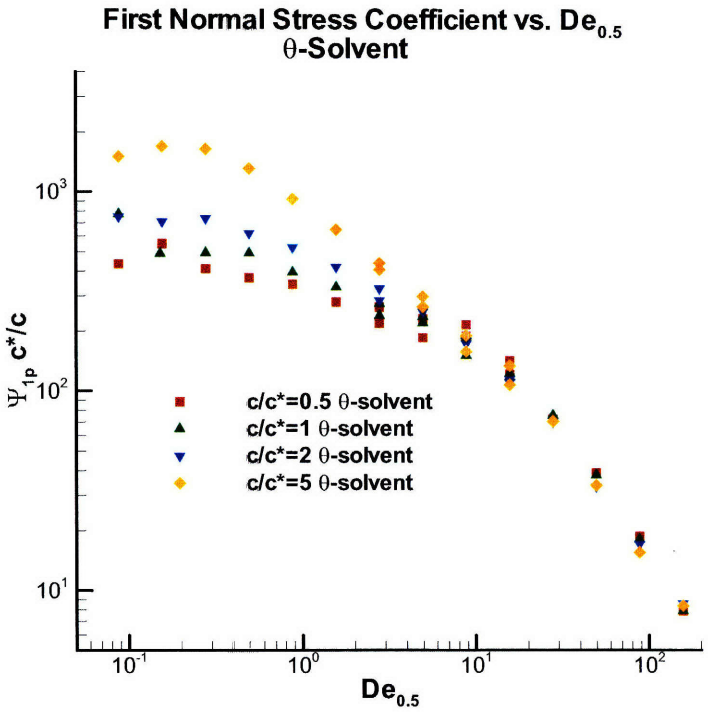

Figure 5-44: The first normal stress coefficient vs. $De_{0.5}$ in a θ-solvent.

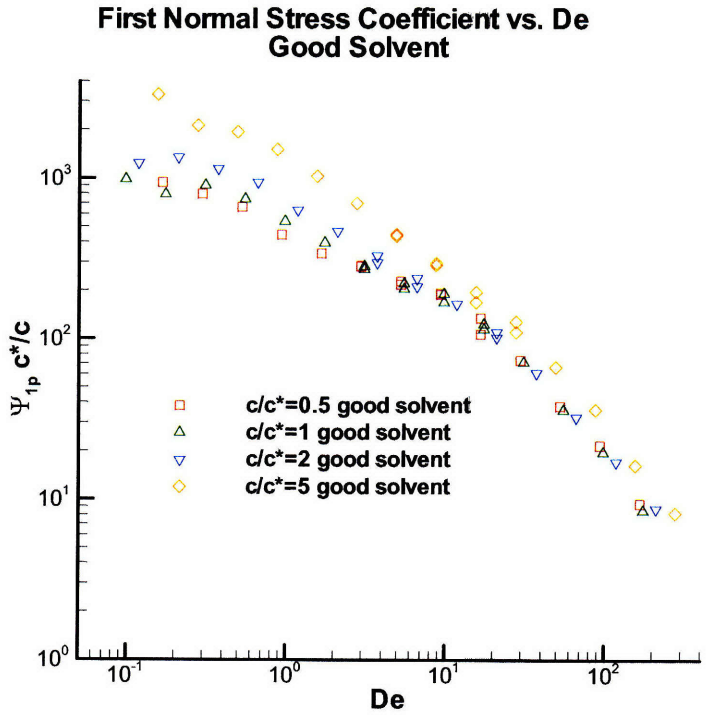

Figure 5-45: First normal stress coefficient vs. De in a good solvent.

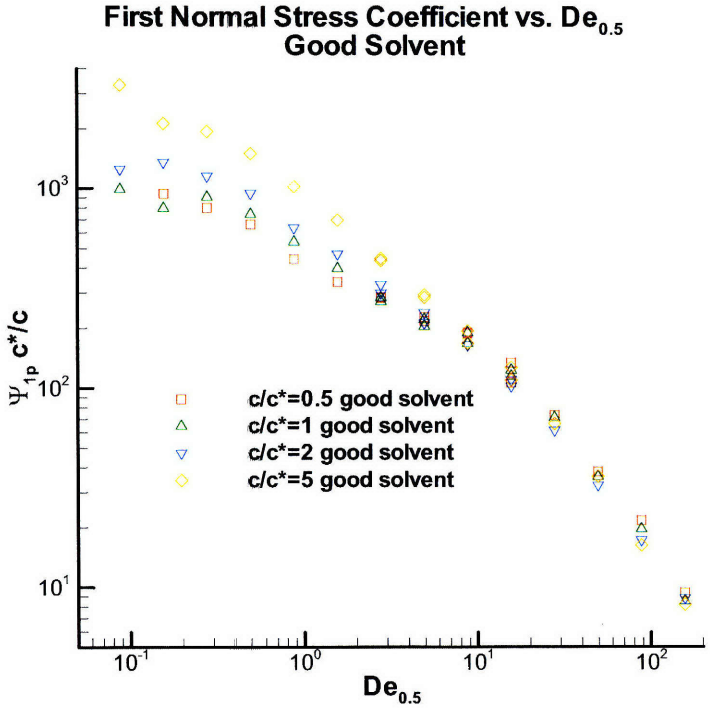

Figure 5-46: First normal stress coefficient vs. $De_{0.5}$ in a good solvent.

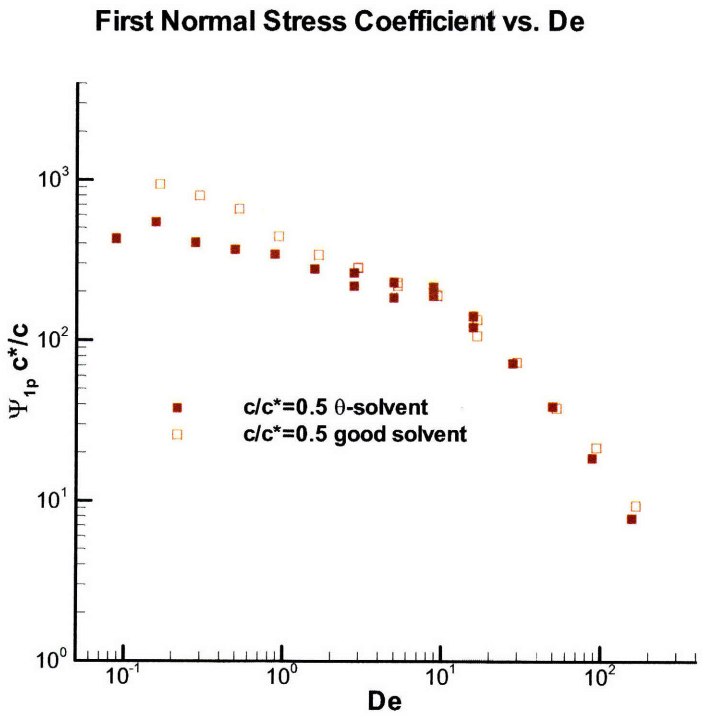

Figure 5-47: First normal stress coefficient vs. De for good and θ-solvents at $c/c* = 0.5$

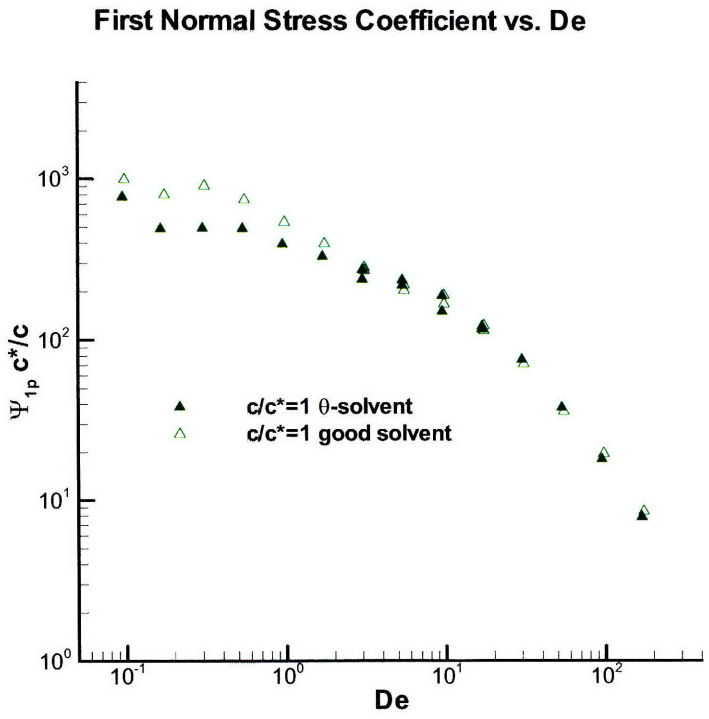

Figure 5-48: First normal stress coefficient vs. De for good and θ-solvents at $c/c* = 1$

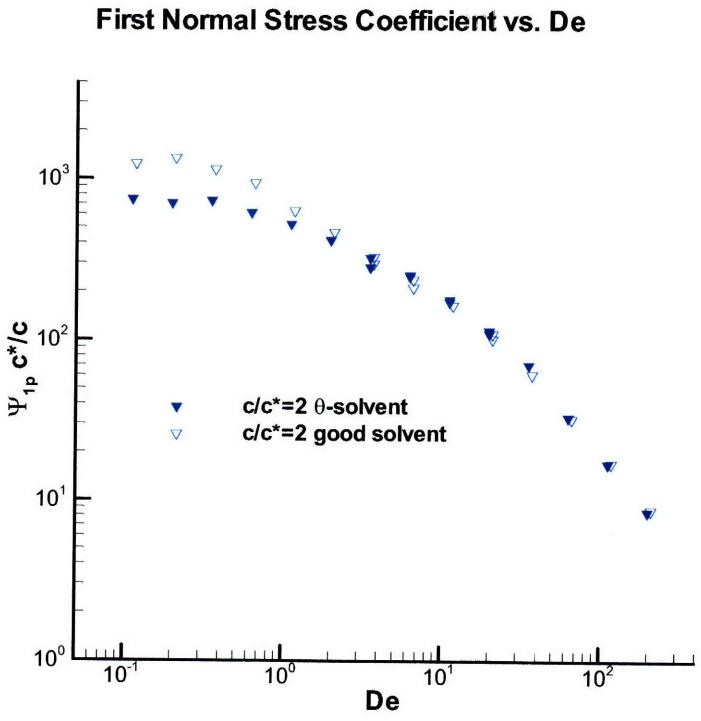

Figure 5-49: First normal stress coefficient vs. De for good and θ-solvents at $c/c* = 2$

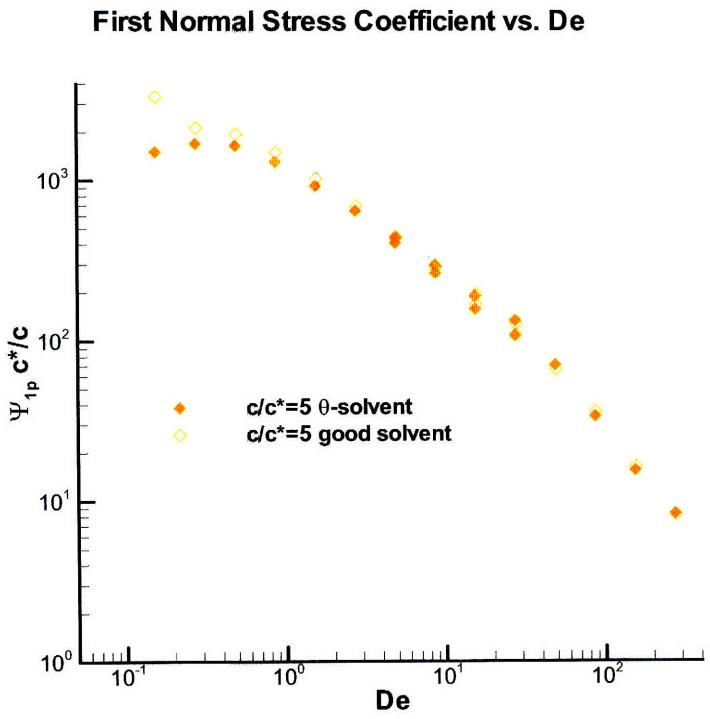

Figure 5-50: First normal stress coefficient vs. De for good and θ-solvents at $c/c* = 5$

5.4.4 Discussion

There are several key themes that come out of the shear flow results which find themselves repeated in different forms throughout the material function and configurational results. Primarily, we contrast the importance of the relaxation time in shear and elongational flows. In planar elongational flow, plotting the molecular extension and viscosity against De produces very good agreement between the different concentrations, with a coil-stretch transition occurring at the predicted value of De = 0.5. When this data is plotted as a function of a constant strain rate, $De_{0.5}$, however, one can see clearly the importance of the relaxation time dependence on concentration, as each concentration undergoes the coil-stretch transition at a different absolute strain rate. It is clear that the dynamic results in planar elongational flow depend on the relaxation rate of the solution as a whole, much more than the relaxation rate of a single molecule in isolation. In the shear flow results, however, this dichotomy is not as clear. Both the radius of gyration and first normal stress coefficient are dominated by the flow-direction stretch of the molecules, and these quantities are most successfully plotted against $De_{0.5}$. This suggests that the intermolecular interactions that cause a larger relaxation time at higher concentration are not that important in determining the flow-direction extension in steady shear flow. The viscosity, on the other hand, is much more successfully plotted against De, which does take into account the differences in relaxation time. We conclude that in the shear-thinning region, interactions between particles are important in determining macromolecular alignment, but are less important in governing the degree of stretch experienced by each bead-spring chain. The transition between the zero-shear-rate regime and the shear-thinning regime is much more gradual, and occurs over a larger range of the Deborah number than does the coil-stretch transition in planar elongational flow. As a result, the strain rate at which transitions begin are more difficult to specify in shear flow.

The necessity of using multiple values of Γ in order to access the entire range of interesting De for shear flow must be viewed as a liability for DPD, as it is difficult to

match the overlapping data perfectly, and adds uncertainty to the conclusions that can be made. We note that planar elongational flow does not suffer from this difficulty, as the entire range of interesting strain rates is accessible using a single value of Γ.

We also note the importance of the equilibrium coil size on the zero-shear-rate results. In the good solvent, where the concentration has a strong effect on the coil size, a larger radius of gyration, viscosity and first normal stress coefficient were observed in shear flow as compared to the θ-solvent. This effect becomes smaller as the concentration increases. Similarly, the fractional extension and and elongational viscosity at low elongation rates showed the same general trend in the elongational flow case.

In interpreting our results, we look to compare qualitatively to the work of Stoltz *et al.*[76], who have performed Brownian dynamics simulations in the semi-dilute regime of steady shear and planar elongational flows of λ-DNA molecules. The work is restricted to a good solvent, but includes simulations with and without hydrodynamic interaction. We are in agreement with this work in predicting an equilibrium coil size which decreases with increasing concentration, as well as an increase in the relaxation time of more concentrated solutions. The concentration-dependence of the zero-shear-rate viscosity in shear flow is predicted by both methods as well. When HI is included in the Brownian dynamics simulations, the elongational viscosity at large De in planar elongational flow increases dramatically with the concentration while the fractional extension is relatively unchanged. This effect disappears when HI is not included in their model. The DPD results do not show this concentration dependence, which suggests that the HI effects which come about naturally in DPD do not capture this phenomenon.

5.5 Conclusion

In this chapter, a demonstration of the rheological modeling capabilities of DPD has been presented. A linear bead-spring chain model of a flexible polymer was subjected to steady shear and planar elongational flow at concentrations throughout the semi-dilute

range. The conservative force coefficient was varied to reproduce both good and θ-solvent conditions. A spring-spring repulsion force has been introduced into the DPD polymer model in order to prevent springs from passing through each other, allowing the model to reproduce concentration dependent effects.

At equilibrium, the radius of gyration of the polymer coil was shown to depend on both the solvent quality and the polymer concentration. At low concentration, the polymer coil size is much larger in the good solvent than in the θ-solvent. As the concentration is increased, however, the coil size in the good solvent decreases. The polymer coil size in the θ-solvent is much less sensitive to the concentration.

As concentration is increased, the relaxation time of the solution increases for both solvent qualities. The presence of other molecules hinders relaxation from a stretched shape. This result is in accord with previous studies of concentration-dependence of polymers in the semi-dilute range.

In planar elongational flow, a sharp coil-stretch transition was observed to occur at the theoretically predicted strain rate of $\mathrm{De} = 0.5$. This is reflected in both the molecular extension and the elongational viscosity. This result is significant, as it represents the first use of DPD to simulate an elongational flow. The results presented here thus serve as a confirmation of DPD's ability to reproduce correct polymeric rheology, as well as a demonstration of the appropriateness of applying the Kraynik and Reinelt boundary conditions to the DPD system.

In shear flow, the results were more mixed. Encouragingly, the viscosity, first normal stress coefficient, and radius of gyration all showed correct qualitative rheological behavior. The material functions were constant at low shear rates, transitioning to a shear thinning regime obeying a power-law at $\mathrm{De} = 1$. The radius of gyration is constant at low shear rates, goes through a sharp increase, and finally levels off at very high shear rates. A clear concentration dependence of the zero-shear-rate viscosity was demonstrated for both solvent qualities, in agreement with previous work, with the viscosity increasing with concentration. In the good solvent, this effect is tempered by an opposite tendency

due to the larger coil size at lower concentration.

In the shear-thinning regime, the effect of the concentration was shown to apply primarily to the viscosity, as the shear-thinning curves at disparate concentrations fall onto a single curve when plotted against the Deborah number. The first normal stress coefficient and radius of gyration on the other hand fall on a single curve when plotted against a constant strain rate, $De_{0.5}$, indicating that the concentration does not have a significant effect on these properties.

In both types of flow, the importance of the spring-spring repulsion force was demonstrated by tracking the pressure added to the system due to it. Spring repulsions are more common in the θ-solvent, because the excluded volume interaction present in the good solvent prevents springs from approaching each other in many cases. Contra Stoltz el al., however, we found that the EV interaction does not reduce spring crossing events sufficiently so that the spring repulsion interaction may be removed from the model. As the concentration increases, the number and importance of spring-spring interactions increases for both solvent qualities.

Having found the linear spring repulsion force law to be insufficient, we were forced to use a more computationally demanding exponential force law instead. While calculation of the spring-spring interaction is no more computationally demanding with the exponential law, stability constraints required us to reduce the timestep used, and to limit the maximum spring length used in our bead-spring chains. Stochastic error is a significant problem in these calculations, particularly at low strain rates, where the measured stresses are very small. The cost of including the spring repulsion interaction limits the length of time which can be sampled.

Thus, while we note that the agreement with both expected rheological results generally, and with the specific semi-dilute concentration dependence reported by Stoltz *et al.* is encouraging, and speaks to DPD's ability to produce correct rheological behavior in polymer systems, the sheer computational requirements for reaching these results counsels against the use of DPD as a tool for systems as simple as the one presented here.

In other words, when Brownian dynamics is available as an alternate method, it will likely always hold a significant computational cost advantage over DPD. Nonetheless, the extensive flexibility in molecular architecture and chemistry available to DPD makes it attractive to use for modeling more complicated molecules and systems. Having shown that the rheological predictions made by DPD are quite reliable, such systems can be simulated with more confidence.

Chapter 6

Summary

In this thesis, the utility of the Dissipative Particle Dynamics method for rheological studies of polymers is explored through non-equilibrium simulations of steady shear and planar elongational flow. Special attention has been paid to the implementation details of simulating non-equilibrium flows in domains of limited size. The application of the Kraynik and Reinelt boundary conditions to DPD to simulate planar elongational flow has not been previously demonstrated, and represents a new use for DPD. The material functions of DPD polymer solutions are calculated as a function of strain rate, showing that DPD is capable of reproducing correct rheological behavior over a large range of shear and elongation rates.

6.1 Dilute FENE Dumbbells

In Chapter 4, DPD was used to simulate as faithfully as possible a dilute solution of FENE dumbbells. The purpose of the exercise was to show that the scaled material function results of FENE dumbbells undergoing shear and planar elongational flow are in quantitative agreement with the predictions of Brownian dynamics, a simulation method which is well-studied and widely accepted. Due to computational cost restraints, the condition of dilution in DPD is approximated by using a θ-solvent and "phantom" springs,

which can pass through one another freely. All DPD dumbbells were simulated with a constant extensibility parameter, $b = 50$, to allow for comparison to a single set of BD results. The ratio of the maximum extension length of the dumbbell to the DPD particle interaction length was varied, which in turn varied the degree of coarse-graining in DPD. For the longest dumbbells, corresponding to the finest-grained DPD, excellent agreement was found between DPD and BD in the shear viscosity, first normal stress coefficient, and elongational viscosity. As the molecules were shorted, two discrepancies arose. At low shear rates, elevated viscosity and first normal stress coefficient were observed. This effect is a result of the excluded volume interaction produced by the repulsive interaction of the dumbbell's end-beads when the length is less than the DPD interaction distance. At high shear rates, shorter dumbbells exhibited faster shear-thinning of the material functions than is predicted by BD. I showed that this result is in qualitative agreement with the predictions of the Giesekus anisotropic drag model for hydrodynamic interaction.

6.2 Semidilute Solutions of Bead-Spring Chains

Chapter 5 explored the shear and elongational rheology of longer $N = 20$ bead-spring chain molecules. In order to include the effects of concentration on the rheology, an additional component was added to the DPD model to prevent springs from passing through each other. Specifically, a repulsive force law with an exponential weighting function was added between springs. Solvent quality was also varied by changing the strength of the conservative bead-bead repulsion force between solvent and polymer DPD particles. The solvent quality and concentration dependence of the polymer material functions were reported for steady shear and planar elongational flow. At equilibrium, the coil size of polymers in a good solvent was shown to be strongly concentration dependent, decreasing as concentration increased and the coils impinged upon each other. The effect was observed, but found to be much weaker in a θ-solvent.

The relaxation time of the solution increased with concentration for both solvent

qualities. This leads to two scalings of the strain rate. The Deborah number is calculated for each individual solution based on the relaxation time measured. Alternatively, the solutions can be compared on the basis of a constant absolute shear rate. In planar elongational flow, a sharp coil-stretch transition was observed to occur at $De = 0.5$, for each solution, in accordance with theoretical predictions. From this, we note that the dynamics of elongational flow is predicted quite successfully by the measured relaxation rates, as opposed to the absolute strain rate. The same cannot be said for shear flow, which shows some dependence on the Deborah number, and some on the absolute shear rate. The viscosity shows behavior consistent with different relaxation rates for different concentrations, while the first normal stress coefficient and radius of gyration behavior appears to depend only on the relaxation rate of an individual molecule. At low strain rates, the viscosity increased with concentration. This effect was mitigated in the good solvent by the tendency of the coils to be larger at low concentration, as larger coils lead to greater viscosity.

6.3 Conclusions

- For rheological investigations of polymers, the Lowe-Anderson formulation of DPD is vastly superior to the original incarnation which includes the explicit dissipative and random forces. Original DPD is much more restricted in the range of Schmidt number that can be simulated. Stability considerations dictate the value of the random force coefficient, and there is very little flexibility available to the modeler. I have been able to find no substantive difference between the results of the two methods at low Schmidt numbers. The variety of polymer molecules which can be built in DPD is almost limitless, and represents an enormous spread of relaxation times. Because DPD is naturally restricted in the strain rates at which simulation can be performed efficiently, the ability of LA-DPD to simulate different simple fluid viscosities is very important.

- Due to the high cost of performing DPD simulations, it is frequently important to limit the simulation box size as much as possible. I have shown that long molecules may be simulated using a domain which is smaller than the total contour length of the molecule. In this thesis, the box size has been defined most often by the requirement that the domain be twice the maximum spring extension in any direction. While I have not performed systematic studies to determine the importance of box-size effects, I have not detected any box-size dependent behavior in my rheology studies. It is possible that the soft interparticle interaction that characterizes DPD leads to rapid damping out of perturbations, minimizing the domain size requirements.

- The concentration of polymer which can realistically be simulated with DPD is limited by a number of factors. First, the number density of DPD particles is small compared to other methods, reflective of the fact that each DPD particle represents a large collection of solvent or monomer units. Even when every DPD particle is a part of a polymer molecule, only a small multiple of the overlap concentration is achieved. Second, concentration-dependent behavior requires the inclusion of a spring-spring repulsion interaction. Calculating the closest approach distance between one-dimensional objects such as springs is much more computationally demanding than finding distances between points. At high polymer concentrations, the spring-spring repulsion algorithm becomes the limiting computational step in the DPD method. This problem is shared by Brownian dynamics as well.

- The effect of excluded volume in DPD has been clearly demonstrated in the dumbbell results of Chapter 4. Depending on the length scale chosen by the modeler, the effect can be quite strong, or almost non-existent. The polymer length scale has a very powerful effect on the simulation cost, however, so the modeler may not always be free to change the polymer length scale to suit his needs. The effect of hydrodynamic interaction is much more difficult to establish clearly. I have shown

that the faster shear-thinning of shorter dumbbells is in qualitative agreement with the Giesekus anisotropic drag model, but quantitative measures of the effect of HI are difficult to obtain, due to the presence of EV. Like EV, the importance of HI in DPD is tunable by varying the polymer length scale. There is no way to separate these two effects, which must be considered a weakness of the DPD method.

- Stochastic error is a significant problem in DPD, particularly when examining the low-shear-rate behavior of polymer molecules with long relaxation times such as those studied in Chapter 5. In comparison to Brownian dynamics, the cost of simulating the solvent explicitly in DPD makes the method much less attractive for systematic rheology studies. The method is tremendously flexible for building polymer molecules, including architecture, chemistry, and solvent quality, but is quite inflexible with regard to other issues such as the inclusion of, and the degree of importance of HI and EV. It is important to show that DPD produces qualitatively correct rheology for a verifiable case such as FENE dumbbells, because DPD is best used to simulate unverifiable cases, which are not amenable to simulation with other methods.

Bibliography

[1] Allen, M. P. and D. J. Tildesley. *Computer Simulation of Liquids*. Oxford, 1987.

[2] Andersen, H. C. "Molecular-Dynamics Simulations at Constant Pressure And-Or Temperature," *Journal of Chemical Physics*, *72*(4):2384–2393 (1980).

[3] Avalos, J. B. and A. D. Mackie. "Dissipative particle dynamics with energy conservation," *Europhysics Letters*, *40*(2):141–146 (OCT 15 1997).

[4] Avalos, J. B. and A. D. Mackie. "Dynamic and transport properties of dissipative particle dynamics with energy conservation," *Journal of Chemical Physics*, *111*(11):5267–5276 (SEP 15 1999).

[5] Backer, J. A., et al. "Combined length scales in dissipative particle dynamics," *Journal of Chemical Physics*, *123*(11):114905 (SEP 15 2005).

[6] Backer, J. A., et al. "Poiseuille flow to measure the viscosity of particle model fluids," *Journal of Chemical Physics*, *122*(15):154503 (APR 15 2005).

[7] Benzi, R., et al. "The Lattice Boltzmann-Equation - Theory and Applications," *Physics Reports-Review Section of Physics Letters*, *222*(3):145–197 (DEC 1992).

[8] Bird, R. B., et al. *Dynamics of Polymeric Liquids, Volume 2 Kinetic Theory*. Wiley, 1987.

[9] Boek, E. S., et al. "Computer simulation of rheological phenomena in dense colloidal suspensions with dissipative particle dynamics," *Journal of Physics-Condensed Matter*, *8*(47):9509–9512 (NOV 18 1996).

[10] Boek, E. S., et al. "Simulating the rheology of dense colloidal suspensions using dissipative particle dynamics," *Physical Review E*, *55*(3):3124–3133 (MAR 1997).

[11] Boek, E. S. and P. van der Schoot. "Resolution effects in Dissipative Particle Dynamics simulations," *International Journal of Modern Physics C*, *9*(8):1307–1318 (DEC 1998).

[12] Cao, X. R., et al. "Aggregation of poly(ethylene oxide)-poly(propylene oxide) block copolymers in aqueous solution: DPD simulation study," *Journal of Physical Chemistry a*, *109*(45):10418–10423 (NOV 17 2005).

[13] Chen, S., et al. "Flow around spheres by dissipative particle dynamics," *Physics of Fluids*, *18*(10):103605 (OCT 2006).

[14] Coveney, P. V. and P. Espanol. "Dissipative particle dynamics for interacting multicomponent systems," *Journal of Physics A-Mathematical and General*, *30*(3):779–784 (FEB 7 1997).

[15] Coveney, P. V. and K. E. Novik. "Computer simulations of domain growth and phase separation in two-dimensional binary immiscible fluids using dissipative particle dynamics," *Physical Review E*, *54*(5):5134–5141 (NOV 1996).

[16] Cupelli, C., et al. "Dynamic capillary wetting studied with dissipative particle dynamics," *New Journal of Physics*, *10*:043009 (APR 10 2008).

[17] Duong-Hong, D., et al. "An implementation of no-slip boundary conditions in DPD," *Computational Mechanics*, *35*(1):24–29 (DEC 2004).

[18] Espanol, P. "Dissipative particle dynamics with energy conservation," *Europhysics Letters*, *40*(6):631–636 (DEC 15 1997).

[19] Espanol, P., et al. "Coarse-graining of a fluid and its relation with dissipative particle dynamics and smoothed particle dynamics," *International Journal of Modern Physics C*, *8*(4):899–908 (AUG 1997).

[20] Espanol, P. and P. Warren. "Statistical-Mechanics of Dissipative Particle Dynamics," *Europhysics Letters*, *30*(4):191–196 (MAY 1 1995).

[21] Evans, D. J. and G. P. Morriss. "Statistical Mechanics of Nonequilibrium Liquids," (1990).

[22] Fabritiis, G. D. De, et al. "Multiscale dissipative particle dynamics," *Philosophical Transactions of the Royal Society of London Series A-Mathematical Physical and Engineering Sciences*, *360*(1792):317–331 (MAR 15 2002).

[23] Fabritiis, G. De and P. V. Coveney. "Dynamical geometry for multiscale dissipative particle dynamics," *Computer Physics Communications*, *153*(2):209–226 (JUN 15 2003).

[24] Fan, X. J. "Viscosity, 1st Normal-Stress Coefficient, and Molecular Stretching in Dilute Polymer-Solutions," *Journal of Non-Newtonian Fluid Mechanics*, *17*(2):125–144 (1985).

[25] Fan, X. J., et al. "Simulating flow of DNA suspension using dissipative particle dynamics," *Physics of Fluids*, *18*(6):063102 (JUN 2006).

[26] Fan, X. J., et al. "Microchannel flow of a macromolecular suspension," *Physics of Fluids*, *15*(1):11–21 (JAN 2003).

[27] Fedosov, D. A., et al. "Dissipative particle dynamics simulation of depletion layer and polymer migration in micro- and nanochannels for dilute polymer solutions," *Journal of Chemical Physics*, *128*(14):144903 (APR 14 2008).

[28] Fedosov, D. A., et al. "Velocity limit in DPD simulations of wall-bounded flows," *Journal of Computational Physics*, *227*(4):2540–2559 (FEB 1 2008).

[29] Feng, H., et al. "Micro-phase separation of diblock copolymer in a nanosphere: Dissipative particle dynamics approach," *Fluid Phase Equilibria*, *261*(1-2):50–57 (DEC 1 2007).

[30] Feng, J., et al. "Mesophase separation of diblock copolymer confined in a cylindrical tube studied by dissipative particle dynamics," *Macromolecular Theory and Simulations*, *15*(9):674–685 (NOV 17 2006).

[31] Flory, P. J. *Principles of Polymer Chemistry*. Cornell University Press, 1953.

[32] Gao, L. H., et al. "Improved dissipative particle dynamics simulations of lipid bilayers," *Journal of Chemical Physics*, *126*(1):015101 (JAN 7 2007).

[33] Gibson, J. B. and K. Chen. "The equilibrium of a velocity-Verlet type algorithm for DPD with finite time steps," *International Journal of Modern Physics C*, *10*(1):241–261 (FEB 1999).

[34] Gibson, J. B., et al. "Simulation of particle adsorption onto a polymer-coated surface using the dissipative particle dynamics method," *Journal of colloid and interface science*, *206*(2):464–474 (OCT 15 1998).

[35] Giesekus, H. "A Simple Constitutive Equation for Polymer Fluids Based on the Concept of Deformation-Dependent Tensorial Mobility," *Journal of Non-Newtonian Fluid Mechanics*, *11*(1-2):69–109 (1982).

[36] Groot, R. D. and T. J. Madden. "Dynamic simulation of diblock copolymer microphase separation," *Journal of Chemical Physics*, *108*(20):8713–8724 (MAY 22 1998).

[37] Groot, R. D. and P. B. Warren. "Dissipative particle dynamics: Bridging the gap between atomistic and mesoscopic simulation," *Journal of Chemical Physics*, *107*(11):4423–4435 (SEP 15 1997).

[38] Hafskjold, B., et al. "Can such long time steps really be used in dissipative particle dynamics simulations?," *Molecular Simulation*, *30*(13-15):879–885 (NOV-DEC 2004).

[39] Herrchen, M. and H. C. Ottinger. "A detailed comparison of various FENE dumbbell models," *Journal of Non-Newtonian Fluid Mechanics*, *68*(1):17–42 (JAN 1997).

[40] Hoogerbrugge, P. J. and J. M. V. A. Koelman. "Simulating Microscopic Hydrodynamic Phenomena with Dissipative Particle Dynamics," *Europhysics Letters*, *19*(3):155–160 (JUN 1 1992).

[41] Irfachsyad, D., et al. "Dissipative particle dynamics simulation of grafted polymer brushes under shear," *Physical Chemistry Chemical Physics*, *4*(13):3008–3015 (2002).

[42] Jury, S., et al. "Simulation of amphiphilic mesophases using dissipative particle dynamics," *Physical Chemistry Chemical Physics*, *1*(9):2051–2056 (MAY 1 1999).

[43] Kim, J. M. and R. J. Phillips. "Dissipative particle dynamics simulation of flow around spheres and cylinders at finite Reynolds numbers," *Chemical Engineering Science*, *59*(20):4155–4168 (OCT 2004).

[44] Kong, Y., et al. "Effect of solvent quality on the conformation and relaxation of polymers via dissipative particle dynamics," *Journal of Chemical Physics*, *107*(2):592–602 (JUL 8 1997).

[45] Kranenburg, M., et al. "Phase behavior and induced interdigitation in bilayers studied with dissipative particle dynamics," *Journal of Physical Chemistry B*, *107*(41):11491–11501 (OCT 16 2003).

[46] Kraynik, A. M. and D. A. Reinelt. "Extensional Motions of Spatially Periodic Lattices," *International Journal of Multiphase Flow*, *18*(6):1045–1059 (NOV 1992).

[47] Kumar, S. and R. G. Larson. "Brownian dynamics simulations of flexible polymers with spring-spring repulsions," *Journal of Chemical Physics*, *114*(15):6937–6941 (2001).

[48] Liu, D. H. and C. L. Zhong. "Dissipative particle dynamics simulation of microphase separation and properties of linear-dendritic diblock copolymer melts under steady shear flow," *Macromolecular Rapid Communications*, *26*(24):1960–1964 (DEC 22 2005).

[49] Liu, M., et al. "Dissipative particle dynamics simulation of pore-scale multiphase fluid flow," *Water Resources Research*, *43*(4):W04411 (APR 10 2007).

[50] Liu, M. B., et al. "Dissipative particle dynamics with attractive and repulsive particle-particle interactions," *Physics of Fluids*, *18*(1):017101 (JAN 2006).

[51] Liu, M. B., et al. "Dissipative particle dynamics simulation of multiphase fluid flow in microchannels and microchannel networks," *Physics of Fluids*, *19*(3):033302 (MAR 2007).

[52] Lowe, C. P. "An alternative approach to dissipative particle dynamics," *Europhysics Letters*, *47*(2):145–151 (JUL 1999).

[53] Mackie, A. D., et al. "Dissipative particle dynamics with energy conservation: Modelling of heat flow," *Physical Chemistry Chemical Physics*, *1*(9):2039–2049 (MAY 1 1999).

[54] Malfreyt, P. and D. J. Tildesley. "Dissipative particle dynamics simulations of grafted polymer chains between two walls," *Langmuir*, *16*(10):4732–4740 (MAY 16 2000).

[55] Marsh, C. A., et al. "Static and dynamic properties of dissipative particle dynamics," *Physical Review E*, *56*(2):1676–1691 (1997).

[56] Mckinley, G. H., et al. "The Wake Instability in Viscoelastic Flow Past Confined Circular-Cylinders," *Philosophical Transactions of the Royal Society of London Series A-Mathematical Physical and Engineering Sciences*, *344*(1671):265–304 (AUG 16 1993).

[57] Nikunen, P., et al. "How would you integrate the equations of motion in dissipative particle dynamics simulations?," *Computer Physics Communications*, *153*(3):407–423 (JUL 1 2003).

[58] Novik, K. E. and P. V. COveney. "Using dissipative particle dynamics to model binary immiscible fluids," *International Journal of Modern Physics C*, *8*(4):909–918 (AUG 1997).

[59] Pagonabarraga, I., et al. "Self-consistent dissipative particle dynamics algorithm," *Europhysics Letters*, *42*(4):377–382 (MAY 15 1998).

[60] Pal, S. and C. Seidel. "Dissipative particle dynamics simulations of polymer brushes: Comparison with molecular dynamics simulations," *Macromolecular Theory and Simulations*, *15*(9):668–673 (NOV 17 2006).

[61] Pan, G. and C. W. Manke. "Effects of solvent quality on the dynamics of polymer solutions simulated by dissipative particle dynamics," *Journal of Rheology*, *46*(5):1221–1237 (2002).

[62] Pan, G. and C. W. Manke. "Developments toward simulation of entangled polymer melts by dissipative particle dynamics (DPD)," *International Journal of Modern Physics B*, *17*(1-2):231–235 (2003).

[63] Perkins, T. T., et al. "Single polymer dynamics in an elongational flow," *Science*, *276*(5321):2016–2021 (JUN 27 1997).

[64] Peters, E. A. J. F. "Elimination of time step effects in DPD," *Europhysics Letters*, *66*(3):311–317 (MAY 2004).

[65] Pivkin, I. V. and G. E. Karniadakis. "A new method to impose no-slip boundary conditions in dissipative particle dynamics," *Journal of Computational Physics*, *207*(1):114–128 (JUL 20 2005).

[66] Pivkin, I. V. and G. E. Karniadakis. "Coarse-graining limits in open and wall-bounded dissipative particle dynamics systems," *Journal of Chemical Physics*, *124*(18):184101 (MAY 14 2006).

[67] Pivkin, I. V. and G. E. Karniadakis. "Controlling density fluctuations in wall-bounded dissipative particle dynamics systems," *Physical Review Letters*, *96*(20):206001 (MAY 26 2006).

[68] Ripoll, M. and P. Espanol. "Dissipative particle dynamics with energy conservation: Heat conduction," *International Journal of Modern Physics C*, *9*(8):1329–1338 (DEC 1998).

[69] Rothman, D. H. and S. Zaleski. "Lattice-Gas Models of Phase-Separation - Interfaces, Phase-Transitions, and Multiphase Flow," *Reviews of Modern Physics*, *66*(4):1417–1479 (OCT 1994).

[70] Schlijper, A. G., et al. "Computer-Simulation of Dilute Polymer-Solutions with the Dissipative Particle Dynamics Method," *Journal of Rheology*, *39*(3):567–579 (MAY-JUN 1995).

[71] Schulz, S. G., et al. "The self-assembly of an amphiphilic block copolymer: A dissipative particle dynamics study," *Tenside Surfactants Detergents*, *42*(3):180–183 (MAY-JUN 2005).

[72] Schulz, S. G., et al. "Phase behavior of amphiphilic polymers: A dissipative particles dynamics study," *Colloid and Polymer Science*, *283*(3):284–290 (DEC 2004).

[73] Shardlow, T. "Splitting for dissipative particle dynamics," *Siam Journal on Scientific Computing*, *24*(4):1267–1282 (2003).

[74] Sim, H. G., et al. "Brownian dynamics simulation study on the anisotropic FENE dumbbell model for concentrated polymer solution and the melt," *Bulletin of the Korean Chemical Society*, *21*(9):875–881 (SEP 20 2000).

[75] Spenley, N. A. "Scaling laws for polymers in dissipative particle dynamics," *Europhysics Letters*, *49*(4):534–540 (FEB 2000).

[76] Stoltz, C., et al. "Concentration dependence of shear and extensional rheology of polymer solutions: Brownian dynamics simulations," *Journal of Rheology*, *50*(2):137–167 (MAR-APR 2006).

[77] Symeonidis, V. and G. E. Karniadakis. "A family of time-staggered schemes for integrating hybrid DPD models for polymers: Algorithms and applications," *Journal of Computational Physics*, *218*(1):82–101 (OCT 10 2006).

[78] Symeonidis, V., et al. "Dissipative particle dynamics simulations of polymer chains: Scaling laws and shearing response compared to DNA experiments," *Physical Review Letters*, *95*(7):076001 (AUG 12 2005).

[79] Symeonidis, V., et al. "Schmidt number effects in dissipative particle dynamics simulation of polymers," *Journal of Chemical Physics*, *125*(18):184902 (NOV 14 2006).

[80] Vattulainen, I., et al. "Integration schemes for dissipative particle dynamics simulations: From softly interacting systems towards hybrid models," *Journal of Chemical Physics*, *116*(10):3967–3979 (MAR 8 2002).

[81] Warren, P. B. "Vapor-liquid coexistence in many-body dissipative particle dynamics," *Physical Review E*, *68*(6):066702 (DEC 2003).

[82] Willemsen, S. M., et al. "No-slip boundary condition in dissipative particle dynamics," *International Journal of Modern Physics C*, *11*(5):881–890 (JUL 2000).

[83] Willemsen, S. M., et al. "Mesoscopic simulation of polymers in fluid dynamics problems," *Journal of Statistical Physics*, *107*(1-2):53–65 (2002).

[84] Xia, J. and C. L. Zhong. "Dissipative particle dynamics study of the formation of multicompartment micelles from ABC star triblock copolymers in water," *Macromolecular Rapid Communications*, *27*(14):1110–1114 (JUL 24 2006).

[85] Xu, J. B., et al. "Dissipative particle dynamics simulation on the meso-scale structure of diblock copolymer film," *Acta Physico-Chimica Sinica*, *22*(1):16–21 (JAN 2006).

[86] Yuan, S. L., et al. "Dissipative particle dynamics simulation on the block polymer in aqueous solution," *Acta Physico-Chimica Sinica*, *20*(8):811–815 (AUG 2004).

[87] Zhang, K. and C. W. Manke. "Simulation of diblock copolymer melts by Dissipative Particle Dynamics," *Computer Physics Communications*, *129*(1-3):275–281 (JUL 2000).